DEVELOPMENT OF ADVANCED REMOTE SENSING METHODS FOR WILDLIFE HABITAT MANAGEMENT

Wen Zhang

A Dissertation Submitted to the Faculty of Graduate Studies
in Partial Fulfillment of the Requirements for the Degree of
Doctor of Philosophy

Graduate Program in Earth and Space Science
York University
Toronto, Ontario, Canada
November, 2022

Abstract

Wildlife habitats have been affected by human activities and climate change. Animal diversity is declining at an unprecedented rate. Tools used to obtain a rapid assessment of wildlife habitats at different scales are urgently needed. The habitat management tools that are currently used for conservation and monitoring wildlife are often limited by the availability of mapped habitat information that is tailored to the wildlife of interest and that covers appropriate geographic and temporal extents of interest. Failure to adequately map specific habitat features can limit effective management. Advancements in remote sensing and related technologies have increased the resolution and quantity of landscape data, providing an excellent opportunity to extract various environment features for examining habitat selection and mapping the wildlife habitats to a broad extent.

To exploit the potential of the emergent remote sensing data sets, the focus of this study was to develop advanced methodologies to derive information related to the properties of environmental features at different scales and to generate tools to improve the understanding of a wildlife habitat landscape that can benefit from habitat management. This thesis provided improved derivations for the mapping of wildlife food resource and shelter, including forest structures, forest roads, water, and wetlands that can be important in characterizing habitat for wildlife. A boreal mixed forest located near the town of Hearst, Ontario, Canada was employed as the study site for the characterization of forest structures and mapping the forest roads. Specifically, an advanced algorithm was developed that utilized spatial pattern analysis and machine learning techniques to classify the forest succession stages from easily accessed optical imagery and had a classification accuracy of 89%. In addition, a novel method was proposed to extract road features from the spatial correlation and geometric information of road structure knowledge followed by a deep learning VGG 16 classification for a refined output. An overall accuracy of 74% was achieved for the forest road

extraction. Moreover, another study site located in the western portion of the black duck breeding range, central Ontario, Canada, was employed for surface water mapping and wetland habitat monitoring framework establishment. A robust and operational stepwise automatic thresholding method was developed to accurately map the dynamics of surface water bodies from SAR data, with an overall accuracy of 95%. In addition, an advanced fuzzy AHP model was utilized to accurately map beaver-altered wetlands in the landscape using remote sensing products derived based on the knowledge of beaver activities, where an average of 83.0% of the known beaver dams and 72.5% of the known beaver ponds were correctly identified based on the validation of the independent dataset. In conclusion, this research demonstrated that the advanced methods utilizing multi-source and multi-temporal remote sensing data could effectively characterize and extract environmental features that benefit wildlife habitat management.

Acknowledgment

I have been very fortunate to work with an excellent supervisor Dr. Baoxin Hu in the Department of Earth and Space Science at York University, and Dr. Glen Brown from Ontario Ministry of Natural Resources and Forestry. I would like to express my warmest thanks and gratitude to both professors for recognizing my potential and providing opportunities, encouragement, knowledge and emotional support, and for their energy, enthusiasm and keen insight into current technology with the remote sensing and ecology applications that have enlightened my years during my graduate program.

My heartfelt appreciations are also extended to the members of my committee, Dr. Costas Armenakis, Dr. Jianguo Wang, Dr. Rick Bello, Dr. Jinfei Wang and Dr. Jinjun Shan, for their guidance, support, and constructive challenges they raised. They all made my graduate research study the most enriching professional experience I have had thus far.

I appreciate the financial support I received from various sources, including the Department of Earth and Space Science and research grants provided by the Natural Sciences and Engineering Research Council (NSERC) of Canada. I was privileged to have the support for providing the RadarSat 2 data from Ontario Ministry of Resources and Canadian Space Agency.

I have been fortunate to have outstanding colleagues and friends upon whom to rely for input, help with algorithm design, programming and companionship. I would like to thank Ima Ituen, Rory Pittman, Qian Li, Yongjie Xia, and all the graduate students within the department for their technical or moral support.

Finally, my deepest appreciation goes to my dearest daughter Rachel, whose love

and inspiration keep me moving forward. And to my beloved husband, Peng Zhou, my parents, Yafei Ge and Shizhong Zhang, for their love, support, and understanding that have allowed me to achieve my dreams.

Table of Contents

List of Figures

List of Tables

Chapter 1
Introduction

Human activities can cause loss or degradation of wildlife habitats, negatively impacting biodiversity and causing the threat of species extinction (Gill, Norris, & Sutherland, 2001). The availability of information on wildlife habitats and associated changes over time can be critical to understanding the responses of wildlife to habitat alteration for effective management. The spatial mapping of wildlife habitats can aid in assessing the impact of long-term change (Inkley et al., 2004), habitat fragmentation (Osborne, Alonso, & Bryant, 2001), and other limiting factors. Conventionally, the management and conservation of wildlife and its habitats are based on data collection carried out by human field workers who count animals, observe their behavior, and/or patrol natural reserves. Such efforts are time-consuming, labor-intensive, and expensive (Witmer, 2005). Moreover, the physical and cognitive limitations of humans unavoidably constrain the temporal resolution and complexity of data that can be collected as well as the extent of the physical area that can be effectively monitored. These limitations considerably hamper the understanding of geographic ranges as well

as the ability to assess the greater picture of habitats.

In recent decades, Forest Resource Inventory and land cover products generated from remotely sensed data have been used to assess wildlife–habitat relationships and to support wildlife conservation strategies and actions (Glenn & Ripple, 2004; Johnson, Alexander, Wheate, & Parker, 2003; Maxie et al., 2010; McDermid et al., 2009), typically at coarse spatial scales; however, these maps are generated for multiple purposes and thus may not reflect the habitat features important to specific wildlife and unique life history adaptations. The lack of spatially explicit products of habitat features for applied management, such as the designation of a "critical habitat" as required by the U.S. Endangered Species Act (ESA) and Canada Species at Risk Act (SARA), presents significant challenges when interpreting scale-dependent habitat suitability for endangered species (Rosenfeld & Hatfield, 2006). Failure to adequately map environmental features related to the habitat can limit effective management.

Recent advances in remote sensing technology provide an excellent opportunity to examine habitat selection and to map wildlife habitats to a broad extent, which are often required by management agencies (Rawat & Kumar, 2015; Robertson, McDonald, Delahay, Kelly, & Bearhop, 2015). To realize the full potential of the emergent remotely sensed data sets, the aim was to develop advanced methods

to characterize and extract environmental features that are essential to wildlife habitats. The habitat fulfills the needs of wildlife species for the basic needs of food, water, reproduction (nesting), and protection against predators and competitors (Grebner, Bettinger, Siry, & Boston, 2021). The major components related to the habitat are forest, forest roads, water, and wetlands. Specific importance is described in the following.

(1) Forest can provide food and shelter to the animals (Lindenmayer, 2009). For example, the woodland caribou (*Rangifer tarandus caribou*) tend to select low-productive forests with sparse crown closure where ground lichens are a dominant understory component, and as they consume these lichens as a major component of their diet (Storeheier et al., 2002). In addition, caribou can acquire forage in the lichen-rich landscapes and distance themselves from more productive forests which support higher densities of moose (*Alces alces*) and thus from predators, such as wolves (*Canis lupus*) (Rettie & Messier, 2000).

(2) The presence of roads may result in the fragmentation and loss of habitats (Reed, Johnson-Barnard, & Baker, 1996; Saunders, Bozek, Edwards, Jennings, & Newman, 2002). Human interference has negative consequences for caribou, including direct mortality from vehicle collisions, changes in predator-prey relationships, barrier effects, and avoidance (Dyer et al.2001). These forest roads,

especially the tertiary gravel road, can create linear corridors that allow predators to move through the landscape rapidly and increase predation risk to caribou (James & Stuart-Smith, 2000). Caribou occupancy is often reduced within 1-10 km from such disturbances (Vors et al., 2007, Schaefer & Mahoney, 2007)

(3) Another essential requirement of wildlife habitat involves the availability of water, and water birds depend on wetlands for breeding and feeding (DeGraaf, Yamasaki, Leak, & Lester, 2006). Global climate change is expected to decrease water quality and wetland availability for ducks through drought conditions (Guillemain et al. 2013). Also, spatial variation in the lakes across the breeding range could potentially influence the variation in black duck distribution and demographic rates.

(4) Wetlands are critical for wildlife, especially for waterfowl. Evidence suggests black ducks, like other waterfowl, show a preference for more productive, nutrient-rich water bodies, likely related to their high energy demands during egg production and brood rearing (Diefenbach & Owen 1989; Merendino & Ankney 1994; Rempel et al. 1997). The wetland habitat features may affect the distribution and reproductive performance of breeding waterfowl.

In summary, these components, forest stages, forest roads, water bodies, and wetlands are keys for habitat mapping, but their derivations require further

improvement (with the details in the following paragraphs). Hence, they were the focus of this research. The findings can help identify the value of remote sensing products to support standardized monitoring of changes in wildlife habitats and the integration into the existing monitoring-management framework. To achieve the research goal, the following four specific objectives were identified and fulfilled.

(1) Advancement of the classification of the forest succession stage using very high resolution multispectral aerial imagery.

The structural attributes of the succession of naturally disturbed forests and the associated resources, such as food availability, can influence on the presence of wildlife species (Swanson et al., 2011). Light Detection and Ranging (LiDAR) derived height metrics are capable of characterizing the three-dimensional structure of forest canopies and studies have been using them to map forest succession stages with promising accuracy (Falkowski, Evans, Martinuzzi, Gessler, & Hudak, 2009; Van Ewijk, Tritz, & Scott, 2011). However, for habitat mapping, the large-scale coverage of repeated high density LiDAR data is still costly. To alleviate the spatial and temporal limitations of airborne LiDAR data, rapidly available high spatial resolution optical imagery is exploited. To realize

the full value of high spatial resolution imagery, an advanced algorithm is needed to derive the spatial patterns exhibited in the imagery to classify complex forest succession stages.

(2) Development of a deep-learning-aided method for the automatic identification and mapping of forest roads.

For large-scale habitat assessment, the road network is another key factor that significantly impacts wildlife habitats. Human activities along roads may increase the risk of mortality through changes in predator movement and collisions with vehicles (Cain, Tuovila, Hewitt, & Tewes, 2003; Fuller, 1989; Lin, 2016). Mapping forest roads, such as maintained and logging roads, is usually carried out through the manual interpretation of high spatial resolution optical imagery, which is time-consuming and labor-intensive. Several studies have been carried out to automatically extract roads from remotely sensed data (mainly passive optical imagery) based on the fact that roads are linear features with edges and have different spectral signatures than surrounding objects (Ravanbakhsh, Heipke, & Pakzad, 2008; Tang, Li, Huang, & Yang, 2014; Valero, Chanussot, Benediktsson, Talbot, & Waske, 2010). Although promising results have been obtained, most are focused on extracting road centrelines from an urban area. The

detection of forest roads remains underdeveloped, as this type of road is narrow with the apparent interspersion of forest cover. The recent advances in the data-driven convolutional neural network (CNN) have created new opportunities, and studies have been carried out to apply them to road detection in a complex forest scene(Saito, Yamashita, & Aoki, 2016; Wei, Wang, & Xu, 2017). Nonetheless, it is resource-consuming to scan an entire forest scene using CNN to extract sparse forest road data because image classification using a deep-learning network requires intensive computational power. Therefore, an integration of traditional machine learning and the CNN network is needed for efficient forest road mapping.

(3) Development of a robust automatic and operational process to map the dynamics of surface water bodies.

Wetlands provide a habitat for a range of wildlife, including water birds, and mapping surface water can be a key component of tracking changes in wetland states. Synthetic Aperture Radar (SAR) is especially effective due to its ability to detect water and flooded vegetation. In SAR imagery, water has specular microwave reflection, which appears dark and homogeneous. Such information is useful in detecting flooded areas and in classifying wetlands (Hess, Melack,

Novo, Barbosa, & Gastil, 2003; Lane & D'Amico, 2010; Touzi, Deschamps, & Rother, 2007). Several studies have been conducted to map surface water with SAR data using thresholding techniques with the low return signal behavior of open water. Specifically, the methods include manually-defined histogram thresholding (Santoro et al., 2015; Westerhoff et al., 2013), Otsu's algorithm (Li & Wang, 2015), a radiometric threshold based on a gamma distribution (Liang & Liu, 2020; Matgen et al., 2011), and a set of thresholds based on a statistical analysis of the training data(Sandra Bolanos, Stiff, Brisco, & Pietroniro, 2016; S. Hong, Jang, Kim, & Sohn, 2015). These approaches are not fully automatic, and some of them require additional processes to generate high-accuracy surface water maps, such as supervised classification approaches(Brian Brisco, 2015; S. Hong et al., 2015; Huang et al., 2018; Morandeira, Grings, Facchinetti, & Kandus, 2016), region growing segmentation(Sandra Bolanos et al., 2016; Manjusree, Prasanna Kumar, Bhatt, Rao, & Bhanumurthy, 2012a; Martinis, Twele, & Voigt, 2009; Matgen et al., 2011), and machine-learning approaches (P. Zhang et al., 2019; X. Zhou, Liu, & Zhang, 2019). Even with their success, these methods are time- and labor-intensive and thus are not operational (Santoro et al., 2015; H. K. Zhang & Roy, 2017). A fully automatic and incident angle independent algorithm is therefore needed to support the timely production of surface water mapping.

(4) Development of a framework to utilize multi-source and multi-temporal remote sensing data for wetland structural habitat features using an advanced fuzzy Analytical Hierarchy Process (AHP) model.

As the availability of remote sensing-derived environmental metrics increases, new opportunities open to investigate how these metrics are relevant in explaining patterns in the distribution and abundance of wildlife and habitats. These metrics should be exploited to their full potential by translating the relationship into predicted habitat maps that can be used in habitat management and conservation plans. Despite much progress in targeting habitat management in staging and wintering areas, methods to identify and target high-quality breeding habitats that result in the greatest potential for wildlife are still required. This is particularly true for species that breed in remote, inaccessible areas, such as the American black duck, an intensively managed game bird in Eastern North America. Although evidence suggests that black ducks prefer productive, nutrient-rich waterbodies, such as beaver ponds, information about the distribution and quality of these habitats across the vast boreal forest is lacking an accurate identification, creating a challenge. Continuing advancements in remote sensing technologies that provide spatially extensive and temporally

repeated information are particularly useful in closing this information gap. Multi-source and multi-temporal remote sensing data should be used to derive environmental metrics that are tailored to the needs of wildlife along with a mathematical model to map a habitat's spatial distribution.

The research related to the abovementioned four individual objectives are described in the following chapters respectively: Chapter 2, characterizing forest succession stages for wildlife habitat assessment using multispectral airborne imagery and machine learning technique; Chapter 3, forest roads extraction through a convolution neural network aided method; Chapter 4, automatic surface water mapping using SAR data and robust thresholding for long-term change detection; and Chapter 5, beaver pond identification from multi-temporal and multi-sourced remote sensing data through an AHP model.

This dissertation research generated the following publications:

1. Zhang, W., Hu, B., Brown, G., and Meyer, S. (2022). Beaver Pond Identification from Multi-temporal and Multi- Sourced Remote Sensing Data. *Journal of Geo-spatial Information Science*, under revision.
2. Zhang, W., & Hu, B. (2021). Forest roads extraction through a

convolution neural network aided method. *International Journal of Remote Sensing*, 42(7), 2706-2721.

3. Zhang, W., Hu, B., & Brown, G. S. (2020). Automatic surface water mapping using Polarimetric SAR data for long-term change detection. *Water*, 12(3), 872.
4. Zhang, W., Hu, B., & Brown, G. (2018). Wetland Classification for Black Duck Habitat Management Using Combined Polarimetric RADARSAT 2 and SPOT Imagery. *The International Archives of the Photogrammetry, Remote Sensing and Spatial Information Sciences*.42(3).
5. Zhang, W., Hu, B., Woods, M., & Brown, G. (2017). Characterizing Forest Succession Stages for Wildlife Habitat Assessment using Multispectral Airborne Imagery. *Forests*, 8(7), 234.
6. Zhang, W., Hu, B., & Quist, L. (2017). Forest Road Identification and Extraction through Advanced LOG Matching Techniques. *International Archives of the Photogrammetry, Remote Sensing & Spatial Information Sciences*, 42.

Chapter 2

Characterizing forest succession stages for wildlife habitat assessment using multispectral airborne imagery and machine learning techniques

In this chapter, the work on the characterization of forest 3-D structures and succession stages is presented. Four forest succession stages were adopted: stand initiation, young multi-story, understory reinitiation, and old growth. Remote sensing metrics describing the spatial patterns of forest structures were derived and a random forest learning algorithm was used to classify forest succession stages (classification accuracy of 89%). These metrics included texture variables from Gray Level Co-occurrence Measures (GLCM), range and sill from the semi-variogram, and the fraction of shadow and its spatial distribution. In addition, the imagery spatial variables were shown to be consistent with the LiDAR derived variable (R2=0.68 and RSME =2.39). It was demonstrated that high spatial

resolution imagery was able to characterize forest succession stages with promising accuracy and may be considered as an alternative to LiDAR data.

The research in this chapter is published in the following journal paper:

Zhang, W., Hu, B., Woods, M., & Brown, G. (2017). Characterizing Forest Succession Stages for Wildlife Habitat Assessment using Multispectral Airborne Imagery. Forests, 8(7), 234.

I thank the Forest, MDPI publisher, and other authors who have permitted me to reuse the article in my dissertation.

2.1 Related work

Conventionally, the characterization of the forest successional stages was conducted by field work and generally is used at the local scale. Applications of moderate resolution products to delineate wildlife habitat have revealed both benefits (e.g. broad-scale mapping) and limitations for inferring ecological relationships and differentiating fine-scale environmental features relevant to wildlife. As wildlife respond to understory features that are not readily mapped using moderate resolution products, ground sampling or fine-scale aerial imagery may augment interpretation (Hill, 1987; Szantoi, Smith, Strona, Koh, & Wich, 2017). Accurate classifications of forest successional stages at large spatial extents are essential for characterizing wildlife habitats , where wildlife adapted to various forest stand conditions (Helle & Monkkonen, 1990).

The development of light detection and ranging (LiDAR) instruments has provided a good opportunity to explore the vertical structures of forest canopies for wildlife habitat mapping (Bergen et al., 2009). As an optical-remote-sensing technology, a LiDAR instrument measures the properties of scattered light to find the range of a target. Based on the measured distance and associated recorded

time, the three-dimensional (3-D) geo-coordinates of the surface object are obtained. For the past decades, airborne LiDAR data have been widely exploited in forest applications, in particular for retrieving forest structural parameters, such as tree height, crown diameter, stem density, basal area, and biomass (Lim, Treitz, Wulder, St-Onge, & Flood, 2003). Recent studies have also shown that a set of LiDAR derived height metrics characterizing the three-dimensional structure of forest canopies can map forest succession stages with promising accuracy (over 85%) (Falkowski et al., 2009). Not only the point clouds, but LiDAR derived image-based Canopy Height Model (CHM) has also been utilized for textural analyses to describe the tree density(Ozdemir & Donoghue, 2013). However, large scale coverage of high density LiDAR data is still costly. In this study, I exploited the use of high spatial resolution passive imagery as a useful alternative for LiDAR data in the characterization of forest succession stages.

So far, studies have been conducted to use high spatial resolution imagery in characterizing forest structures with variables like crown closure, density, basal area, and stand age (Wulder, Hall, Coops, & Franklin, 2004). One of the widely-used methods is calculating the semi-variogram. Semi-variogram illustrates the variations in the brightness value of pixels separated by a series of lag distances.

The range of the semi-variogram is an indicator of the distance of spatial dependence and is often related to the size or scale of dominant objects in the imagery (Curran, 1988). The sill is an indicator of the total structurally dependent variance in the data (Johansen, Coops, Gergel, & Stange, 2007). Lévesque and King (Levesque & King, 1999) related semi-variograms to such forest structures as canopy and crown closure, stem density, tree height, and crown size. Also, Song and Woodcock (C. Song & Woodcock, 2002) demonstrated that range and sill of semi-variogram were related to the size of the dominant tree crown and found they were not sensitive to changes in canopy sizes when image resolution was greater than the tree crowns size. Another commonly used method to characterize spatial variation in forest canopies is based on the Gray Level Co-occurrence Matrix (GLCM). Different from first-order texture measures, such as the standard deviation of gray level values, GLCM provides second-order statistics that describe the relationship among the brightness values of neighboring pixels in an image. Kayitakire et al. (Kayitakire, Hamel, & Defourny, 2006) estimated the forest variables including crown height, crown circumference, tree stand density, and ages from GLCM-derived textural variables with IKONOS-2 imagery. Ozdemir and Karnieli (Ozdemir & Karnieli, 2011) correlated old forest structural parameters including the number of trees,

basal area, stem volume, diameter differentiation index, contagion Index, Gini coefficient, and standard deviation of diameters at breast heights with GLCM texture features extracted from 2 m resolution WorldView-2 image. In addition, different from the low-resolution satellite imagery, shadows can be observed in high-resolution aerial imagery. Few studies have reported the relationship between the delineated area of tree shadows to structural parameters, such as diameter-at-breast height (DBH) and crown area(Greenberg, Dobrowski, & Ustin, 2005; Ozdemir, 2008) .

The studies mentioned above have associated image spatial variables to single forest structural attributes such as tree height, crown size, and tree densities. I extend previous work by using an integrative approach to combine the metrics to derive the horizontal spatial patterns exhibited in high spatial resolution imagery to characterize the forest succession stages. The objective of this research is to advance the classification of forest succession stage using very high resolution multispectral aerial imagery, applications of imagery spatial pattern analysis and machine learning techniques, and to exploit the potential of a cost-effective LiDAR alternative. Remote sensing metrics including imagery texture analysis of semi-variogram, GLCM, and spectral measures of shadows fraction and

shadows distribution were derived for forest succession stages classification, and most significant variables were recommended for faster processing.

2.2 Materials and Methods

The study area is located in the Hearst Forest near the town of Hearst, Central Ontario, Canada (49.7°N, 83.7°W) (Fig. 2.1). Hearst Forest falls within the boreal mixed wood region and covers approximately 1.23 million ha, 1.00 million ha of which is productive forest. The main species within the forest are black spruce (*Picea mariana*), white spruce (*Picea glauca*), balsam fir (*Abies balsamea*), trembling aspen (*Populous tremuloides*) and black poplar (*Populous balsamifera*).

The optical imagery acquired using a Leica ADS-40 during July and August 2007 has four spectral bands (blue, green, red and near-infrared) with a spatial resolution of 0.4 m by 0.4 m. The solar angle at the time of the data collection was 36.8 degrees. LiDAR data were also collected in between July 4 and September 4, 2007 during leaf-on conditions using an Optech ALS50 sensor mounted in a Cessna 310 aircraft with an average flying altitude of 2400 meters above mean sea level. Average sampling density was 1.1 returns per square meter. The LiDAR data were used in this study to access the structural properties of

forest canopies from different succession stages, and compare with those derived from optical imagery. Figure 2.1 shows the location of the study site and gives an overview of the multispectral imagery.

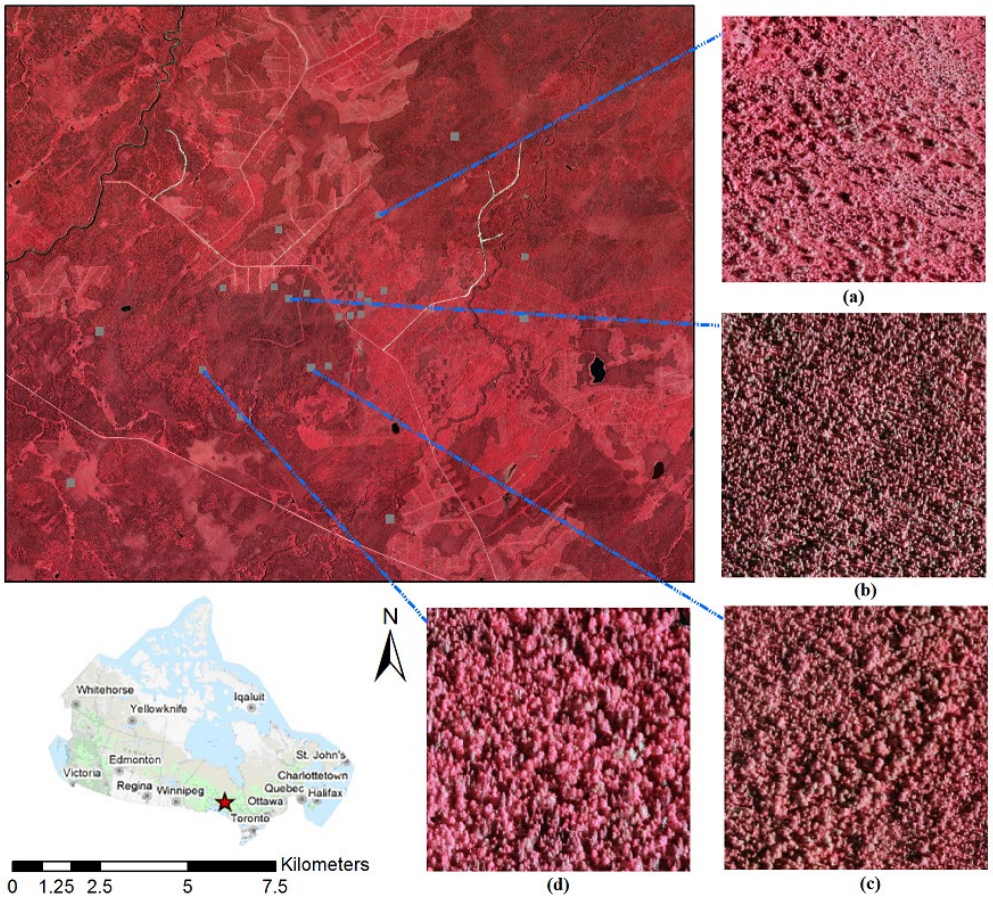

Figure 2.1. False-color imagery of the study site, with the near infrared band printed as red, red as green and green as blue. Test sites are marked with gray squares. The location of study area in Hearst Forest, Ontario, Canada is at lower left panel. And the imagery of forest stands at the four development stages: (a) stand reinitiation, (b) young multistory, (c) understory reinitiation, and (d) old-growth stage. The false color composite of the optical imagery covering the study area is displayed with the near-infrared band as red, red as green and green as blue.

Four general forest succession stages were adopted in this study [23]: stand initiation, young multi-story, understory reinitiation, and old growth. The stand initiation stage indicates the stage where new vegetation becomes established and fully occupies a disturbed site. The following young multi-story stage is mainly characterized by competition among the dominant trees. After some time when younger trees start to regenerate, the stand enters the understory reinitiation stage. In the last stage, the old growth stage, autogenic and gap-replacing processes create patches large enough for the stand re-initiation to begin.

From the entire study area, 24 test areas representing four different succession stages were selected based on visual interpretation and the aid of tree height information from LiDAR. Each test site 501 x 501 pixels (200m x200m) was subset. Examples of the test sites representing the four forest succession stages are shown in Figure 2.1(a) to (d).

For each test site, to capture the spatial variation of forest canopies within a stand, calculations were conducted with a block size of 50 pixels by 50 pixels (i.e. 400 square meters). Such a block size was chosen as an adequate size to capture the variation within forest stands in each of the successional stages of this forest. To examine the ability of high spatial resolution imagery to differentiate forest stages,

semi-variogram, GLCM, and the fraction of shadow and its spatial distribution were calculated through a self-written C++ program.

Semi-variogram measured the squared difference in brightness between pairs of pixels with a given distance apart and thus indicated the spatial variability of the observed tree canopies. The sill is the upper limit of the variance, which is equivalent to the overall variance in the image. The range is the distance at which the variance reaches the sill. The nugget effect is the variance at lag zero. From the semi-variogram, the variance values among pixels can be observed to increase with the lag distance between these pixels and become flattened out when the distance is large. The range was interpreted as the maximum crown size (B. Hu, Li, Jing, & Judah, 2014). The height of the sill of the variogram was related to the density of trees (Woodcock, Strahler, & Jupp, 1988). To quantitatively relate the range and sill of a semi-variogram to the spatial variation of its corresponding stand, the experimental semi-variogram were calculated and then modeled using exponential model fitting, and range, sill, and nugget were determined

To characterize forest canopies, the GLCM was used to calculate second order mean, standard deviation, contrast, Angular Second Moment (ASM), entropy, homogeneity, dissimilarity and correlation (Cosmopoulos & King, 2004;

Haralick, Shanmugam, & Dinstein, 1973; Pesaresi, 2000). The first principal component from a PCA (principal component analysis) was used for the calculation of GLCM. For each pixel, four GLCMs were calculated within a neighborhood of 50 pixels by 50 pixels at four directions, 0°, 45°, 90° and 135°. The displacement parameter in GLCM calculation defines the scale at which the texture was analyzed. For our purpose, details of the spatial pattern were desired, and displacement distance was set equal to one pixel. The reason for selecting this value was to capture the variation within stands. When displacement value increases, the GLCM values become diverse and make it more difficult to distinguish between different stages.

In addition, shadows observed in imagery as a proxy for spatial attributes of forest canopies were investigated. In general, the distribution of shadows varies with tree height and size of the overstory. As shown in Figure 2.2, the presence of shadows was different from stage to stage. Therefore, the shadow fraction that represents the shaded background was used as one descriptor to measure the structure difference of the forest stand development. In this study, shadow fraction was calculated as the ratio of shaded area to total area of the window size 50 x 50 pixels (20m x 20m). It was derived by using the near infrared band because the contrast between the tree stands and the shaded background was the

greatest. First, the distribution of the histogram was analyzed, and a threshold value was determined to separate the pixels into shaded and non-shaded groups. Then, the ratio between the number of shaded pixels and the total number of pixels within the window were calculated as the shadow fraction.

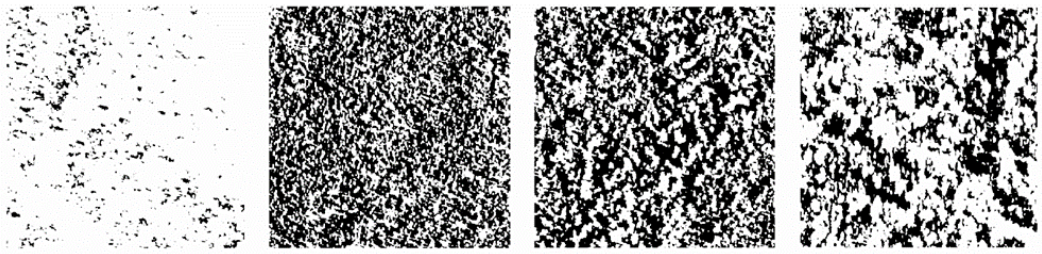

Figure 2.2. Shadow map for forest stands at (a) stand initiation stage, (b) young multistory stage, (c) understory re-initiation stage, and (d) old growth stage, where black color indicates shaded background and white indicate sunlit background.

To further describe the forest succession stages in the measure of shadow distribution, a quadrant count (QC) method (Dale et al., 2002) was used. For a given site, the shadow maps from the previous step were used to calculate the degree of clumping to characterize the clumps of trees. Those maps were partitioned into *m* square regions called quadrats. The side length l of these quadrants was set to be 50 pixels to represent stands level for all sites. In each quadrat, the number of pixels that were marked as shadow was counted and the

spatial pattern of the shadow for that site was described by a variance-to-mean ratio (VTMR) defined as:

$$VTMR = \frac{Variance}{Mean} = \frac{(\sum x_i^2 - (\sum x_i)^2/m)/(m-1)}{\sum x_i/m}, \qquad \text{(Eq. 2.1)}$$

Where x_i is the number of pixels in each quadrat, and m is the number of quadrats in the layer. VTMR values is a dispersion index, where the value equals to zero represent a constant random (not dispersed) case, and larger values represent greater clustering.

The variables derived from semi-variogram, GLCM, shadow fraction and degree of tree clumping were used in a Random Forest classification to investigate forest succession stage differentiation. The random forest classifier consists of an ensemble of tree classifiers generated randomly from the input vector and outputs the classes that are voted by individual trees (Breiman, 2001). It has been demonstrated in recent applications that a random forest is an excellent classifier for hyperspectral remote sensing data, and multisource geographic data(Gislason, Benediktsson, & Sveinsson, 2006; Ham, Chen, Crawford, & Ghosh, 2005; Lawrence, Wood, & Sheley, 2006). In this study, the Random Forest was chosen due to the following two advantages, compared with other classification methods. First, random forest classification was a non-parametric algorithm easy to

interpret and free from dependence on the distribution assumption to achieve an accurate result. Second, each of predictor variables was interpreted by calculating the influence of the model accuracy, which was used to determine the importance of each variable, and to select the optimal ones to further reduce the data redundancy (Cutler et al., 2007). In this study, 50 trees were used in the classifier as the analysis showed no significant difference between the forests after reaching the number. Analysis was conducted using the Random Forest package in the R statistical program (R Core Team. Available online: http://www.R-project.org).

Classification accuracy was assessed using a confusion matrix, where each column represented the predicted stage, and each row represented the actual stage. The class accuracy of each succession stage was calculated as the number of correctly predicted samples divided by the total number of samples in that stage, and the overall accuracy was calculated as the total number of correctly classified stages divided by the total number all tested samples. Also, to further validate the classification result, LiDAR derived forest stage indicator was generated. The empirical model was built to link the LiDAR statistical derived metrics and the forest succession stage. Due to the lack of field surveys, no sufficient information was available to establish a direct relationship between the LiDAR point clouds

and forest attributes at different stages. Thus, the model (Equation (2.2)) reported in van Ewijk et al (Van Ewijk et al., 2011) to predict Lorey's height (PLH) for forest succession stage was adopted. Lorey's height (the stand tree height weighted by basal area) was found to be a good index in their study to separate the young multistory stage from an understory reinitiation stage. The reported model had an $R^2 = 0.86$, compared to the predicted quadratic mean diameter at breast height model which only achieved an $R^2 = 0.68$.

$$PLH = 17.72 + 6.47\ H\_Skew + 0.94\ H\_Kurtosis + 0.80\ H\_P9 - 16.59\ H\_D6, \quad \text{(Eq. 2.2)}$$

Where *H_Skew* is the Skewness of Heights, *H_Kurtosis*is the Kurtosis of Heights, *H_ P9* is the 90th Height Percentile, and *H_D6* is the 6th Height Decile.

All returns of discrete LiDAR points were utilized for mapping the forest stage. First, the LiDAR data were classified by the vendor using the standard American Society for Photogrammetry and Remote Sensing classification and Terra Solid's TerraScan software. Classified ground returns were used to generate a 1-m bare earth DTM raster, against which LiDAR vegetation returns were normalized. For

stand level analysis, the entire area of 4 km by 4 km was arbitrarily cut into height bins in size of 20m by 20m, and PLH within each height bins was calculated. Linear regression was modeled to determine if used variables and PLH were correlated with each other.

2.3. Results and Discussion

2.3.1. Semi-variogram

The semi-variograms for the four stages revealed that the range of the variance for forest stands at the initiation stage was the smallest, and the range of the old-growth forest stands was the greatest (Figure 2.3). These values were close to the sizes of the dominant trees in the sites. The sill of the variance was related to the variation in the brightness value of the pixels, which in turn were related to percent canopy cover and vertical layering in the stands (Cohen, Spies, & Bradshaw, 1990). As expected, stand initiation and young multistory stands have single canopy layers, and the corresponding sill values are low. The understory reinitiation and old-growth have multiple canopy layers with higher contrast and resulting in a higher sill values. Also, multiple peaks exhibit variance of forest stands at stand initiation and old growth stages. The results indicate gaps or clumps of trees in the stands at stand initiation stage, and mixed clumping

pattern of trees in the stands at old-growth stage.

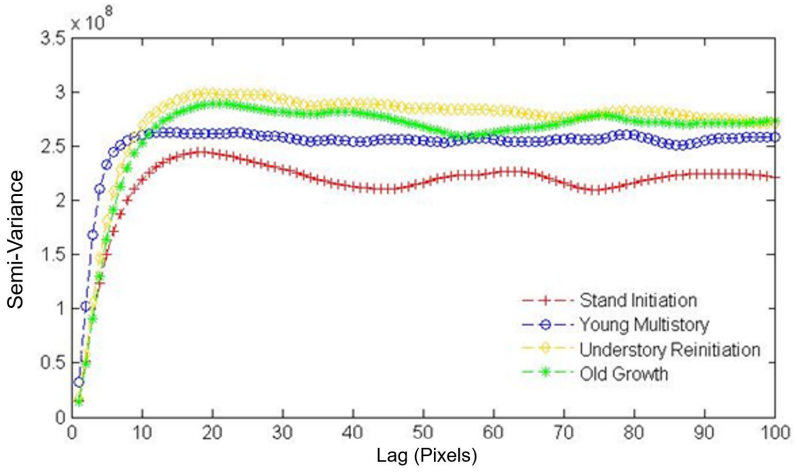

Figure 2.3: Semi-variogram of the four forest succession stages: forest stands at stand re-initiation, forest stands at young multi-storey, forest stands at understory reinitiation, and forest stands at the old-growth stage.

Table 2.1. Average and standard deviation of semivariogram parameters

Forest Stages	**Range (pixels)**		**Sill**	
	Mean	St. Deviation	Mean	St. Deviation
Stand Initiation	3.56	3.84	22.83	11.21
Young Multi-storey	3.20	1.27	189.51	15.48
Understory re-initiation	3.71	1.23	153.38	19.79
Old Growth	5.88	2.57	187.25	60.26

The range value decreases from stands at the first stage (stand initiation) to the second (young multistory) and then increases to the third and fourth stage (understory re-initiation and old growth, respectively) Table 2.1). At the early

stage, when most of the area was bare soil, its spatial variation is rough and can be recognized as objects with an irregular shape in various sizes. From the young multi-story stage to the old growth stage, the tree crowns are dominant. Therefore, the range value increases as the size of the crown increase from young to old stages. This is validated by comparing the standard deviation of range value. In second and third stages, the tree crown surface is more homogeneous, resulting in a smaller standard deviation. In contrast, both stand initiation and old growth stages had higher standard deviation, which may relate to greater canopy openness and associated variability.

To further demonstrate the relationship of range and sill for different stages, a scatter plot was created, with each stage assigned a different color. As shown in Figure 2.4, the stands at the stand initiation stage have a significant smaller sill value, which can be used to distinguish it. Also, though there is some overlapping, the majority of young multistory and multistory reinitiation were separate from each other, while the old growth was mixed with them.

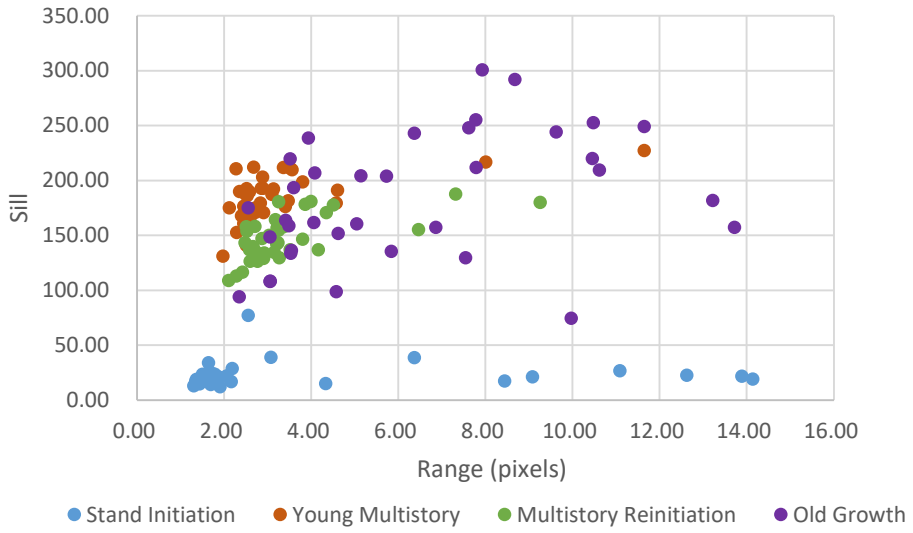

Figure 2.4. Scatter plot of semivariogram parameters range and sill for four forest stages with the Range in the unit of pixels.

2.3.2. GLCM

Findings from the GLCM texture variable analysis indicated that no single variable can be used to separate all four succession stages; however, contrast showed the largest differences (Figure 2.5). Higher contrast values represent greater spatial variation between neighboring pixels. At the young multi-story stage, the tree crowns were relatively small, and the neighboring pixels of different features (such as crown and soil) occur more frequently, leading to greater contrast. On the other hand, old growth stands have bigger crowns, and

the neighboring pixels were more likely to be within same features (crown or understory), and thus the contrast appeared to be the smallest.

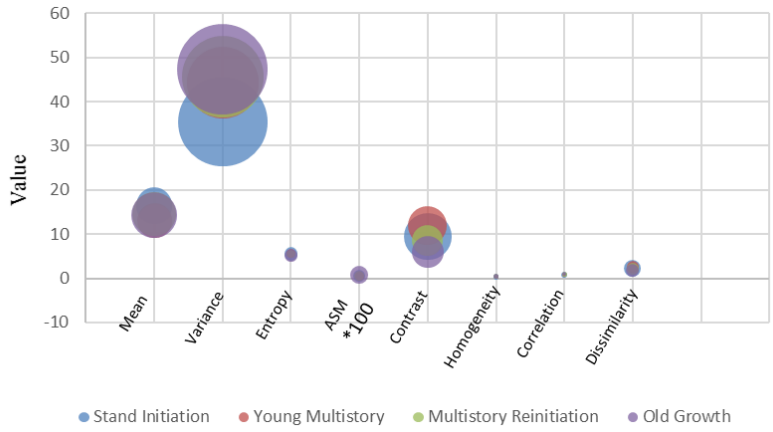

Figure 2.5. Bubble plot of variables for forest stands at four stages, where the location of the bubbles indicates the mean value of that stage and the size of the bubble represents the standard deviations.

2.3.3. Shadow characteristics

Shadow fractions varied among the forest stages but the differences were not significant between adjacent stages (Table 2.2).

Table 2.2. Shadow fraction derived from NIR band from four forest succession stage

Forest Stages	**Shadow Fraction**	
	Mean	St. Dev.
Stand Initiation	0.0023	0.0041
Young Multistory	0.0914	0.0384
Understory Reinitiation	0.0515	0.0299
Old Growth	0.0188	0.0153

VTMR differed significantly among young multistory, stand re-initiation and old growth, as the mean values of the VMTR are 44.63, 95.93, and 175.84 and stand deviation of 15.16, 37.59, and 64.96, respectively (Figure 2.6). The result has demonstrated that shadow distribution could be used as an indicator for classifying between these three stages. Old growth had the highest VTMR and thus most clustered overstory, and young multistory had the lowest VTMR and most homogenous tree distribution. At the stage of stands at young multistory, most trees in early growth had crowns that were isolated, resulting in dispersed shadow areas. In the stage of stands at old growth, big crowns from the mature stands and the multistory created clustered shadows. Bare soils were dominated

in stands at stand initiation and caused shadow to be randomly distributed.

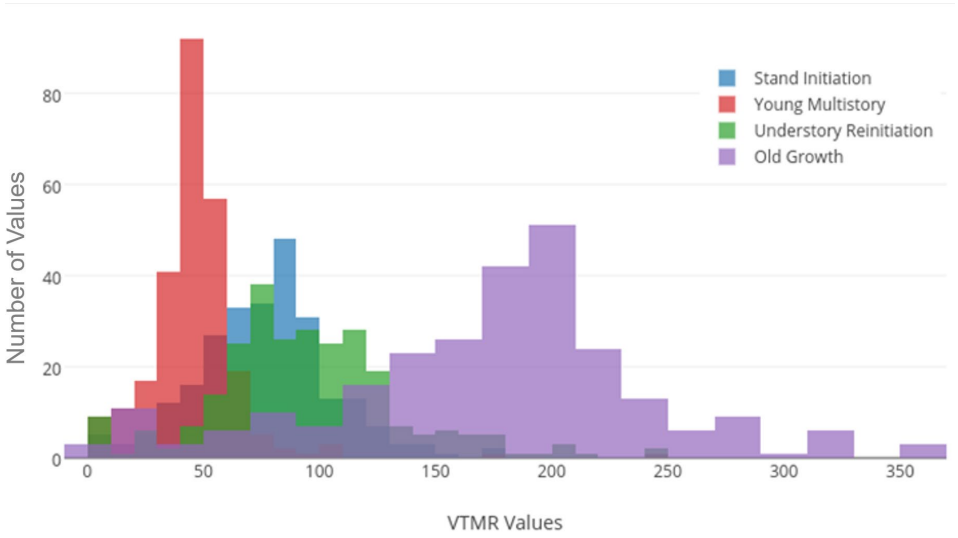

Figure 2.6. VTMR of each quadrat from all four forest succession stages.

2.3.4. Classification of forest succession

In total, 32 variables as eight texture features per each direction, together with shadow fraction were used to perform random forest classification. 1424 out of 1600 samples were correctly classified to achieve an accuracy of 89 % (Table 2.3).

Table 2.3. Confusion matrix from random forest classification

Class		Predicted				User Accuracy
		Stand Initiation	Young Multistory	Understory Reinitiation	Old Growth	
Actual	Stand Initiation	345	20	25	10	86.25%
	Young Multistory	17	362	21	0	90.50%
	Understory Reinitiation	10	20	248	22	82.67%
	Old Growth	5	0	28	467	93.40%
Producer Accuracy		91.51%	90.05%	77.02%	93.59%	
Overall Accuracy						89%

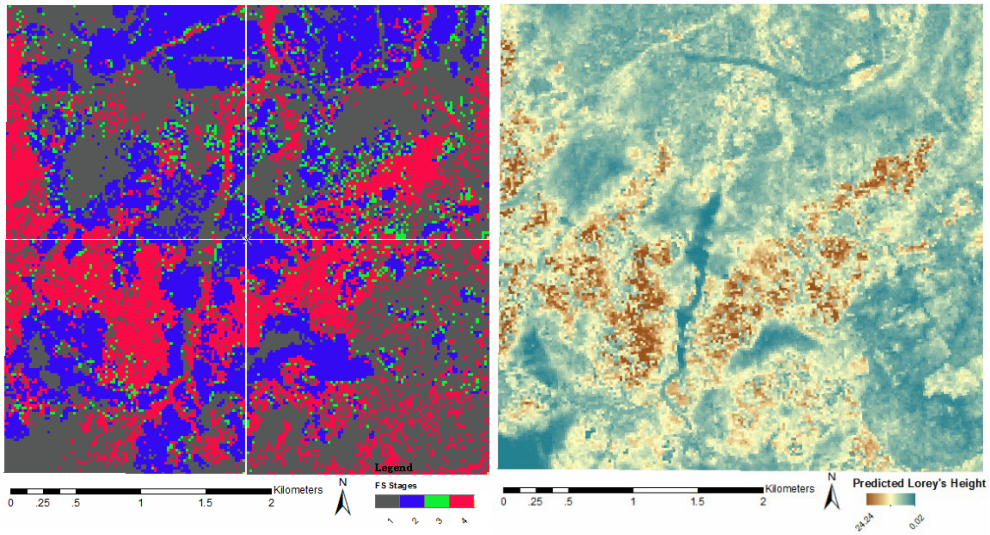

(a) (b)

Figure 2.7: (a) Color shaded forest succession stages predicted from multispectral image spatial patterns with brown, blue, green and red represent the forest stands at (1) stand re-initiation, (2) young multistory, (3) understory reinitiation, and (4) old growth stage respectively. (b)The color shades PLH map derived from LiDAR data with color from blue to red indicate PLH from low to high.

The forest succession stages derived from the image spatial pattern analysis agreed with the PLH from LiDAR data (Figure 2.7). All the areas with high PLH (brown-shaded area in Figure 2.7(b)) were classified as stands at old growth stage (red color areas in Figure 2.7(a)). Most of the forest stands identified from images as re-initiation stage areas identified from images (shaded green in Figure 2.7(b)) corresponded well to low PLH. The same can be noted for the stands at the young multi-story stage too. Only the stands identified from the images as stands at understory reinitiation stage appeared to be under classified, potentially related to its transitional nature between multi-story and old growth. Also, the image texture of the stands at this stage was very similar to the stands at old-growth stage. As evident from the confusion matrix of random forest classification (Table 2.3), most of the commission error of stands at understory reinitiation stage was due to these stands being classified as old-growth.

From a visual comparison, forest succession stages generated from image texture provides a similar classification map as one created from PLH generated from LiDAR point cloud. A linear regression fit to the suite of variables and the LiDAR derived PLH resulted in an $R^2 = 0.68$ and RSME = 2.39. It has to be noted that the R^2 was 0.86 of the PLH and field data for the Petawawa research forest. Differences of forest type exist between our study area and Petawawa research

forest, and also between the real field data and regression model. Overall, the texture features used for classification were correlated with the LiDAR derived PLH.

2.3.5. GLCM parameter sensitivity analysis

The effects of window size and displacement on GLCM derived texture variables were assessed using classification accuracies. The size of the processing window was a trade-off between finding enough spatial information to characterize the land features and limiting overlapping textures of different land features. A large window size captured a better representation of spatial patterns of each stage, but also contained patterns from other stages and introduced systematic errors. For our purpose, the average size of the sampling unit that described the within stand variation was used to accommodate a window size of 50 pixels by 50 pixels. To test if this value was the optimal value, GLCM texture variables were calculated with different window sizes and tested in the Random Forest classification process. As shown in Figure 2.8 (a), the classification accuracy increased as the processing window size increased. When window size was greater than 40 pixels, the improvement of the classification accuracy started to diminish.

It worth mention that a standard window size in this study provides promising

results, further analysis should include segmentation process to extract canopy objects. The texture measurements should be processed within each object rather than predefined windows. The canopy openness, size of the crown/stands was all different at different stand development stages of the forest. At the early stage of the forest dynamics, the trees are generally more isolated, while in their mature stage, when they grow into each other, the overlaps of the tree crown made multiple crowns clustered as one single object. Thus, one window size cannot fit all forest stages.

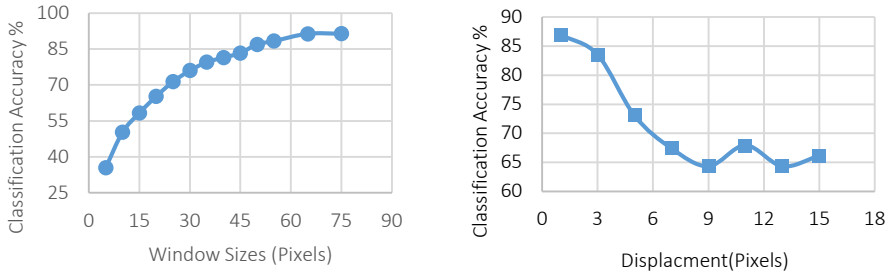

(a) (b)

Figure2.8. Overall random forest classification accuracy results of changing GLCM parameters. (a) Classification accuracy versus window sizes. (b) Classification accuracy versus displacements.

Also, to test if the displace equal to one pixel was the optimal value, texture variables were calculated with different displacement distances and in the random forest classification process. As shown in Figure 2.8 (b), the classification accuracy decreased with the increase of the displacement distance.

When displacement equaled 11 pixels, a slightly increase in the classification accuracy was observed, indicated a spatial relationship between two pixels that were 10 pixels apart, in our case meaning the dominant tree/tree clump size.

2.3.6. Feature selection for classification variables selection

Although promising classification accuracy was achieved, the number of variables used in the classification was large. To reduce the redundancy of the texture features, the omni-direction approach was tested. Different from calculating texture features from GLCM at one direction, the co-occurrence matrix was generated in each direction and then added together for processing. In this case, the variables used for random forest classification were lowered from 32 to 8 texture variables. As a result, an accuracy of 82 % was achieved. The Confusion matrix of the classification result is presented in Table 2.4 to the right.

Table 2.4. Confusion matrix from random forest classification

CLASS		Predicted									
		Four direction					*Omni-direction*				
		Stand Initiation	Young Multistory	Understory Reinitiation	Old Growth	**User Accuracy**	Stand Initiation	Young Multistory	Understory Reinitiation	Old Growth	**User Accuracy**
Actual	Stand Initiation	419	22	31	18	85.51%	376	32	52	30	76.73%
	Young Multistory	26	451	23	0	90.20%	30	450	18	2	90.00%
	Understory Reinitiation	17	15	330	38	82.50%	41	21	288	50	72.00%
	Old Growth	17	2	41	440	88.00%	22	1	51	426	85.20%
Producer Accuracy		87.47%	92.04%	77.65%	88.71%		80.17%	89.29%	70.42%	83.86%	
Overall accuracy						86%	Overall accuracy				82%

As demonstrated in Table 2.4, sampling in all directions can significantly reduce the number of variables used in the classification while maintaining similar classification accuracy. Classification accuracy for young multistory stage conditions was similar between the two classifications but was lower for the other stages, potentially due to the solar angle causing the texture variation associated with shadows. The amount of the shadow varied when the tree height, the presence of understory and size of the canopies were different. Stands at young multi-story had the most homogenous texture. Thus, the shadows were uniform and insignificant from GLCM in different directions. On the other hand, the shadows in the stands at stand initiation, and understory reinitiation were less uniform and had a direction associated with the solar angle in their spatial distribution. Therefore, texture features calculated from GLCM at the direction close to the direction of the shadow were quite different from those of the others. However, putting all directions together will minimize this difference and lower the classification accuracy.

To further reduce the variables used for classification, the first four texture features from the variable importance plot were selected to perform the classification. For our study, the most important variables are contrast, variance, mean and dissimilarity (Figure 2.9). Both contrast and dissimilarity measured the

spreading degree of the gray levels or the average gray level difference between neighboring pixels. The contrast values were higher for large local variations within the region. The local window grey-level variance was higher when there was a significant grey-level standard deviation in the local region. When forests develop, and multistory structures grow, the layers of tree crowns and understory reflect as the gray level variance in the texture. To test if such information is sufficient enough to differentiate the forest from young to mature, a random forest classification was performed with an accuracy of 82 %.

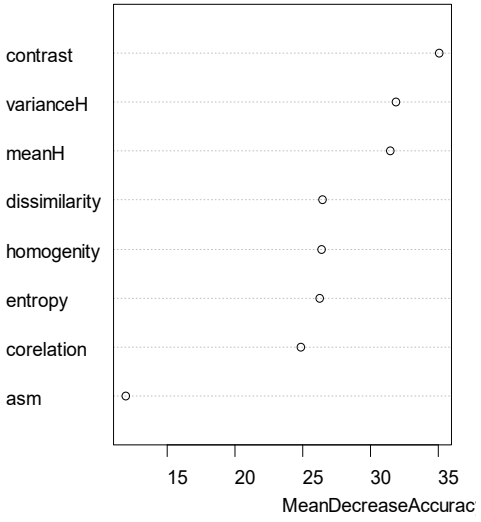

Figure 2.9. Variable importance plots for the forest succession stage classification using GLCM variables. Units are the percentage reduction of resulting classification accuracy from removing one given texture feature.

To analyze the effect of semi-variogram variables range and sill on the overall classification, all variables derived from the GLCM and semi-variogram variables range and sill were used in random forest classification. This resulted in a slight classification accuracy improvement of 0.69%. However, among all the variables, sill was ranked the sixth most important variable and range was the ninth most important variable in random forest classification (Figure 2.10). Overall, the semi-variogram variables did not increase the classification significantly. Calculating range and sill values takes more effort than calculating GLCM variables. While range and sill values were useful for separating the stands at stand initiation stage from the rest, they were not worth calculating for the overall forest succession stage classification.

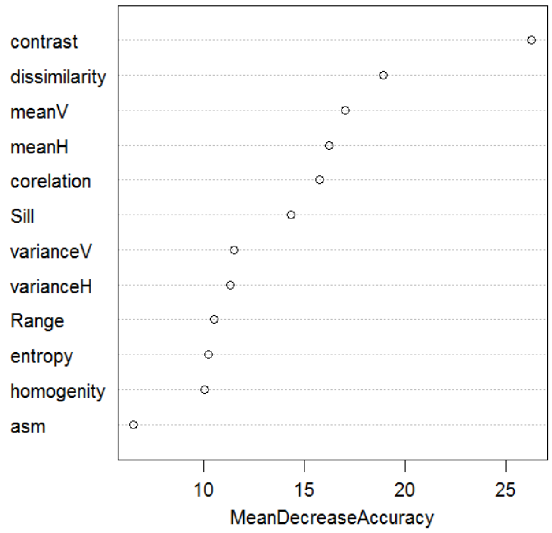

Figure 2.10. Variable importance plots for the forest succession stage classification using both GLCM variables and semi-variogram variables range and sill values. Units are the percentage reduction of resulting classification accuracy from removing one given texture feature.

Adding shadow fractions, together with the variables derived from the GLCM, resulted in improved classification accuracy in a Random Forest classification (89%), and shadow fraction was ranked the most important variable (Figure 2.11). Specifically, adding the shadow fraction improved the differentiation of the stands at old growth stage from stands at understory reinitiation, and the stands at stand initiation from stands at young multi-storey. However, this did not improve the classification between stands at young multistory and understory reinitiation.

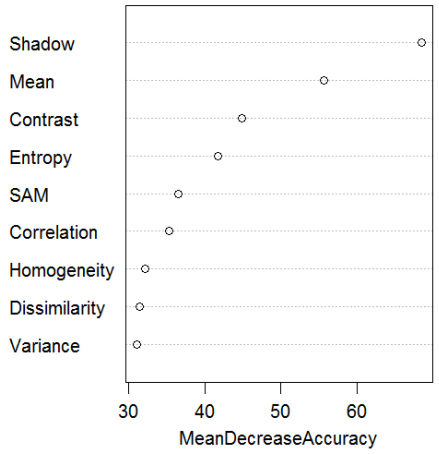

Figure 2.11. Variable importance plots for the forest succession stage classification using GLCM variables and shadow fractions. Units are the percentage reduction of resulting classification accuracy from removing one given texture feature.

Random forest classification was performed with the variables derived from the GLCM and VTMR derived from tree clumping. To provide spatial consistency, all metrics were calculated within a 50 pixels by 50 pixels window. Overall, adding the VTMR decreased the classification to 78%. Specifically, adding the VTMR improved the correctly classified stands at stand initiation and old growth, but greatly affected differentiating the stands at understory reinitiation from the other stages (from 72% down to 59%). It is postulated that this result occurred because the shadow distribution metrics best describe the scene of a large area. When calculated within a sampling unit (400 square meters), it was a poor indicator to separate the different stages. Since the VTMR failed to increase the

overall classification accuracy, the variable was not included in the classification. Finally, the classification scalability was tested at the coarser resolutions. To compare the classification accuracy quantitatively, a set of lower resolution images were resampled from the original image. As shown in Figure 2.12, the classification accuracy decreased with the image resolution decreased. This can be explained by the fact that in very high-resolution imagery, detailed information is revealed from the texture used to aid in distinguishing different classes. With coarser resolution imagery information content is smoothed and made less distinct which cannot provide sufficient information to separate classes. However, it should be noted that high-resolution image computation was computer processing intensive and extensive for large area data collection, while satellite imagery came at a greater availability. Based on our findings, resolution of 2 meters was good for large area habitat mapping, as the image size was five times smaller while the classification accuracy remains above 75%.

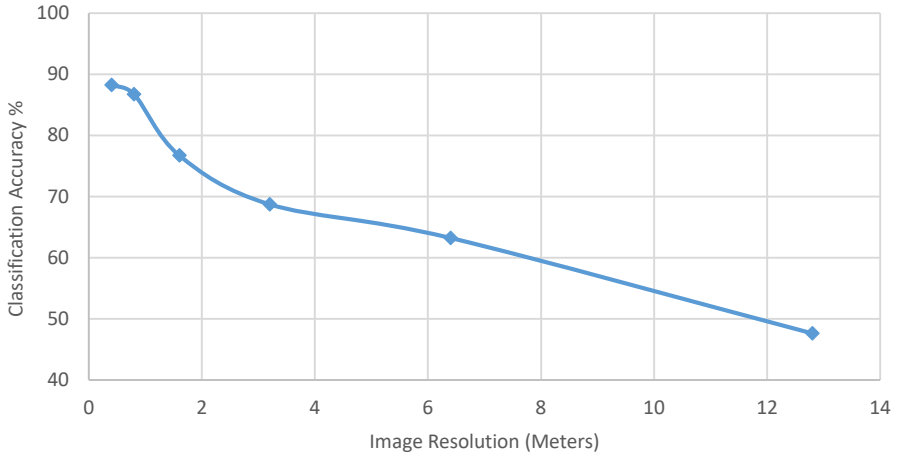

Figure 2.12. Overall random forest classification accuracy results with image resolution changing from fine to coarse.

2.4 Summary

This study on the characterization of the forest successional stages provided a comprehensive investigation of the variables derived from a texture analysis of GLCM, semi-variogram, and spectral variables of shadow fraction and shadow distribution. The result of the RF classification demonstrated that GLCM texture measurements and shadow fraction could differentiate the stages of forest stand development with an accuracy of 89%. The key variables used for the differentiation were contrast, variance, mean, and dissimilarity from GLCM and shadow fraction. The development of forest stands and changes in the canopy

surface created variations between canopies that were measurable by applying spatial pattern analysis. It was that no linear relationship was detected between the semi-variogram parameters and forest succession stages. However, the sill value could be used to distinguish the stands at the stand initiation stage, and the range value to separate stands at young multistory, understory reinitiation, and old growth stages. The cross-validation of the image texture classification using LiDAR derived indices of PLH showed that the classification from young to mature corresponded to the PLH, providing an indication of the agreement of classified forest stages with LiDAR derived indices.

While spatial pattern analysis was able to measure the variations between canopies that were created by the development of forest stands, accurate results (over 70%) could only be obtained from a multispectral imagery that had spatial resolution smaller than 2 meters. Moreover, imagery acquired in the morning or afternoon (low solar angle) was able to achieve similar classification accuracy, as shadow was used to measure the structure difference of the forest stand development. When solar zenith angle was very small, the area of shadow would be limited, and the differences between forest stages became less distinctive.

Chapter 3

Forest roads extraction through a convolution neural network aided method

In this chapter, the work of forest road extraction is presented. Mapping forest roads is important for forest management and wildlife habitat mapping. Forest roads are necessary elements when accessing forestry resources, and their impact on the wildlife habitat can be significant. A convolutional neural network (CNN) aided method for forest road identification and extraction was developed. The algorithm utilized the multivariate Gaussian and Laplacian of Gaussian (LoG) filters and VGG 16 on high spatial resolution multispectral imagery to extract both primary road and secondary roads in forested areas. The algorithm was tested on imagery over two areas in the Hearst forest located in central Ontario, Canada. Based on validation against manually digitized roads, over 74% of the roads from both test areas were successfully extracted.

The research in this chapter is published in the following journal paper:

Zhang, W., & Hu, B. (2021). Forest roads extraction through a convolution neural network aided method. International Journal of Remote Sensing, 42(7), 2706-2721.

3.1 Related work

Mapping forest roads is usually carried out through the manual interpretation of high spatial resolution optical imagery, which is time-consuming and labor-intensive. Several studies have been carried out to automatically extract roads from remotely sensed data (mainly passive optical imagery) based on the fact that roads are linear features with edges and have different spectral signatures from surrounding objects. The existing methods can be categorized as active contour models (snakes) (Butenuth & Heipke, 2012; Ravanbakhsh et al., 2008), mathematical morphology (Pierre Soille & Pesaresi, 2002; Valero et al., 2010; C. Zhang, Murai, & Baltsavias, 1999; Zhu et al., 2005), road tracking (J. Hu, Razdan, Femiani, Cui, & Wonka, 2007; Movaghati, Moghaddamjoo, & Tavakoli, 2010; Tang et al., 2014), segmentation (Máttyus, Wang, Fidler, & Urtasun, 2015; Mena & Malpica, 2005) and classification (Bouziani, Goita, & He, 2010; Shi, Miao, & Debayle, 2013; M. Song & Civco, 2004). Although promising results have been obtained, most are focused on extracting road centerlines from an urban area. A few studies have used LiDAR to detect forest roads with differing of accuracies (Azizi, Najafi, & Sadeghian, 2014; Hrůza et al., 2018; Sherba, Blesius, & Davis, 2014; R. A. White, Dietterick, Mastin, & Strohman, 2010). The detection of forest roads from optical imagery remains underdeveloped. Furthermore, the

distinction between forest roads and their surroundings is different from paved city roads. Consequently, it is difficult to identify effective features to use the abovementioned machine-learning methods.

With the recent advances in the data-driven convolutional neural network (CNN) and fully convolutional networks (FCNs), studies have been carried out to apply them in road detection (Saito et al., 2016; Wei et al., 2017; Zhong, Li, Cui, & Jiang, 2016). Most recently, researchers have combined deep residual networks (ResNets) and the U-Net, an improved FCN model, for improved results with a fewer number of parameters (Gao, Song, Dai, & Chen, 2019; Lu et al., 2019; Z. Zhang, Liu, & Wang, 2018). Although these approaches have promising results, U-net has only been applied to major roads built with concrete or pavement in cities, and the method requires a large number of masked samples for training purposes; however, there is an insufficient number of masked samples available for roads with vegetation coverage or under tree canopy shadows. Moreover, similar to conventional object segmentation, U-net produces the results in a pixel-based segmentation, so the length and geometric constraints of the road are not fully utilized. A deep CNN, meaning the network has been trained from scratch or fine-tuned, is available for road feature classification (Z. Hong, Ming, Zhou,

Guo, & Lu, 2018; Wei et al., 2017). Specifically, VGG 16 (Simonyan & Zisserman, 2014) has been studied as it is currently the most preferred choice for extracting features from images; however, processing image classification with a deep learning network requires intensive computational power. It is resource-consuming to scan an entire forest scene to extract sparse forest roads. A smaller sample size is more favorable for processing when using the deep learning classification.

In this article, a novel method is proposed that utilizes road feature filtering and VGG 16 together. Road feature filtering extracts the road pixels from the spatial correlation and geometric information of road structure knowledge followed by VGG 16 classification for a refined output. This approach was tested on imagery obtained over the Hearst forest in Ontario, Canada, and the results were validated against manually digitized roads.

3.2. Study area and data used

The study area (49° 52'30" N, 84°35'30"W) is located near the town of Hearst, Central Ontario, Canada, as shown in Figure 3.1. This study area falls within the boreal mixed-wood region and covers approximately 1.23 million ha, 1.00

million ha of which is productive forest. The major cover types in this study area include water bodies, forests, roads, and low vegetation. Two study sites with the size of 6.25 square kilometers and 25 square kilometers were selected due to the availability of existing wildlife data because updated disturbance information was needed to support the initiatives of resource managers conducting wildlife-habitat assessments. Two types of roads were examined in this study, as shown in Figure 3.1. The primary road is defined as a wide and paved road with ditches on both sides, which has also been marked as the lifted road. The secondary road is the service road, which is defined as a straight and flat road with full/partial vegetation coverage. The optical imagery was acquired using a Leica ADS-40 in the summer of 2007 during the leaf-on condition. The imagery has four spectral bands (blue, green, red, and near-infrared) with a spatial resolution of 0.4m by 0.4m.

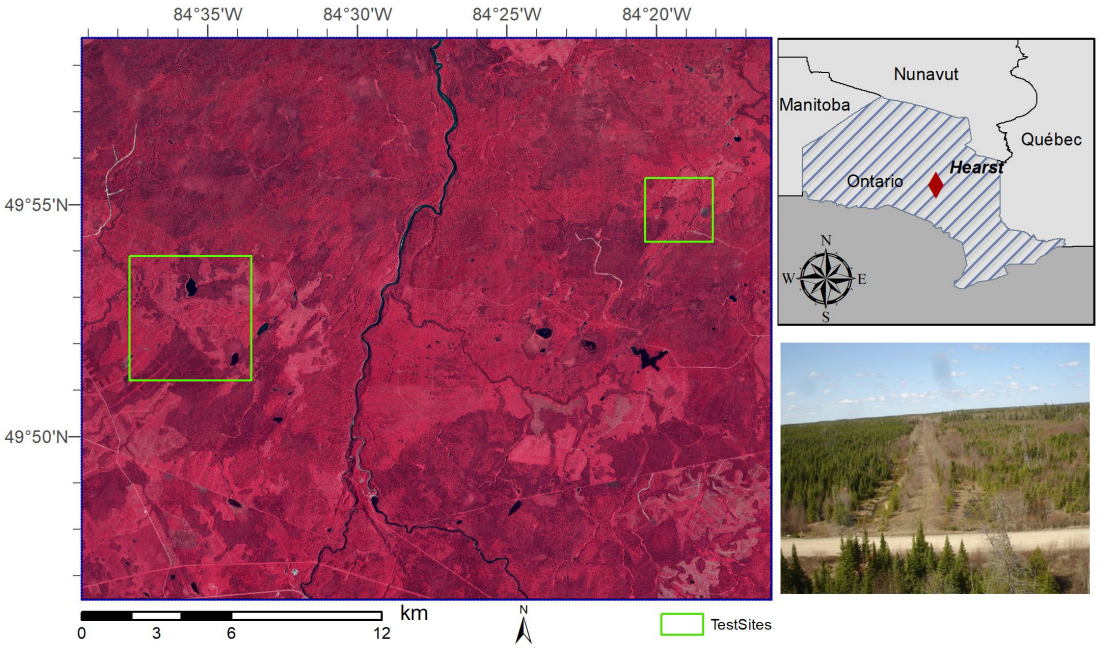

Figure 3.1: The false-color composite of the optical imagery at the study site with the near-infrared band displayed as red, red as green, and green as blue. The test sites are displayed as green rectangles. The photo showing the two types of roads is provided in the lower-right corner.

3.3. Methodology

The proposed method integrates knowledge-based feature filtering and data-driven deep learning approaches, and its diagram is shown in Figure 3.2. A Multivariate Gaussian and its LoG filtering was utilized in the first step to extract potential road pixels. VGG 16 was then used as an aided process to screen out non-road pixels, and a tensor voting method was employed at the end to connect

the detected road pixels and to generate the final road map. These steps are described individually in detail in the following sections.

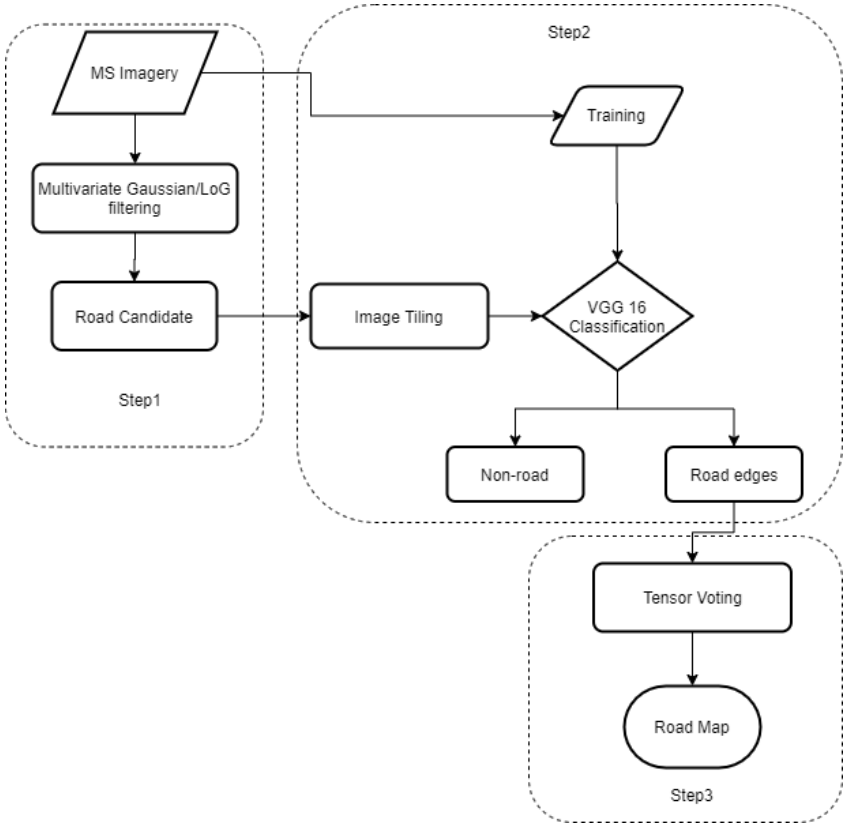

Figure 3.2: The flow chart of the proposed road extraction method.

3.3.1 The extraction of road candidates using feature filtering

As mentioned, primary and secondary forest roads were extracted for this study. The typical paved road was considered the primary road. The secondary roads included narrow dirt roads with trees and bushes on the sides and paths covered by ground vegetation. For fast extraction, the imagery was down sampled into 2 meters by 2 meters resolution. Figure 3.3 shows examples of these roads. Also, the surface of the road features was smooth after the down sampling, and made the filtering process easier. A further examination of the reflectance of these roads revealed that the reflectance of a primary road exhibited a common shape of high values in the middle and low values on the side in the red band, resembling the shape of a Gaussian function (Figure 3.3). The secondary road had a different spectral signature. It was found to have a valley in the middle and peaks on the side in the red band, similar to the shape of the Laplacian of Gaussian (LoG), as shown in Figure 3.3. Based on the observations, customized Gaussian and LoG filters were generated to extract all potential road candidates. Red band was employed in the extraction as such shapes were not as obvious in other bands or bands combined. Also, rather than using the commonly used symmetric 2-dimensional (2D) (Jing, Hu, Noland, & Li, n.d.), Gaussian filters with the shape of elongated ellipsoids were generated with different standard

deviations for different variables, as shown in Equation 3.1. The corresponding Laplacian of Gaussian (LoG) is shown in Equation 3.2.

$$p(\mathbf{DN};\boldsymbol{\mu},\sum) = \frac{1}{2\pi\sigma_x\sigma_y}\exp\left(-\frac{1}{2\sigma_x^2}(\mathrm{DN}_x-\mu_x)^2-\frac{1}{2\sigma_y^2}\left(\mathrm{DN}_y-\mu_y\right)^2\right)$$

$$\mathbf{DN}=\begin{bmatrix}\mathrm{DN}_x\\ \mathrm{DN}_y\end{bmatrix}\ ,\ \boldsymbol{\mu}=\begin{bmatrix}\mu_x\\ \mu_y\end{bmatrix}\ ,\quad \Sigma=\begin{bmatrix}\sigma_x^2 & 0\\ 0 & \sigma_y^2\end{bmatrix}$$

(Eq. 3.1)

$$LoG(\mathbf{DN};\boldsymbol{\mu},\sum) = -\frac{1}{\pi\sigma_x^2\sigma_y^2}\left(1-\frac{(\mathrm{DN}_x-\mu_x)^2+\left(\mathrm{DN}_y-\mu_y\right)^2}{2\sigma_x\sigma_y}\right)\exp\left(-\frac{1}{2\sigma_x^2}(\mathrm{DN}_x-\mu_x)^2-\frac{1}{2\sigma_y^2}\left(\mathrm{DN}_y-\mu_y\right)^2\right)$$

(Eq. 3.2)

In Equation 3.1 and Equation 3.2, DN_x, DN_y, and the vector $\mathbf{DN}$ represent the radiometric response (digital number) in the red band of a given pixel location *(x,y)*, μ_x, μ_y are the mean reflectance , and $\sum$ is a diagonal matrix with σ_x, σ_y representing the standard deviations.

Figure 3.3 shows the designed Gaussian and LoG filters in comparison with the spectral shape of the two types of the roads. The shape of the multivariate Gaussian shows a close representation of the primary road, and the Laplacian of

the multivariate Gaussian has a narrow stripe shape that represents the spectral shape of the secondary road.

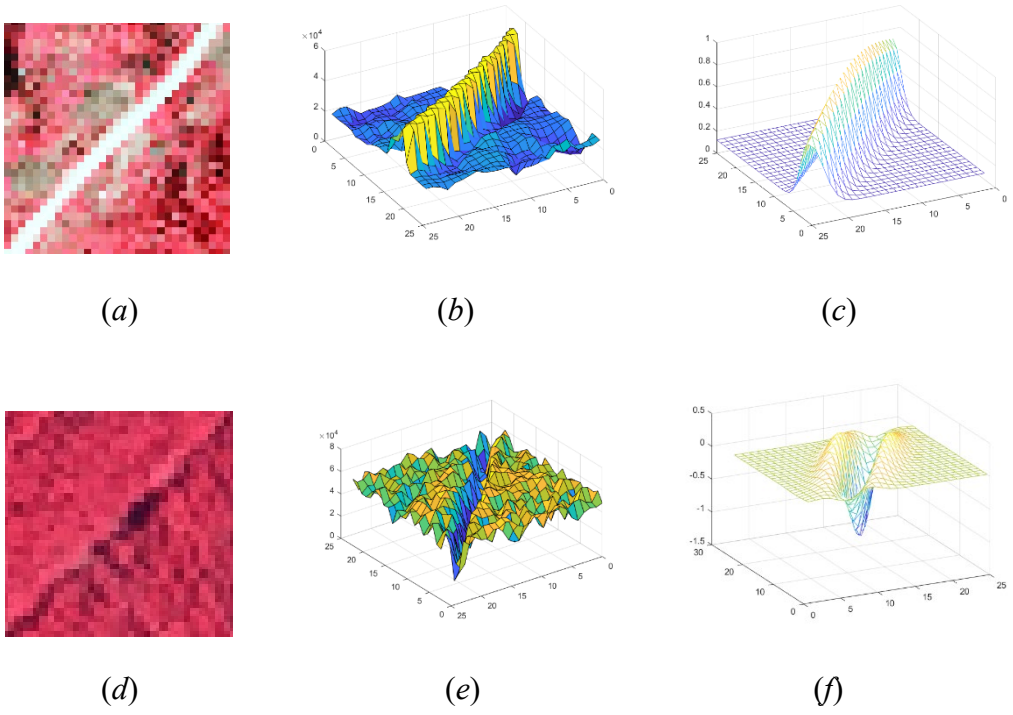

(*a*) (*b*) (*c*)

(*d*) (*e*) (*f*)

Figure 3.3: Road shapes. (a) Primary road observed from the false color image. (b) The spectral shape of the primary road from the red band with the height variation represented by the spectral intensity of the pixels. (c) Designed multivariate Gaussian filter at 30 degrees. (d) Secondary road observed from the false color image. (e) The spectral shape of the secondary road from the red band with the height variation represented by the spectral intensity of the pixels. (f) Designed multivariate LoG filter at 30 degrees.

To locate the roads with different directions, the filters were designed to be

rotated at a set of angles from 0 to 180 degrees in a step of 30. The road feature filtering process was performed at each angle individually and then added together. Since the two types of the roads behaved differently in terms of the spectral shape, a different set of parameters of the filters were set based on the sample road features. Details of how those parameters affected the extraction process are presented in the results and discussion section. The Figure 3.4 shows the resulting response map computed from filtering using one of the Gaussian filters and one of the LoG filters.

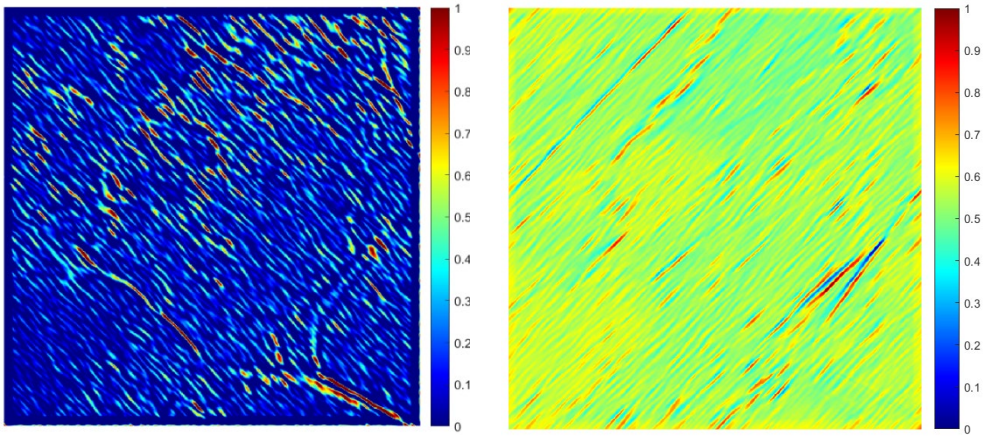

(*a*) (*b*)

Figure 3.4: (a) Filter response map generated from the 30-degree multivariate Gaussian filter and the road image with the color from red to blue indicating the response from high to low. (b) Filter response map generated from the 120-degree LoG and the road image with the color from red to blue indicating the response from high to low.

As shown in Figure 3.4, the color shaded red to blue indicates the variation of the filtering response decreasing from 1 to 0. A value close to 1 indicates a higher likelihood of a road candidate, and a value close to 0 indicates a non-match. A threshold value of 0.7 was chosen to filter out the candidate road pixels.

3.3.2 Classification for road edges using VGG 16

Consider the fact that the filtering process can pick up other edge features that are very similar to the road features, such as the edge of the ponds, water creek or the forest. A deep learning network was used to filter out the no-road pixels from the candidates generated by the previous step. The VGG 16 network utilized in this study is shown in Figure 3.5. The network is characterized by its simplicity, using only 3×3 convolutional layers stacked on top of each other in increasing depth and max pooling to reduce volume size. Two fully-connected layers, each with 2,048 nodes, are then followed by a softmax classifier.

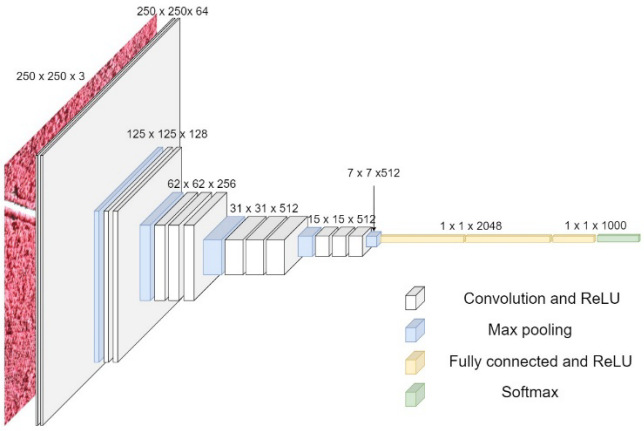

Figure 3.5: The structure of the VGG network.

The input data are the four bands of the multispectral aerial image, whereas the output is the class type of the edge pixel. Two types of edges are defined in the training images. Type 1 refers to roads including primary roads and secondary roads, and Type 2 refers to non-road edges, including forest edges and water creeks (Figure 3.6). To maximize the training data size for the convoluted network, the entire Hearst forest area was employed. As a result, about 15% of the training were selected within the test site 1 and test site 2, and the rest were selected outside these two areas. The generation of the training dataset consisted of 100 to 200 images per class. After rotation, mirroring, and flipping, the training dataset had 1672 samples in total. The individual patches measured 250x250 pixels.

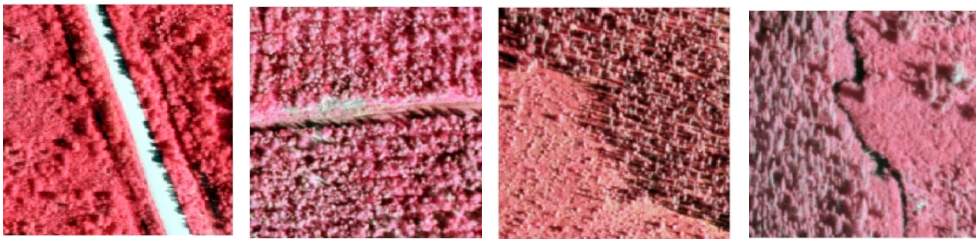

(*a*) (*b*) (*c*) (*d*)

Figure 3.6: Sample image patches of all three classes used in the classification. The images are in the size of 250x250 pixels. (a) Edge type 1, Primary road; (b) Edge type 1, secondary road; (c) Edge type 2, Forest edge; and (d) Edge type 2, water creek.

To train the network, 65 percent of the data was fed into the 21 convolutional layers of VGG 16 to extract the hierarchical features of the edges. The classification accuracy reached 93% after 100 epochs. Details of the convolution layers are listed in Table 1.

Table 3.1. The network structure of VGG 16

Layer (type)	Output Shape	Param #
input_1 (InputLayer)	(None, 250, 250, 3)	0
block1_conv1 (Conv2D)	(None, 250, 250, 64)	1792
block1_conv2 (Conv2D)	(None, 250, 250, 64)	36928
block1_pool (MaxPooling2D)	(None, 125, 125, 64)	0
block2_conv1 (Conv2D)	(None, 125, 125, 128)	73856
block2_conv2 (Conv2D)	(None, 125, 125, 128)	147584
block2_pool (MaxPooling2D)	(None, 62, 62, 128)	0
block3_conv1 (Conv2D)	(None, 62, 62, 256)	295168
block3_conv2 (Conv2D)	(None, 62, 62, 256)	590080
block3_conv3 (Conv2D)	(None, 62, 62, 256)	590080
block3_pool (MaxPooling2D)	(None, 31, 31, 256)	0
block4_conv1 (Conv2D)	(None, 31, 31, 512)	1180160
block4_conv2 (Conv2D)	(None, 31, 31, 512)	2359808
block4_conv3 (Conv2D)	(None, 31, 31, 512)	2359808
block4_pool (MaxPooling2D)	(None, 15, 15, 512)	0
block5_conv1 (Conv2D)	(None, 15, 15, 512)	2359808
block5_conv2 (Conv2D)	(None, 15, 15, 512)	2359808
block5_conv3 (Conv2D)	(None, 15, 15, 512)	2359808
block5_pool (MaxPooling2D)	(None, 7, 7, 512)	0
global_average_pooling2d_1 (	(None, 512)	0
dense_1 (Dense)	(None, 2048)	1050624
dense_2 (Dense)	(None, 2048)	4196352
dense_3 (Dense)	(None, 3)	6147

Total params: 19,967,811
Trainable params: 19,967,811
Non-trainable params: 0

To filter out the road edges from all edge candidates, image tiles were generated from the study area. As the original spatial resolution (0.4 meter by 0.4 meter) was utilized here, the edge pixels were indexed and resampled back. A moving window with the same size as the training patch (250x250 pixels) was used to search over the study area. When the edge pixels were detected in the moving window, the multispectral image within that window was clipped and saved for further classification. After the moving window searched over the entire image, all the tiles were processed with the trained VGG 16 network. A classified label was used to filter the edge pixels associated with the tile. For example, if the classified label was type 1, the edge pixels within the area were saved as the road. On the other hand, if the type 2 label was generated, the corresponding edge pixel values were set to zero.

3.3.4 The generation of road mapping using tensor voting

After the final road pixels were located, post-processing was performed to connect the road pixels and to remove the non-road features. To connect the road pixels into continuous road features, tensor voting was employed (Medioni, Tang, & Lee, 2000).

In a binary image, a pixel can be encoded as a second-order symmetric tensor $\boldsymbol{T}$ and is defined as:

$$\boldsymbol{T} = [\overrightarrow{\boldsymbol{e_1}} \quad \overrightarrow{\boldsymbol{e_2}}] \begin{bmatrix} \boldsymbol{\lambda_1} & 0 \\ 0 & \boldsymbol{\lambda_2} \end{bmatrix} \begin{bmatrix} \overrightarrow{\boldsymbol{e_1}} \\ \overrightarrow{\boldsymbol{e_2}} \end{bmatrix} \qquad \text{(Eq. 3.3)}$$

where $\boldsymbol{\lambda_1} \geq \boldsymbol{\lambda_2} \geq 0$ are eigenvalues, and $\overrightarrow{\boldsymbol{e_1}}$, $\overrightarrow{\boldsymbol{e_2}}$ are the eigenvectors corresponding to $\boldsymbol{\lambda_1}$, and $\boldsymbol{\lambda_2}$.

By applying the spectrum theorem, the tensor $\boldsymbol{T}$ in Equation 3.3 can be expressed as a linear combination of three basis tensors (ball, plate, and stick), as in Equation 3.4.

$$\boldsymbol{T} = (\boldsymbol{\lambda_1} - \boldsymbol{\lambda_2})\overrightarrow{\boldsymbol{e_1}}\overrightarrow{\boldsymbol{e_1}}^T + \boldsymbol{\lambda_2}(\overrightarrow{\boldsymbol{e_1}}\overrightarrow{\boldsymbol{e_1}}^T + \overrightarrow{\boldsymbol{e_2}}\overrightarrow{\boldsymbol{e_2}}^T) \qquad \text{(Eq. 3.4)}$$

where $\overrightarrow{\boldsymbol{e_1}}\overrightarrow{\boldsymbol{e_1}}^T$ describes a stick (surface) with associated saliency $(\boldsymbol{\lambda_1} - \boldsymbol{\lambda_2})$ and normal orientation $\overrightarrow{\boldsymbol{e_1}}$, and $(\overrightarrow{\boldsymbol{e_1}}\overrightarrow{\boldsymbol{e_1}}^T + \overrightarrow{\boldsymbol{e_2}}\overrightarrow{\boldsymbol{e_2}}^T)$ describes a plate (curve) with associated saliency $\boldsymbol{\lambda_2}$ with no orientation preference.

Tensor voting was carried out on the initial tensor after encoding, and tensors communicate their information with each other in a neighborhood. After decomposition, the stick tensor saliency and the ball tensor saliency were used to automatically connects the discontinued road pixels. The tensor voting process

has the original road shapes preserved, and the final road map is generated. For representation and quantitative analysis purposes, the results have been further converted into polylines and saved as shapefiles.

To validate the forest road extraction results, a quantitative analysis was performed with manually digitized roads. The following three cases were considered: 1) True Positive (TP): The road lines generated from the proposed method overlapped with the manually digitized lines within a search radius of six meters (standard forest road width); 2) False positive (FP): The road lines generated from the proposed method did not overlap with the manually digitized lines within a search radius of six meters (standard forest road width); and 3) False negative (FN): The portion of the manually digitized lines did not overlap with any of the roads from the proposed method within a search radius of six meters (standard forest road width). In all three cases, the sum of the road length was calculated.

To further assess the accuracy of the extracted roads, quality measures defined by Wiedemann et al. 1998 (Wiedemann, Heipke, Mayer, & Jamet, 1998) were adopted. Completeness (*C*m) represented the ratio of the records correctly extracted to the total number of relevant records within the ground-truth data (Equation 3.5); Correctness (*C*r) represented the ratio of the number of relevant

records extracted to the total number of relevant and irrelevant records retrieved (Equation 3.6); and Quality (Q) measured of the goodness of the final result (Equation 3.7).

$$Cm = \frac{TP}{TP+FN} \quad \text{(Eq. 3.5)}$$

$$Cr = \frac{TP}{TP+FP} \quad \text{(Eq. 3.6)}$$

$$Q = \frac{TP}{TP+FP+FN} \quad \text{(Eq. 3.7)}$$

3.4. Results and Discussion

The results of the primary edge pixels generated from filtering are shown in Figure 3.7(a). A visual evaluation of Figure 3.7(a) indicates that most of the roads have been correctly identified, especially for the primary roads that are wide and have distinct boundaries from the surroundings. Secondary roads that pass through the woods have been successfully identified as well. This demonstrates the advancement of the proposed method, as others often fail to detect such roads; however, the process is unable to identify all the roads from the open area, i.e., roads passing bare soil. The reason for the unsatisfactory result is that the filter process is based on the assumption that road features are close to

the Gaussian or LoG surface, while the roads in the open area with bare soil on both sides do not satisfy the criteria.

While the aim of road candidate filtering is to detect all the road features, it also detects other edge pixels that represent a similar shape of the road, such as water creek banks and the edges of the forest. It was not trivial to remove the falsely included road features, especially the edges of forests. Different thresholding and filters based on different features were attempted, but no satisfactory results were obtained. It was difficult to find and describe the spatial attributes that were systematic differences between roads and other linear features. As described in the methodology, a deep-learning network was, therefore, employed to eliminate the commission error by separating the pixels into the road and non-road features, including the edges and paths of the forest, and the water creeks. The results of the filtered road pixels are shown in Figure 3.7(b). The classification results showed that the paths within the forest and along the sides of the roads have been successfully classified as non-road pixels and eliminated, while one water creek in the lower-right corner was falsely classified as a road pixel. The reason is that part of the water creek had a spectral shape that was similar to the service road and thus was not separated as a non-road pixel.

The final road map overlaid with a red band from the original image is shown in

Figure 3.7(c). The visual comparison against manually digitized roads in Figure 3.7(d) shows that most of the roads were successfully extracted, while some secondary roads or parts of them are missing. This study area is challenging due to a large number of roads that are partially occluded, which creates a non-uniformed spectral shape that makes it difficult for filtering, resulting in an incomplete extraction of these secondary roads.

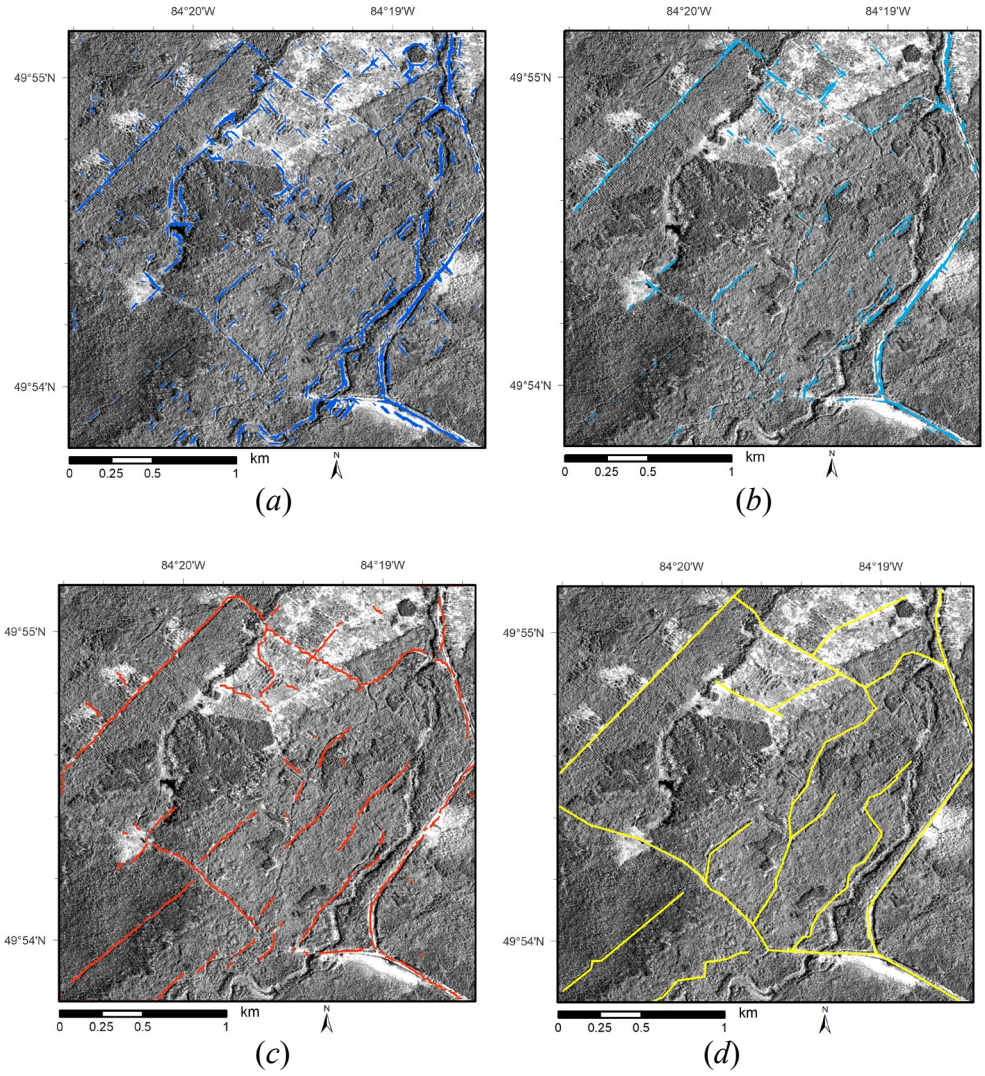

Figure 3.7: Road extraction results from the proposed CNN aided method. (a) Road features generated from initial LoG filtering with each pixel indicated by blue lines, and the background is optical imagery. (b) Filtered road candidates generated from CNN indicated by blue lines, and the background is the false-color optical imagery. (c) Final forest road detection result after post-processing. Each road is indicated by red polylines, and the background is the red band of optical imagery. (d) Manually digitized roads in yellow lines, provincial road segments in blue lines, and the background is the red band of optical imagery.

A second test area was selected to further validate the proposed method. The results of the primary road pixels generated from feature filtering are shown in Figure 3.8(a). Similar results to Figure 3.7(a) indicate that most of the roads have been correctly identified, especially for the primary roads that are wide and have distinct boundaries from the surroundings. Secondary roads that pass through the woods have been successfully identified as well. Commission errors occurred at the edge of the lake and at the boundary of the managed forest. The results of the deep-learning network filtered road pixels are shown in Figure 3.8(b). The classification results showed that the edge of the lake and the paths within the forest were successfully eliminated. On the other hand, the edges of the managed forest, shown as squares in the upper-left corner, were falsely classified as road pixels. The reason is that parts of the edges are very straight and very close to the spectral of the service road and thus were not separated as non-road pixels. The final road map overlaid with a red band from the original image is shown in Figure 3.8(c). The visual comparison against manually digitized roads shown in Figure 3.8(d) demonstrates that most of the roads were successfully extracted.

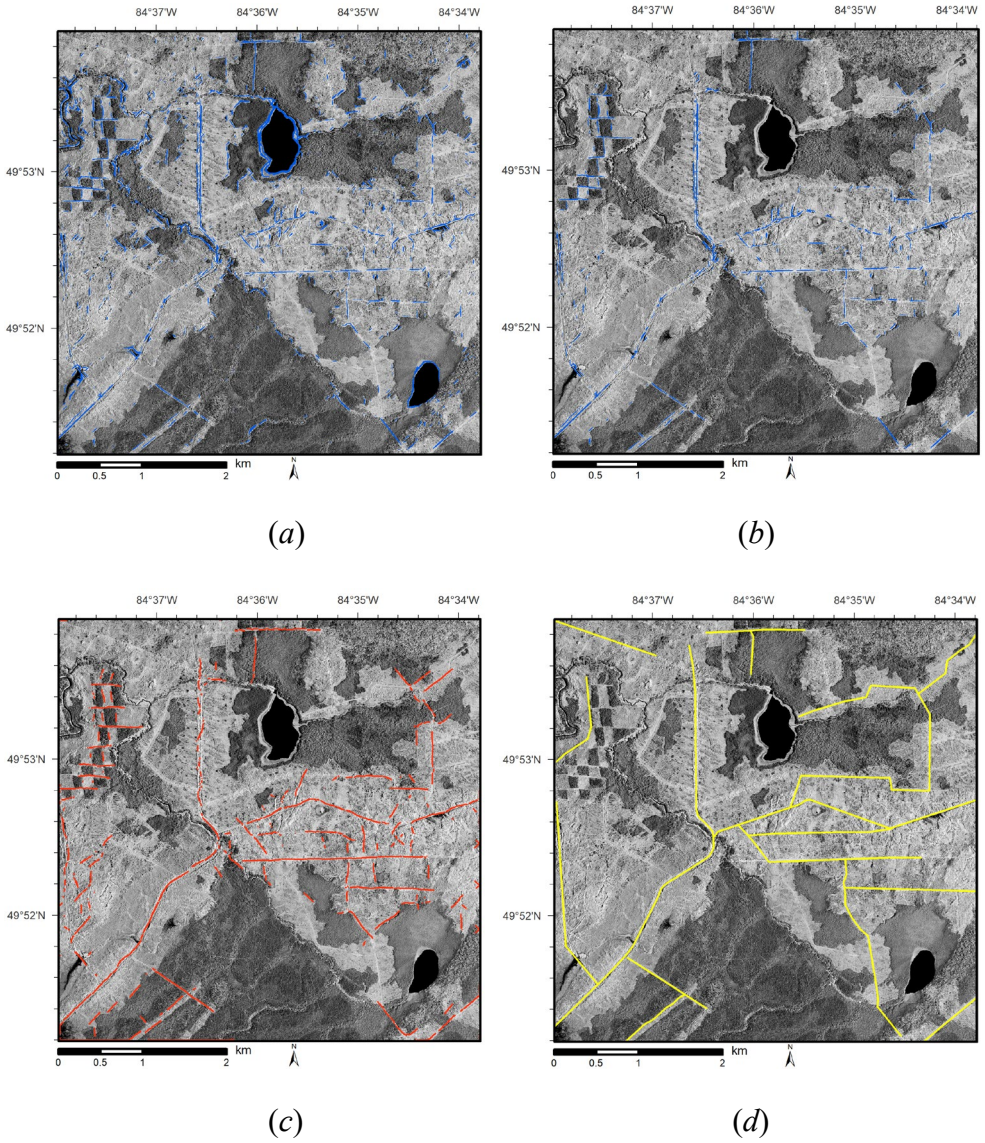

Figure 3.8: Road extraction results of test area 2 from the proposed CNN aided. (a) Road features generated from initial LoG filtering with each pixel indicated by blue lines, and the background is the red band of optical imagery. (b) Filtered road candidates generated from CNN indicated by blue lines, and the background is the red band of optical imagery. (c) Final forest road detection result after post-processing. Each road pixel is indicated by red lines, and the background is the red band of optical imagery. (d) Manually digitized roads are in yellow lines, and the background is the red band of optical imagery.

As shown in Figures 3.7(a) and 3.8(a), the roads detected from the LoG filtering included many non-road features, led to high commission errors. Especially, the secondary roads with indistinct boundary and partial/full vegetation coverage were difficult to be extracted accurately. This was expected and was the reason that CNN was used in this study to further refine the filtering results. It was worth mentioning that different traditional machine learning methods, such as various supervised and unsupervised classification methods and different thresholding methods were also attempted, but the results were not satisfactory.

In addition, the network connectivity or polyline curvatures would not be able to distinguish the false features from roads, since the process would occlude all edge features based on the locations and generate the erroneous result. For example, the water creek that crossed the road would be treated as two roads intersected, and falsely detected edges that were very close to, or passing by the true road features would be treated as sub-branch of the road.

Notably, the imagery was down sampled to a spatial resolution of 2 meters by 2 meters during the filtering process. In the filtering process, the shape of the road was an important feature. The detailed features on road surfaces exhibited on the imagery in the original resolution (0.4 meters by 0.4 meters) were not necessary and had a negative impact. However, the imagery at the original resolution was

used in the VGG 16 classification, as the detailed features on the road surface and its surroundings were needed to separate forest roads from other similar linear landmarks such as forest edge and creeks.

To quantitatively evaluate the forest road extraction results, manually digitized shapefiles were used to validate the accuracy of the classifications, and the results are shown in Table 2. As illustrated by Table 2, the overall *C*m for site 1 and site 2 has an average of 79%, where site 1 has a *C*r of 75%, and site 2 has a lower correctness of 71%.

Table 3.2. The assessment of classification accuracy

		Site 1	***Site 2***
Prediction	*C*m (%)	81.05	65.72
	*C*r (%)	74.95	70.68
	Q (%)	63.77	51.64

To further demonstrate how the size and the shape of the LoG filter affect the road identification results, three different filters were tested. The filters and their corresponding filtering results are shown in Figures 3.9(a)-(f). It can be observed that with a filter width from narrow to wide, the number of road pixels identified decreased; however, with the narrowed filter, falsely identified objects appeared

more often in the results. There is always a tradeoff between the number of subjects identified and the commission error. The more road pixels to be identified, the more noise that will occur. To balance the results and their commission errors, a filter was chosen based on the road samples.

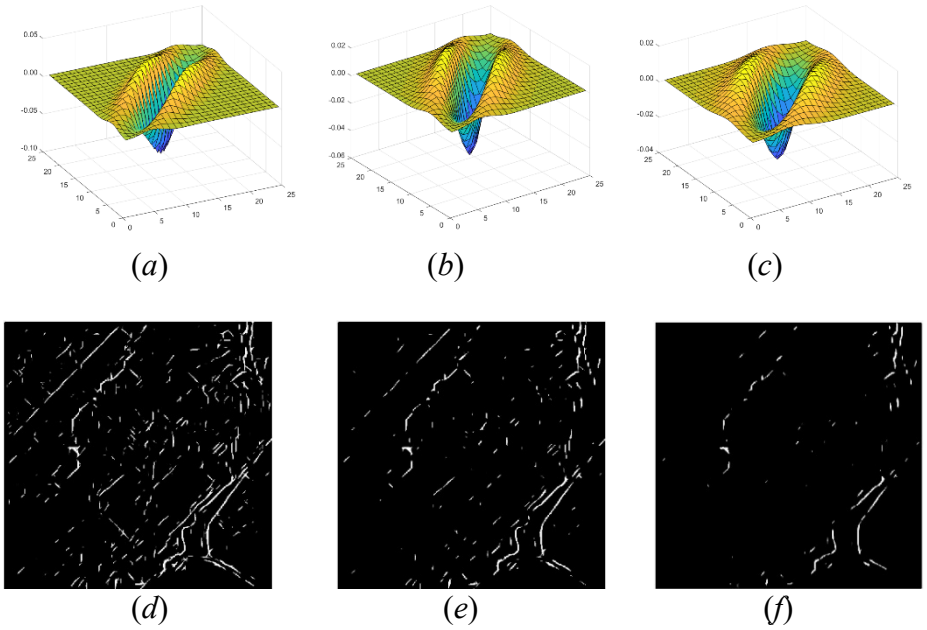

Figure 3.9: Effects of filter shape on LoG filtering results. (a) LoG filter with x-direction std = 1.75. (b) LoG filter with x-direction std =2.25. (c) LoG filter with x-direction std =2.75. (d) Road pixels resulting from filter (a). (e) Road pixels resulting from filter (b). (f) Road pixels resulting from filter (c).

In addition to the shape of the filter, window size influences the LoG filtering results. Therefore, three different filters were tested. The filters and their corresponding filtering results are shown in Figures 3.10(a)-(f). A small window that includes part of the filter cannot identify most of the roads. On the other hand, when the window size increased to a size greater than the filter, the number of road pixels detected did not increase, but more noise appeared. In this study, a window size that best fit the filter was used to identify as many roads as possible while maintaining a minimum of noise.

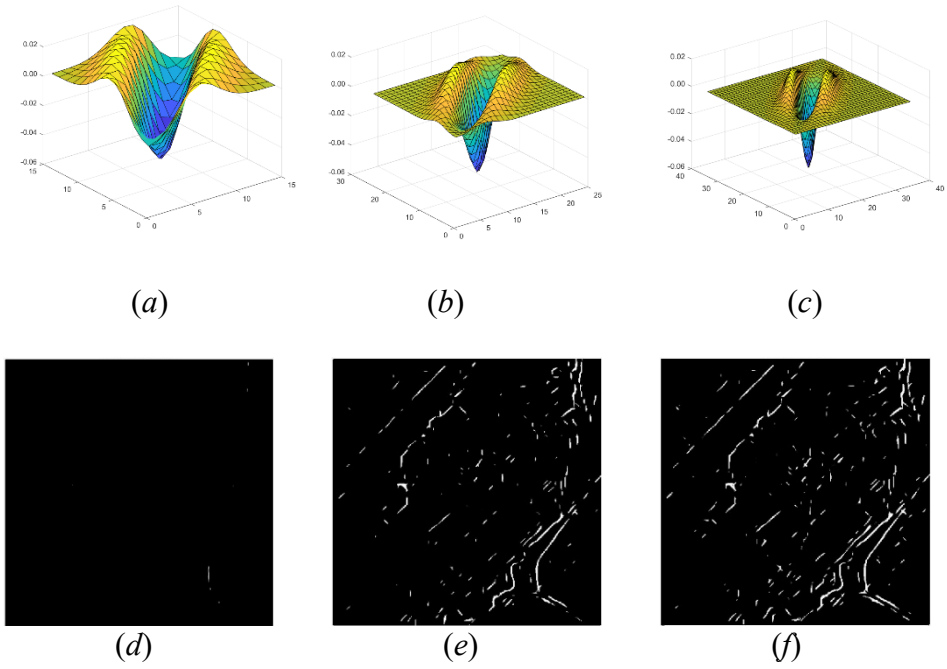

Figure 3.10: Effects of window size on the LoG filter results. (a) LoG filter with window size = 15. (b) LoG filter with window size =25. (c) LoG filter with window size =35. (d) Road pixel resulting from filter (a). (e) Road pixels resulting from filter (b). (f) Road pixels resulting from filter (c).

3.5 Summary

This study focused on forest road extraction through a novel method that utilized road feature filtering and VGG 16 together. Based on the spectral shapes of the primary and secondary forest roads, a multivariate Gaussian and its LoG

were utilized to extract road feature candidates from the imagery. VGG 16 was then employed to remove the false identified road candidates. Tensor voting was used for post-processing and the generation of the final road network. The novelty of this study was that the proposed method could be used to extract vegetation-covered secondary roads, which had not been achieved in previous investigations. The results of the proposed method demonstrated the ability to accurately detect all primary roads and to extract secondary roads that were shaded or vegetation-covered. Based on the validation against manually digitized roads, the results showed that the proposed method was able to extract forest roads with an average of 74% of completeness. Omission errors were observed for roads with no distinct boundaries, such as non-lifted roads that were partially covered by vegetation or rocks. Commission errors were identified at the edges of the managed forests that were similar to the road features (which were linear and straight).

Notably, the forest roads were extracted based on their Gaussian/Laplacian shaped spectral response, such patterns needed to be observed from the multispectral imagery. Considering the primary road had the width of 6 meters, and secondary road the width of 3 meters (measured from the imagery of the study site), the smallest filter window size was set as 3 pixels by 3 pixels. As a

result, a higher spatial resolution (< 1 meters) multispectral imagery should be utilized to obtain a similar result.

Chapter 4

Automatic surface water mapping using a robust thresholding method from SAR data

In this chapter, the work of open water and flooded vegetation quantification is presented. Surface water bodies are the most significant resources on our planet. Human activities, climate, and other environmental changes impact on the locations and sizes of open water bodies, which in turn, can affect surrounding environments, biodiversity, and wildlife. A fully automatic method based on robust stepwise thresholding was developed to map and track the change in the extent of surface water using Polarimetric SAR data. The application of this method has been applied in both Radarsat-2 and Sentinel-1 data in central Ontario, Canada. It was demonstrated that the developed robust stepwise thresholding approach could facilitate rapid mapping of open water areas with a promising accuracy of over 95%. In addition, the time-series extent of surface

water extracted from May 2008 to August 2016 reveals the dynamic nature of surface inundation, and the trend was consistent with the local precipitation data.

The research in this chapter is published in the following journal paper:

Zhang, W., Hu, B., & Brown, G. S. (2020). Automatic surface water mapping using Polarimetric SAR data for long-term change detection. *Water*, 12(3), 872.

I thank the Water, MDPI publisher and other authors who have permitted me to reuse the article in my dissertation.

4.1 Related work

Advanced remote sensing technologies provide an excellent opportunity to obtain spatially extensive and temporally repeated data relevant to mapping surface water (Klein et al., 2014; Sawaya, Olmanson, Heinert, Brezonik, & Bauer, 2003; Smith, Sheng, MacDonald, & Hinzman, 2005; Yilmaz, Adler, Tian, Hong, & Pierce, 2010). With optical imagery, surface water is usually extracted based on the difference in the spectral reflectance between land and water. Water absorbs most of the radiation in near-infrared (NIR) and mid-infrared (MIR), whereas other cover types, such as vegetation, soil, and human infrastructure have a higher reflectance in these spectral ranges. In addition to the direct use of the surface reflectance in multispectral satellite imagery, several indices are commonly employed, including the normalized difference water index (NDWI) that uses the visible wavelength (0.52-0.60 micrometers) and NIR (0.77-0.90 micrometers) and modified normalized difference water index (MNDWI) that uses the visible and Mid-infrared wavelengths (1.55-1.75 micrometers) (Hanqiu Xu, 2006; McFeeters, 1996). Despite the values of such metrics, the acquisition of passive optical data depends on weather conditions and solar illumination, which make it a challenge for them to be used in surface water monitoring. For example, flooding usually happens during the heavy rain, which makes it difficult

for the optical sensors to obtain data of the earth surface covered by clouds (Silveira, Heleno, & IEEE, 2009).

As an active sensor, Synthetic Aperture Radar (SAR) can collect images day or night, and its microwaves can penetrate through most clouds, rain fields, water vapor, and aerosol layers. In particular, as water has a unique signature in SAR imagery, a calm water body behaves as a specular reflector with respect to the radar wavelength and thus appears as a low-intensity area in SAR images. This contrasts with the higher intensity of the rougher surrounding terrain, characterized by diffuse scattering (Hess et al., 2003; Lane & D'Amico, 2010; Touzi et al., 2007; C. Zhou, 2000). However, the contrast is dependent on factors such as polarization and incidence angle of the emitted microwave radiation. For the current Radarsat-2 sensor with an incident angle ranging from 20 degrees to 54 degrees, calm water is considered as specular reflection, and the backscatter is close to zero (Geldsetzer & Yackel, 2009).

Several studies have been conducted to map surface water with SAR data through the thresholding techniques utilizing the low return signal behavior of open water. Specifically, methods include manually-defined histogram thresholding (Santoro et al., 2015; Westerhoff et al., 2013), the Otsu's algorithm (Li & Wang, 2015), radiometric threshold based on a gamma distribution (Liang & Liu, 2020;

Matgen et al., 2011), and set of thresholds based on statistical analysis of the trainings (S Bolanos, Stiff, Brisco, & Pietroniro, 2016; Hong, S., Jang, H., Kim, N., & Sohn, 2015). Those approaches are not fully automatic, and some of them require additional processes to generate surface water map, such as supervised classification approaches (Brian Brisco, 2015; S. Hong et al., 2015; Huang et al., 2018; Morandeira et al., 2016), region growing segmentation (Sandra Bolanos et al., 2016; Manjusree, Prasanna Kumar, Bhatt, Rao, & Bhanumurthy, 2012b; Martinis et al., 2009; Matgen et al., 2011), and machine learning approaches(Qin, Yang, Li, & Sun, 2019; P. Zhang et al., 2019; X. Zhou et al., 2019). Even with their success, these methods require time and human resources and thus are not operational(Santoro et al., 2015; H. K. Zhang & Roy, 2017). In addition, some methods are incident angle-dependent, as higher incident angle data are selected for their high contrast between surface water and land (Martinis et al., 2009; Murfitt, Brown, & Howell, 2018). Although higher accuracy has been achieved, it is not suitable for long term surface water mapping and emergency flood map production as the amount of the data is reduced. A fully automatic and incident angle independent process is thus much needed to support the timely production of mapping the surface water.

In this chapter, a fully automated algorithm is developed to characterize

effectively water bodies using Polarimetric C-band SAR data. Surface water extent was mapped through a robust stepwise automatic thresholding (SAT) approach and validated with a manual digitized surface water inventory. The SAT method was also compared with other commonly used approaches for surface water mapping using NDWI and Otsu's method (Du et al., 2014). To further explore the potential of mapping the surface water at a global scale, the algorithm was tested on both Radarsat-2 and Sentinel-1 SAR data. At last, the algorithm was applied on a time series of RadarSat-2 data to map the surface inundation dynamics.

4.2. Materials and Methods

The study area is located in Ontario, Canada (77° 28' 21" W, 45° 59' 10 " N), as shown in Figure 4.1. It was categorized as the Boreal Shield ecoregion, with the climate was described as generally continental with long cold winters and short warm summers (Marshall, Smith, & Selby, 1996). The historical weather data show the monthly precipitation in the site ranges between 29 mm and 111 mm with the annual temperatures averaged at approximately 4.5 °C. Figure 4.2 shows the specific precipitation data in the area. Also, the area is within the western portion of black duck breeding range with the southern area covered by deciduous forest and transitioning to the northern boreal forest. The

site was selected due to the availability of existing SAR and waterfowl data for individual wetlands, as needed to support initiatives of resources managers conducting wildlife-habitat assessments.

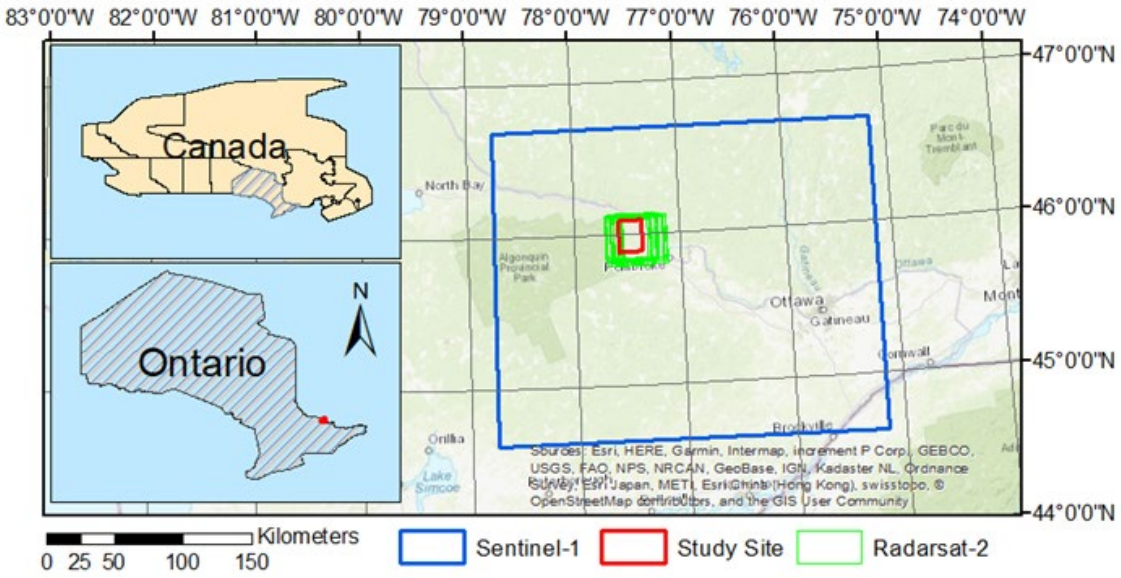

Figure 4.1. The geographic location of the study area with the SAR scenes. The red box on the map indicates the location of the study site and the footprint of the Multi-spectral SPOT imagery. The green boxes indicate the frame footprint of Radarsat-2 data. The blue box indicates the frame footprint of the Sentinel-1 SAR data. The right panel uses the World topographic map from Esri, with the sources from Esri, HERE, Garmin, Intermap, increment P Corp., GEBCO, USGS, FAO, NPS, NRCAN, GeoBase, IGN, Kadaster NL, Ordnance Survey, Esri Japan, METI, Esri China (Hong Kong), swisstopo, OpenStreetMap contributors, and the GIS User Community

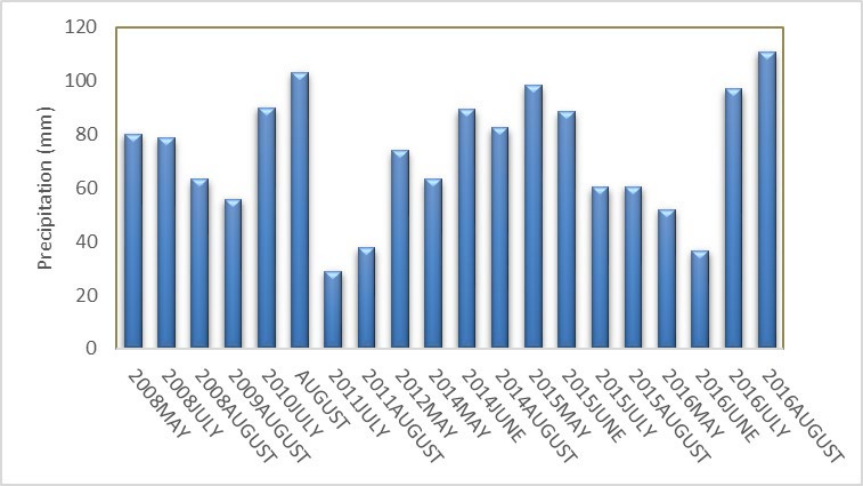

Figure 4.2. Summary of monthly precipitation of the study area for summer in 2008-2016.

This study utilized a total of 51 scenes of C-band (5.405 GHz) Radarsat-2 Single look complex (SLC) images acquired from May 2008 to August 2016. The images all were acquired from Fine Quad (FQ) polarized mode, with a resolution of 5.2 m and 7.7 m in slant range and azimuth, respectively. Also, images were collected in both descending (acquisition time around 11:30 UTC) and ascending (acquisition time around 23:15 UTC) orbits, and from varies beam mode, including FQ4, FQ9, FQ14, FQ18, FQ23 and FQ28 to maximize the number of scenes for the temporal analysis. (Detailed information about the images is listed in Appendix)

Another C-band imager Sentinel-1A with a swath width of 250-km at fine spatial resolution was explored in this study. For algorithm testing, one scene of Dual-polarized (HH/VH) Sentinel-1 SAR data under interferometric wide-swath (IW) mode acquired on June 09, 2016, was first processed to Level-1 ground range detected (GRD), and then downloaded via python download from National Aeronautics and Space Administration Alaska Satellite Facility (NASA/ASF). The spatial resolution was 20.3m and 22.6 m in slant range and azimuth, respectively, and the incident angle was between 32.9 – 43.1 degrees.

A digital elevation model (DEM) was employed to perform the terrain correction on the images, as the images were aligned and corrected for elevation interference to ensure that all SAR images were overlaid with each other and with the cartographic files. The DEM used for this purpose was the South Central Ontario Ortho-photography Project (SCOOP) grid (2 m), generated from the stereo imagery collected between April to May 2013.

To cross-validate the surface water mapped by SAR data, one scene of SPOT-7 imagery acquired on 03 May 2016 was also employed. The multispectral satellite imagery has four spectral bands, blue (450-520nm), green (530-590nm), red (625-695nm), and near-infrared (760-890), and a spatial resolution of 6.6 m. The imagery has been ortho-rectified to be the same georeferenced as the SAR

imagery.

The proposed automatic algorithm consists of three steps: 1) pre-processing of SAR data to generate a backscattering coefficient, georeferenced with a provincial 2m LiDAR derived DEM to correct the relief displacement, and boxcar de-speckle filtering to remove the noise within the data, 2) SAT for generating the water extent map, and 3) post-processing of the image using morphological operations to remove an island within a lake and small misclassified areas (Figure 4.3). The HH polarization was used in this study as it provides the highest contrast between calming open water and land.

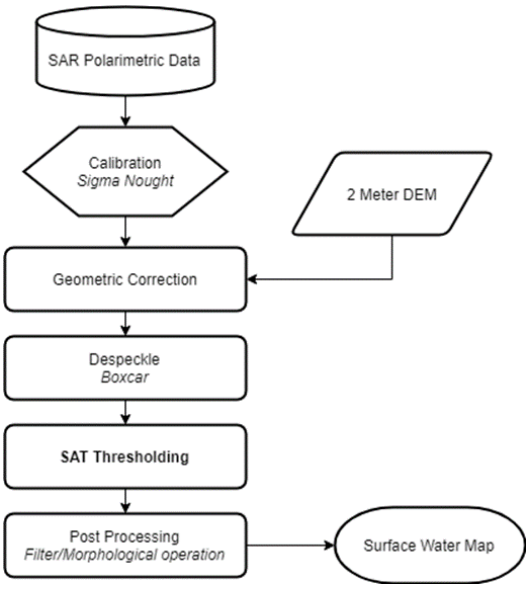

Figure 4.3. The workflow of the proposed water-mapping procedure

The pixel value of the SAR image was determined by the strength of the radar signal reflected from a unit area on the corresponding location in the scene, the backscatter coefficient β_0 was used in calibration to convert the values from the digital number to the reflectivity of the surface objects. Parameter β_0 was the radar cross-section per surface unit of the target with respect to the local incident angle. All SAR data were then converted from raw units to power units (decibels).

Due to the fact that the speckle effect caused by the coherent radiation used by

radar systems was present, the de-speckle filter was employed to remove the salt and pepper noise while preserving edges and textural structures prior to data analysis. In this study, a boxcar filter with a 5-pixel by 5-pixel window was adopted, resulting in a unique valley-hill pattern in the histogram that represented a better distinction between water and non-water bodies, shown in Figure 4.4. The strategy of detecting the bottom of this valley has been proven to be a good threshold that separates water bodies (low backscattering coefficient) and non-water bodies (L. White, Brisco, Dabboor, Schmitt, & Pratt, 2015). Also, this pattern exists in all incidence angle of Radarsat-2 SAR data, not only the higher ones. Thus the normalization between incident angles is omitted in this study. All the pre-processing procedures were designed as a workflow done automatically with python script utilizing the functions provided by PCI Geomatica.

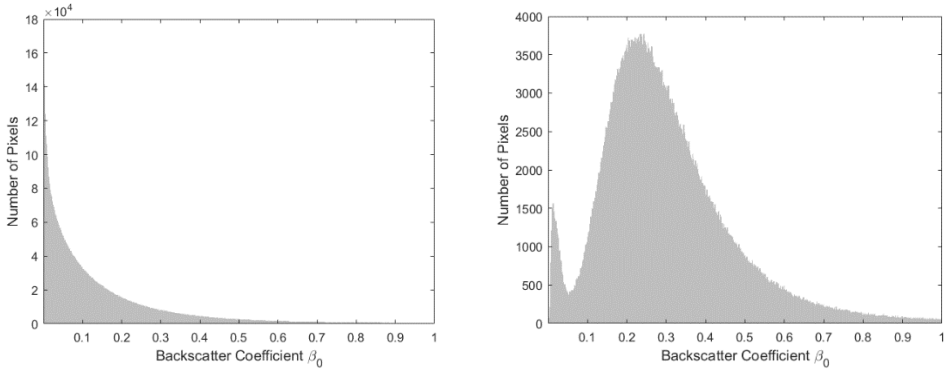

(a) (b)

Figure 4.4. Histograms of HH band. (a) Histogram of original backscattering coefficient in the HH band. (b) Histogram of backscattering coefficient in the HH band after boxcar filtering

To automatically determine the threshold value located at the valley (shown in Figure 4b), a step-wise method was developed. Specifically, a set of third-order polynomials was employed to fit the histogram in a manner of moving steps. The reason for this is the third-order polynomial has the shape that best describes the histogram of backscattering coefficient after boxcar de-speckle, and easy to solve the turning points. Also, as image histogram is rough with notches appeared throughout the curve, using local minimum detection would detect the bottom between any two adjacent notches, and yield multiple results that do not represent the true minimum, i.e. the threshold value. Moreover, due to the roughness of the histogram, using one polynomial to fit the entire histogram would yield a threshold value with significant uncertainty. Therefore, a step-wise polynomial

fitting was the best choice to solve the threshold from the bottom of the valley.

The iterative process started at the beginning of the histogram. First, a partial histogram was extracted. Second, a third-order polynomial was fitted to the selected histogram. Last, the local minimum (turning point) was solved from the first derivative of the polynomial equal to zero. As the third-order polynomial was used, the smaller value of the solution was extracted and recorded as the threshold candidate (Figure 5a). Meanwhile, the difference between the two turning points are calculated, and 1/10 of the result value is stored as the step size. The process continued, and moved with the calculated step size to the next part of the histogram, another polynomial was fitted, and a second threshold candidate was solved (Figure 5b). The iterative process continued until the solved threshold value moved outside the fitting area of the selected histogram (Figure 4.5c). Finally, the optimal threshold value was obtained from fitting through the pre-determined candidates (Figure 4.5d). It is worth mentioning that when the slope of the two sides of the valley is different, i.e. very asymmetric shape, the candidates were scattered along with the histogram rather than clustered at the bottom of the valley. Therefore, fitting through all the candidates instead of simply calculating the average assures the optimal result.

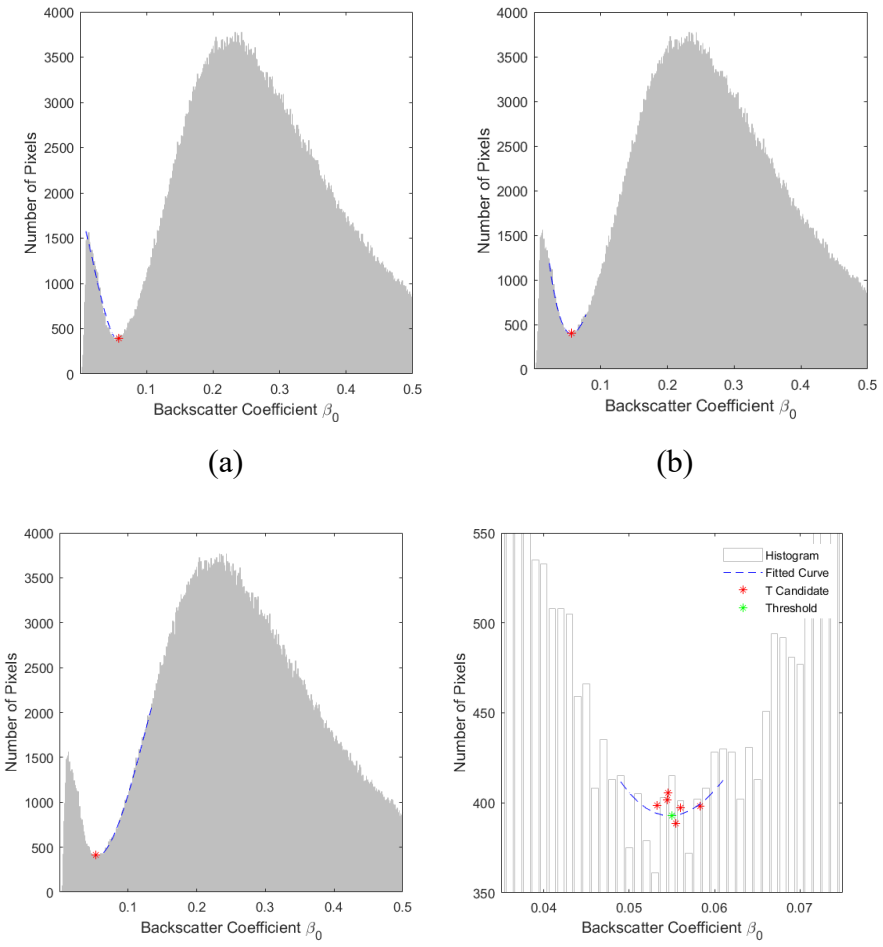

Figure 4.5. Illustration of the automatic histogram threshold generation, where the image histogram was shown as grey color bars, threshold candidates from the step-wise polynomial fitting as shown in red stars, the fitted polynomials were shown in blue curves, and the final threshold was shown in the green star. (a) The first step of threshold candidate generation with a fitted polynomial. (b) Mid-step of threshold candidate generation with a fitted polynomial. (c) Last step of threshold candidate generation with a fitted polynomial. (d) Final threshold generation.

After the threshold was determined, each pixel in the SAR image was classified into either water or land, depending on whether its value was smaller or greater than the threshold, respectively. Post-processing was used to refine the classification result. First, morphologic dilation (P Soille, 2013) was performed by filling any holes or gaps that appeared as "islands" inside the big water bodies. A size filter was applied to clean up the final result when any water region with a size smaller than 3 pixels and isolated was removed.

To further test the proposed automatic thresholding method on different sensor types, one scene of Sentinel-1 data from the same area was employed. For sentinel-1 data pre-processing, the Science Toolbox Exploitation Platform (SNAP) Toolkit developed by the European Space Agency was used. The workflow was built to generate the HH intensity image from high-resolution Level-1 ground range detected products, and then the image has been pre-processed for geocoding, terrain-flatten, and also the signal has been corrected to sigma naught backscatter coefficients (β0). At last, the boxcar de-speckle filter with 5 x5 kernels was used to reduce speckle noise. Terrain flattening and terrain correction was conducted using the recently released Shuttle Radar Topography Mission (STRM) 1 arc-second (approximately 30 m) digital elevation model (DEM) (SRTMGL1).

In addition, the Otsu thresholding method (Otsu, 1979), one of the most commonly used automatic image thresholding techniques, was utilized to obtain another surface water map and compared with the one generated with the proposed SAT method. The threshold value was determined through an iterative process that minimizes the within-class variance at the same time when it maximizes between-class variances.

To access the binary classification generated by the SAT, both qualitative and quantitative analyses were conducted based on the manually digitized shapefile and 7-meter SPOT true color imagery. As the shape and the presence of the wetland can be different between the creation dates, the reference data were visually interpreted using the SPOT imagery.

The last step was to process a total of 51 Radarsat-2 scenes of the overlapping area with the above-mentioned procedure. As the study area has a flat terrain, the displacement introduced by different incident angles was less than one pixel (~7-meter) after geo-referencing with the 2-meter DEM. Surface water bodies were extracted with the proposed SAT method, and the total area of the delineated surface water extent was calculated and plotted against the precipitation data to conduct the time series analysis.

4.3. Results

4.3.1. Surface water classification

The surface water maps generated by the proposed SAT for both Radarsat-2 and Sentinel-1 were presented here. The surface water map generated from Radarsat-2 data, acquired on August 05, 2016, is shown in Figure 4.4a. For comparison, the corresponding manual digitized polygons are shown in Figure 4.6b. The majority of surface water bodies were successfully identified and extracted, with the kappa coefficient k = 0.9822. A few linear water streams are missing in the classification results as omission errors, and a few commission errors are evident near the bottom of the site, which appears to be inundated water or flooded vegetation falsely identified as open surface water.

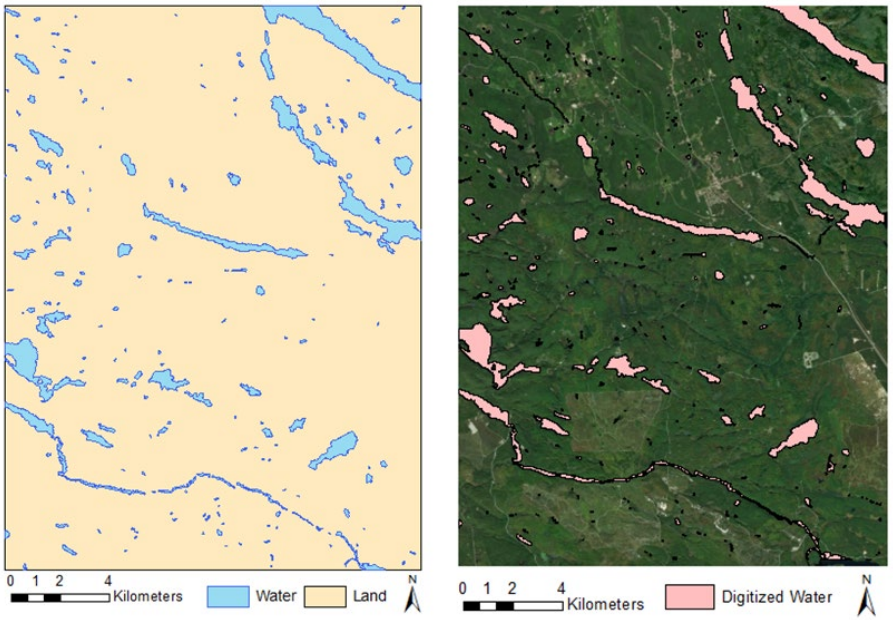

(a) (b)

Figure 4.6. (a) Open water extent map derived from Radarsat-2 Thresholding. Blue polygons indicated identified surface water and the beige background represented the land. (b) Manually digitized polygons were shown in blue overlaid on true color SPOT imagery.

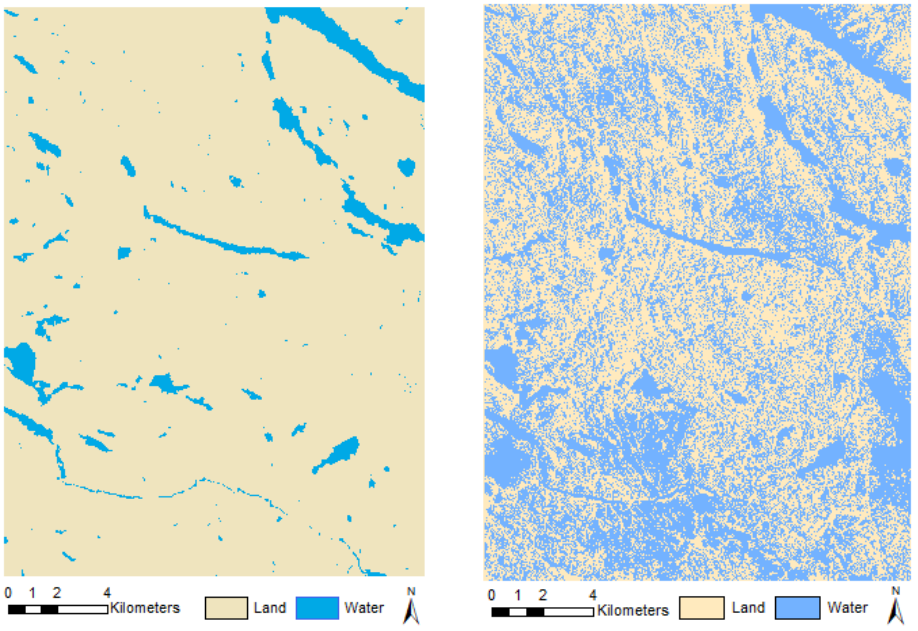

(a) (b)

Figure 4.7. (a) Open water extent map derived from Sentinel-1 using SAT. Blue pixels indicated identified surface water and the beige pixels represented the lands. (b) Open water extent map derived from Sentinel-1 using Otsu Thresholding. Blue pixels indicated identified surface water and the beige pixels represented the lands.

The surface water map generated from Sentinel-1 data with proposed SAT (Figure 4.7a) is consistent with the manually digitized polygons over large water bodies. Similar to the Radarsat-2 result (Figure 4.6a), the majority of surface water bodies are successfully identified and extracted with k = 0.9797, while part of the water streams is missing in the classification results as omission errors. On the other hand, the water/land class derived from the same Sentinel-1 data with

Otsu thresholding is illustrated in Figure 4.7b., and the surface water extent was not successfully extracted with k = -0.7181. Although all water bodies are identified, the majority of the land is falsely classified as water.

4.3.2 Accuracy Assessment

One scene of high-resolution SPOT multispectral image was chosen to be within the closest date with the Radarsat-2 data for comparison and accuracy assessment. Figure 4.8a shows the water bodies derived from SPOT NDWI image using Otsu thresholding and illustrates that large size open water bodies, such as the lakes, have been successfully delineated with $k = 0.9586$. Also, the linear streams which connect the lakes have been differentiated from the land. However, the built-up land features (top left) are falsely identified as surface water objects. The built-up land features have the same positive values as water features in the NDWI image. This is due to the fact that the index is able to efficiently suppress vegetation and soil to negative values, but fails to separate the built-up land background from the positive value range.

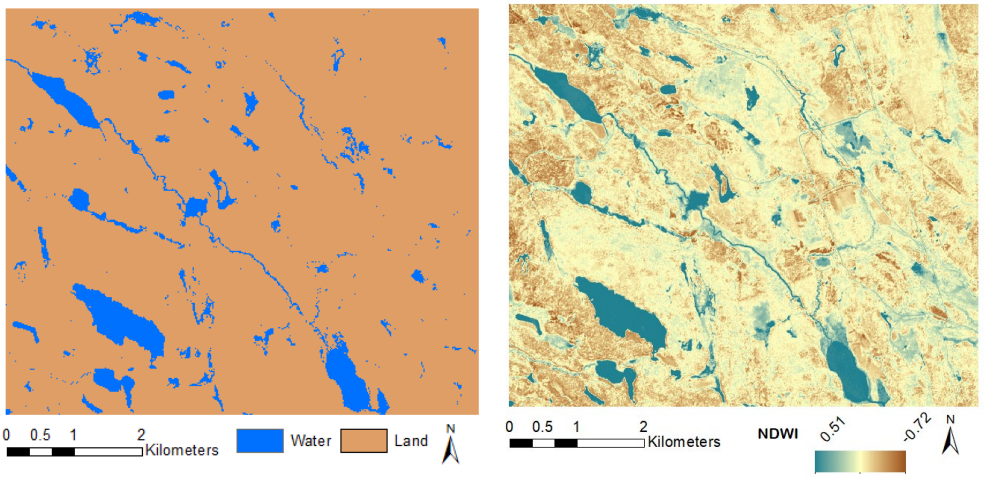

(a) (b)

Figure 4.8. (a) Open water extent map derived from NDWI Thresholding. Blue polygons indicate identified surface water and the purple background represented land. (b) NDWI result generated from SPOT 7 imagery, where blue to red indicate water index from high to low.

To quantitatively evaluate the classification result, manually digitized shapefile was used to validate the accuracy of classifications and the results are shown in Table 1. As illustrated in Table 1, the overall accuracy for both Radarsat-2 and Sentinel-1 SAR data exceeds over 95%, and SAR water class has higher total accuracy than the one generated from the NDWI image. The water classification of Sentinel-1 data using Otsu's method has a total accuracy of 60.34%.

Table 4.1 The matrix of classification accuracy

	False Negative (%)	**False Positive(%)**	**Total Accuracy (%)**
Radarsat-2 (SAT)	1.15	0.22	98.62
Sentinel-1 (SAT)	1.27	0.29	99.70
Sentinel-1 (Otsu)	0.29	39.35	60.34
NDWI (Otsu)	3.09	0.17	96.73

For the accuracy of SAR derived water class, the false identification rate is higher than that derived from NDWI image, indicating more land features may have been falsely identified as water (i.e. commission errors were high).

4.3.3 Time-series Analysis

The time-series extent of surface water was extracted using the Radarsat-2 data from May 2008 to August 2016 shows the dynamics of surface water. As shown in Figure 4.9, the surface water extent generally varies in relation to monthly accumulated precipitation as measured at the local weather station. Decreases in precipitation were associated with a lower area of surface water for several of the observed months (August 2008, May 2014, August 2014, and June 2015). The area of water bodies follows the rate of 3-Day accumulated

precipitation reasonably well. In general, the area of water bodies increases after an increase of 3-Day accumulated precipitation and the change in surface water agrees with the change in precipitation. The area of water bodies follows the rate of 3-Day accumulated precipitation reasonably well. In general, the area of water bodies increases after an increase of 3-Day accumulated precipitation and the change in surface water agrees with the change in precipitation.

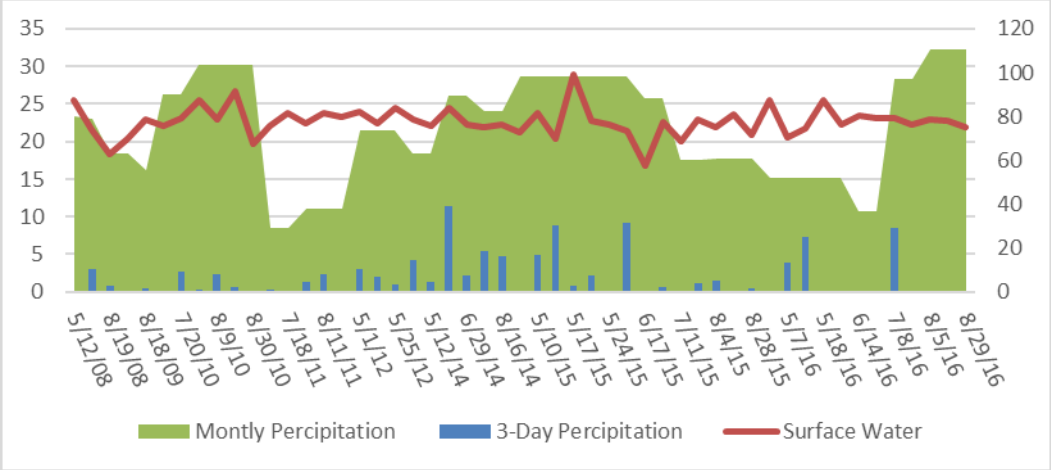

Figure 4.9. Time series of Radarsat-2 derived area of surface water extent (km squared), 3-Day precipitation (mm) and monthly precipitation (mm). The area of water was calculated from the time series of classification maps. The 3-Day and monthly accumulated precipitation data were collected by a nearby weather station in Algonquin Park East, Ontario.

4.4. Discussion

For the entire Radarsat-2 dataset (51 scenes), with the average imagery size of 2700 pixels by 3800 pixels, the proposed method computes the series of water maps in 559.26 seconds on a computer equipped with Intel® i7-6700 3.4GHz and 16GB RAM. Among the whole processing time, SAT thresholding takes 248.92 seconds, post-processing takes 12.95 seconds, and writing the image file takes 297.39 seconds.

The proposed SAT thresholding method is able to successfully extract the majority of surface water bodies. This can also be observed from the histogram (Figure 4.10), as the proposed method detect the threshold close to the bottom of the valley (indicated by the blue line), while the Otsu's method locates the threshold near the peak (indicated by the red line). It can be observed that the surface water bodies with the flooded areas only cover a minor portion in the study area, producing a different histogram from the water dominated studies as shown in Martinis et al. 2009 (Martinis et al., 2009), and the Otsu method failed to properly classify the surface water from the SAR data within our study area.

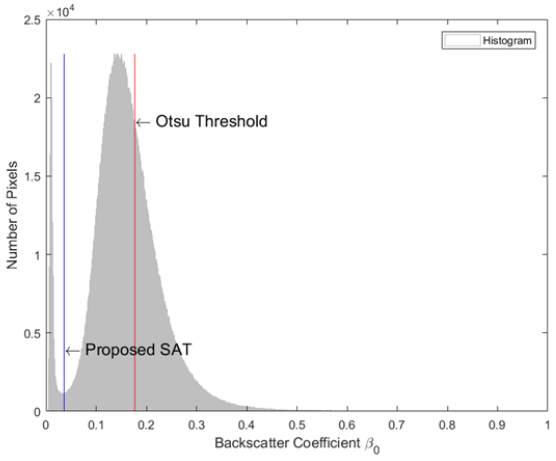

Figure 4.10. Histogram of Sentinel-1 image with threshold solved by proposed SAT method marked by a blue line, and Otsu threshold value marked by a red line.

It is worth mentioning that Otsu thresholding is more effective to separate water and non-water classes when the histogram exhibited as a bi-modal histogram, i.e. two distinct objects presented as one maximum for water and one maximum for land. This can be observed in the NDWI image, and Otsu method is able to separate the two classes with an accuracy of 96%. On the other hand, the histogram of boxcar filtered SAR data only has single modal presented, as shown in Figure 4.10, using Otsu yield low classification accuracy, around 40%. To better align with the literature, the de-speckle filter employed in Otsu thresholding for SAR data is Lee filter, instead of the boxcar filter used by the proposed method, and the classification accuracy raised to a reasonable 60%.

A variety of factors might complicate the derivation of water surfaces from SAR data. The low backscattering from some bare agriculture fields and radar shadows led to the overestimation of the water extent. Besides, some inundated water resulted from heavy precipitation appeared in the SAR data, but not accounted as water bodies in the reference data. For the water surface derived from the NDWI image, the higher commission errors than the omission errors are possibly due to flooded vegetation being classified as water. For the water surface derived from the SAR data, omission errors were observed from smooth objects like pavements and bare soil. Future studies can include additional road masks to reduce the overestimations introduced by roads in urban areas. Omission errors were observed from flooded vegetation close to rivers and lakes (left side of Figure 4.5(b)). This finding is consistent with previous studies that have found fully Polarimetric data were preferred for detecting flooded vegetation (B. Brisco, Schmitt, Murnaghan, Kaya, & Roth, 2013; Morandeira et al., 2016). Furthermore, the Radarsat-2 detected inundated water areas unidentified in the provincial inventory are typically smaller water bodies. Those areas can be a potential breeding area for water birds.

Notably, part of the commission errors may also result from the difference in acquisition time between the spectral image and the SAR image. The reference

manual digitized shapefile was generated from interpretation from the recent spectral image, and the actual boundary observed from SAR data did not precisely follow the same edges from the spectral image. Also, the influence of roughening of the water due to wind on the radar backscatter results in diminished water/land contrast, which can affect the classification accuracy. Future study will cooperate with multi-temporal filters (Quegan, Toan, Yu, Ribbes, & Floury, 2000) and non-local speckle filters (Deledalle, Denis, Tupin, Reigber, & Jager, 2015) to potentially reduce the speckle-noise while the time-sensitive edges are adapted.

4.5 Summary

In this study, a robust thresholding technique was proposed to classify SAR data with a promising accuracy. The pre-processing of SAR data and classification was implemented under the PCI Geomatica and the SNAP toolbox and Python packages. The findings demonstrated that using an SAT technique could automatically generate accurate surface water maps from C-band SAR data (Radarsat-2 and Sentinel-1) in an efficient and timely manner. Based on the accuracy assessment, 98% of the water bodies were successfully extracted. The

visual validation showed that the surface water extent closely followed the boundaries of the main water bodies, such as lakes and rivers. Omission errors were observed for small and linear targets, such as streams and rivers, and commission errors were mainly from roads and inundated vegetation. Another valuable finding was that the time-series results revealed the seasonal dynamics of inundation and showed a correlation between the response in the surface water extent to the changes in precipitation. This implied that the usage of SAR data might allow for detailed and timely surface water mapping for wetland habitat monitoring. Notably, other SAR data, such as Radarsat 1, can also be utilized to extract surface water bodies. However, even though rivers and big lakes can be identified from it, the ponds could be missed due to the coarse spatial resolution.

Chapter 5

Beaver pond identification from multi-temporal and multi- sourced remote sensing data through an AHP model

In this Chapter, remote sensing based indicators testing for habitat assessment is provided. Effective habitat management for waterfowl requires tools to better characterize the distribution, quantity, and/or quality of wetland habitat in remote areas of a species' range, and to enable monitoring of the outcomes of habitat conservation actions and associated responses of wildlife. The waterfowls are known to use beaver-modified wetlands, especially during breeding when energetic demands during egg production and brood-rearing are high, due to the tendency of these habitats to have high invertebrate food resources (Diefenbach & Owen Jr, 1989; Merendino & Ankney, 1994). Multi-source remotely sensed information and a fuzzy Analytical Hierarchy Process were used to map the spatial distribution of beaver-modified wetland features.

The use of multi-source data, including a Digital Elevation Model, a Sentinel-2 Multi-Spectral Image, and RadarSat 2 Polarimetric data, enabled us to identify individual beaver ponds successfully. Validation was performed using an independent dataset of known beaver sign observations. An average of 83.0% of the beaver dams were located in the area predicted to be the most active. Over 72.5% of the beaver ponds in our independent validation dataset were successfully identified.

The manuscript based on this work has been submitted to Journal of Geo-Spatial Information Science and it is under the second round of review.

5.1 Related work

To date, the mapping of beaver ponds mostly occurs through manual interpretation of aerial imagery (e.g., visual identification of pond morphology, the presence of beaver dams, riparian vegetation, etc.) which can be time-consuming and limited by the availability of imagery across large areas of northern Canada, especially in the boreal forest regions (Allen, 1982; Meentemeyer & Butler, 1995; Suzuki & McComb, 1998). The effectiveness of this also greatly depends on the available time series of aerial photos, and currently, it does not readily enable the tracking of changes through time in beaver pond dynamics. The rapid advancements in the availability of remote sensing data enable the mapping of a range of environmental features relevant to beaver habitat identification, including stream gradient, stream power, stream depth and width, valley width, and canopy height. Inclusion of such features may improve the accuracy of predictive models for identifying beaver ponds on the landscape. While most historical beaver habitat studies (Anderson & Bonner, 2014; Dittbrenner et al., 2018; Herrera Huertas, Lencinas, Toro Manríquez, Miller, & Martínez Pastur, 2020; Pollock, Pess, Beechie, & Montgomery, 2004) have focused on locating areas on the landscape that are best suited for beavers to build their dam, with the models relying on hydrology features such as the

stream gradient and elevation, vegetation (or habitat) related features, such as forests and the presence of wetlands, also affect beaver presence and distribution and have been under-utilized to date (Cunningham, Calhoun, & Glanz, 2007).

Multi-source and multi-temporal remote sensing data, such as optical imagery and Synthetic Aperture Radar (SAR), can be used to map habitat related wetland features (Amani et al., 2017; Banks et al., 2015; Bourgeau-Chavez et al., 2015; Corcoran, Knight, & Gallant, 2013). SAR data are particularly useful for mapping water and wetlands as they are unaffected by weather patterns (e.g., cloud cover) due to the use of microwave radiation which allows a double-bounce scatter; a double-bounce scattering between surface water and vegetation can improve the identification of wetland areas, as the microwave radiation strikes the horizontal saturated soil/water surface first, then the vertically oriented vegetation (or vice versa), before being returned to the sensor (Freeman & Durden, 1998). Combining multi-temporal optical imagery and SAR data can further improve the accurate classification of wetland features, as time series optical data can be used to map deciduous forests and meadow marshes efficiently with the changes between leaf-on (i.e., summer) and leaf-off (i.e., fall-winter-spring) conditions. To develop a predictive beaver habitat model, beaver activities also need to be identified from a suite of predetermined remote sensed

features. In this study, I used the Analytical Hierarchy Process (AHP) (Saaty, 2004) to identify and assign weights to these predetermined features. Rather than assign the weights arbitrarily, AHP prioritizes the features based on their importance and mathematically calculates the weights and scores for each feature. Several studies have utilized the AHP in other wildlife habitat mappings to produce predictive habitat models for species such as Tiger, Mentilin and Rhino (Imam & Tesfamichael, 2013; Isnaini, Marhaento, & Subrata, 2021; Medhi & Saha, 2014).

The objective of our study was to identify beaver ponds from multi-source remote sensing data through an advanced fuzzy AHP model and test the accuracy of that model. To accomplish this, we used three data sources to provide habitat related features for our model, a LiDAR-derived digital elevation model (DEM), Sentinel 2 multispectral imagery (S2 MSI), and RadarSat 2 (RS 2) Polarimetric SAR data, from which the S2 MSI and RS 2 are multi-temporal. The environmental/habitat features were derived from previous studies to describe wetland and vegetation features used by beavers; AHP was then used to assign weights to those features. The beaver ponds were identified from the pool of all wetland features from the 'high-activity' area. Provincial beaver dam locations and manually digitized beaver ponds were used to validate the results. Thereafter,

mapping the long-term patterns in habitats in relation to their potential effect on waterfowl demographic rates is discussed.

5.2. Study Site and Materials

Our study area is located in central Ontario (77° 28’ 21” W, 45° 59’ 10” N), Canada (Figure 5.1), within the western portion of the black duck breeding range in Canada. A deciduous forest dominates the southern portion of the area, transitioning into a northern boreal forest. There is limited agricultural development, but forest harvesting on Crown Land has occurred throughout the area. For this study, I used waterfowl breeding pair data from the Eastern Waterfowl Survey (EWS) conducted by Environment and Climate Change Canada given its focus on detecting breeding black ducks and time series. Two of the 40 plots (Plots 7 and 11) were chosen based on the computational limitations of the study, availability of existing SAR, beaver observations and waterfowl data. These plots also permitted the use of detailed habitat information from remote sensing and other products that were not available for the other EWS plots. Each plot is 5 km by 5 km and all wetlands and waterbodies are surveyed by a four-person crew from a helicopter during peak nest initiation of black ducks.

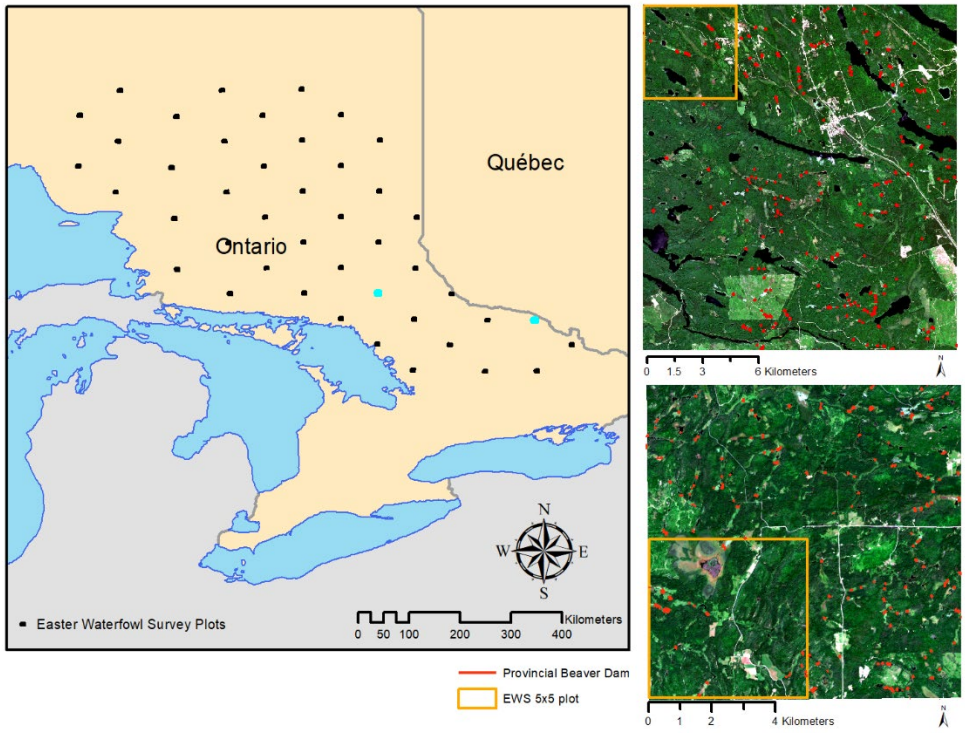

Figure 5.1. Map of the study site. The black squares are all of the Eastern Waterfowl Survey (EWS) Plots with study Plots 7 and 11 highlighted. The upper right panel shows test area 1 (Plot 7) with the S2 MSI in true color, while the lower right panel shows test area 2 (Plot 11) with the S2 MSI in true color. The red lines in the two panels are the known locations of beaver dams provided by the Ontario Ministry of Northern Development, Mines, Natural Resources and Forestry.

The following three remote sensing data sources were used in our study to map the beaver ponds, DEM, S2 MSI, and RS 2 Polarimetric SAR data. S2 is a wide-swath, high-resolution, multispectral imaging mission with a global five-day

revisit frequency. The S2 MSI samples 13 spectral bands: visible and NIR at 10 meters; red edge and SWIR at 20 meters; and atmospheric bands at 60 meters of spatial resolution. Google Earth Engine was used to query and download the level 2A (the bottom-of-atmosphere reflectance in cartographic geometry) multi-temporal S2 MSI. Two scenes of S2 MSI from spring (May 13, 2020) and summer (Aug. 14, 2020) with cloud coverage of less than 10% were selected for extracting seasonal changes.

A set of C-band (5.405 GHz) RS2 single look complex (SLC) images were acquired for the summer periods. The images were acquired from Fine Quad (FQ) polarized mode with a resolution of 5.2 m and 7.7 m in slant range and azimuth, respectively. Also, images were collected in both descending (acquisition time around 11:30 UTC) and ascending (acquisition time around 23:15 UTC) orbits, with beam mode of FQ7 (Incident Angle range from 25.7° to 27.6°) and FQ9 (Incident Angle range from 28° to 29.8°).

A DEM was used to perform the terrain correction and proper alignment of all SAR data and images. The DEM used for this purpose was the South Central Ontario Ortho-photography Project (SCOOP) grid (2 m) generated from the stereo imagery collected between April to May 2013.

Known beaver dam locations and manually digitized beaver ponds were used to assess the accuracy of the remote sensing-based habitat classification of beaver ponds. The known beaver dam location dataset was provided by the Ontario Ministry of Northern Development, Mines, Natural Resources and Forestry. A beaver dam is a linear feature, which can be identified on aerial imagery, and is constructed of sticks, mud, and stones by beavers to create a beaver pond and indicates the presence of beavers in an area. Known beaver ponds were manually classified and digitized as polygons using 2018 aerial orthophotography imagery and the National Hydrological Network (NHN) data. The imagery permitted visual identification of beaver signs (dams, lodges) and the beaver ponds were classified using the riverine-beaver pond marsh class as defined in boreal wetlands classification for waterfowl (Rempel, Abraham, Gadawski, & Gabor, 1997).

5.3. Methodology

I used existing knowledge of the habitat needs and life history of beavers to identify relevant environmental characteristics and mathematically weight those features based on their relative importance to beavers. This was undertaken to map 'probable' beaver activity and improve the identification of beaver ponds in our predictive model from other open waterbodies. The process consisted of

three steps: 1) extraction of open water from RS 2 data; 2) mapping of 'probable' beaver activity areas; and 3) beaver pond identification through rule-based classification of open water. 'Probable' beaver activity areas were inferred by mapping the environmental and habitat features assumed to affect their presence, including dam and shelter habitat features, such as DEM slope, stream gradient, stream order, open surface water, wetland presence, humans, and non-coniferous vegetation food sources. Fuzzy AHP was used to mathematically assign the weight of each feature and then develop a beaver activity map. To accommodate the differences in spatial resolution in the input data, all of the derived environmental features were standardized by resampling to a resolution of 10 meters.

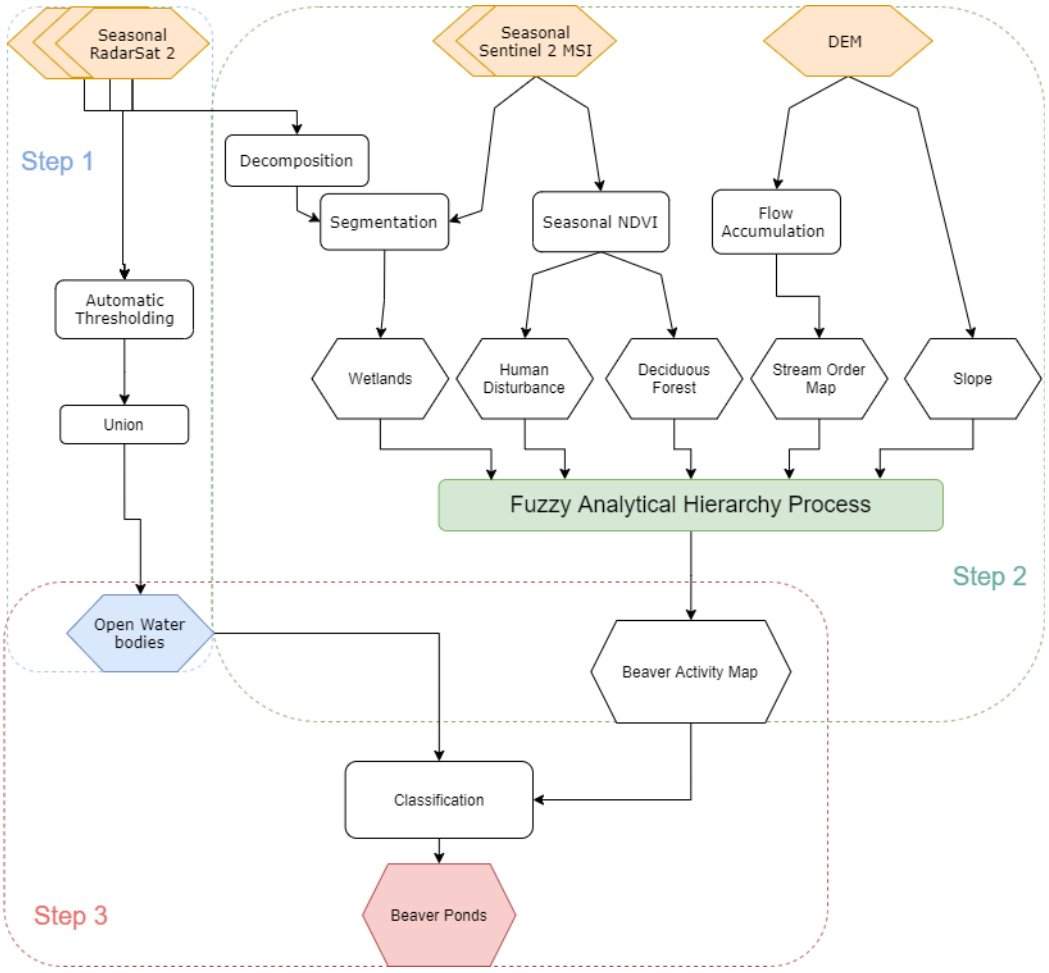

Figure 5.2. Flowchart depicting the use of remote sensed imagery data with a Fuzzy Analytical Hierarchy Process to assign weights and known beaver activity to map the location of beaver ponds.

5.3.1 Open surface water extraction from RS 2 data (Step 1)

Open water was extracted with an improved version of the step-wise automatic thresholding method presented in Zhang et al. (2020). The seasonal RS2 data of three scenes from aerial photographs taken between early May to late August were used because seasonal data better represents meadow marsh compared to using a single scene. The size and shape of beaver ponds can vary within seasons, which can affect the accuracy of the extraction when using a single scene. Moreover, seasonal data can better differentiate periods of drought, as it is easier to detect future droughts during spring when wetlands are being recharged compared to summer when precipitation is less. To accurately identify the candidate open waterbodies, the step-wise thresholding method was performed on each scene, followed by the geometric union to extract the open water.

The step-wise thresholding method is described as follows.

First, one scene of RS2 data was pre-processed to generate a backscattering coefficient. The HH polarization was used in this study as it provided the highest contrast between calming open water and land. Relief displacement was corrected through geo-referencing with a provincial 2-meter DEM.

Second, a boxcar filter with a 5-pixel by 5-pixel window was adopted, resulting in a unique valley-hill pattern in the histogram that represented a better distinction between water and non-waterbodies. The strategy of detecting the bottom of this valley has been proven to be a good threshold that separates water bodies and non-water bodies (L. White et al., 2015). It is worth mentioning that other filters, such as Lee and adaptive Lee, were tried as well. However, only the boxcar filter provided a unique valley-hill pattern in the histogram.

Third, a step-wise method was then developed to determine the threshold as the valley value of the histogram, which was then used to generate the water extent map. Last, post-processing with morphological operations was applied to remove an island within a lake and small misclassified areas. Further details of the automatic step-wise thresholding method for open water map generation can be found in Zhang et al. (2020). After the operation, all the surface water features were converted into polygons. All the pre-processing procedures were done with a Python script (Python Software Foundation, https://www.python.org/) utilizing the functions provided by Geomatica Banff (PCI Geomatics Inc, Canada)

5.3.2 Mapping ‘probable’ beaver activity areas (Step 2)

Knowledge of beaver life history and habitat use from previous studies were used to identify a suite of environmental and habitat features and map ‘probable’ areas of beaver activity within our study area, akin to habitat suitability (Table 1). Three groups of environmental features, based on habitat needs, were derived using remote sensing techniques to generate the ‘probable’ beaver activity map.

Table 5.1. Environmental and habitat features required during the life history of beavers. Features were linked to remote sensing imagery data to create a ‘probable’ beaver activity map.

	Dam and Shelter Environmental Features		Food Source Environmental Features	Additional Shelter Environmental Features	
Beaver Habitat Needs and Preferences	Flat surface to form a pond	Build dams near slow streams	Alder, aspen, birch, cottonwood, maple, poplar, and willow trees (Allen, 1982)	Use wetlands as shelters	Avoid high-traffic areas/presence of humans
Remote Sensing Derivate	DEM slope	Stream maps from flow accumulation	NDVI for non-conifer treed area	Image classification for wetlands	NDVI for human disturbance and infrastructure

Dam and Shelter Environmental Features

Topographic information associated with slope and streamflow can be significant predictors of beaver presence, as beavers prefer relatively slow streamflow for building their dams (Woo & Waddington, 1990). In this step, the ArcGIS hydrology toolbox was used to derive the slope and stream network. A 2-meter DEM was used to calculate the slope gradient from each cell of the DEM. The stream network was delineated by first determining the direction of water flow from each cell, as well as sinks in the original DEM. A sink is usually an incorrect value that is lower than the values of its surroundings. To ensure proper drainage mapping, any depressions that were created from this step were filled. This process prevented the problem of water flowing into the area not being able to flow out. Second, flow accumulation was generated by calculating the number of upslope cells flowing to a location. Shreve techniques(Tarboton, Bras, & Rodriguez-Iturbe, 1991) were then used to define the stream order of each segment in the network.

Environmental Features Related to Food Sources

I used non-coniferous vegetation cover as an indicator to map the availability of food (i.e., woody food items) used by beavers on the landscape. To separate the non-coniferous vegetation from the conifers, the difference in the NDVI

calculated from imagery collected between leaf-on (summer) and leaf-off (spring) conditions were used. Specifically, $NDVI_{spring}$ and $NDVI_{summar}$ were calculated from two scenes of S2 MSI within Google Earth Engine, and the difference between these two NDVIs was generated. For a given pixel, if the difference was greater than 0.5, it was classified as a non-coniferous vegetation. The threshold of 0.5 in the NDVI difference between the spring and summer scenes was used to define non-coniferous vegetation. The 0.5 threshold value of 0.5 was selected as it best described the difference in NDVI between the leaf-on and leaf-off conditions of a forest (Yang, Yang, Heskel, Sun, & Tang, 2017).

Additional Shelter Environmental Features

The combination of seasonal S2 MSI and RS 2 was used to define wetland cover. Specifically, the RS 2 data were first processed with a boxcar de-speckle filter and relief displacement correction from the 2-meter DEM. Then, the Freeman-Durden polarimetric decomposition was calculated. Different surface objects have different scattering mechanisms, and thus may exhibit differences in the resulting images when SAR data are decomposed to different scattering components. The flooded vegetation, open water bodies, upland vegetation, and wet unsaturated soil are usually dominated by double-bounce backscatter, specular backscattering, volume backscattering, and surface scattering,

respectively (Freeman & Durden, 1998). To locate wetlands, the double bouncing from Freeman-Durden decomposition was used.

Due to the speckled nature of the SAR data, classification with SAR data only might produce fragmented results and low accuracy. To utilize both spectral and structural information of wetlands, we combined SAR and S2 MSI to extract wetlands. The region growing segmentation method was employed to generate the wetland objects with the surface reflectance from S2 MSI and the double bouncing component from the decomposed RS2 served as inputs. The segmentation parameters were determined through trial and error. After the segments were created, the double-bouncing component was then used to extract the wetland features (Freeman & Durden, 1998). Specifically, segments with the double bouncing component over a threshold were labeled as wetlands. The threshold was determined based on the natural break shown in the histogram.

The human interference/presence layer was generated using NDVI values. Since human interferences have high ground reflectance and remain unchanged between seasons, a threshold value was set to satisfy both 0.1 in NDVI difference and 0.1*MaxDN of the red band in summer scene conditions to derive the layer.

A fuzzy logic AHP was used to produce the beaver habitat suitability map by

integrating information from the suite of environmental layers. To incorporate features derived from different sources, normalization was applied to quantify the influence of the weightings at an equivalent scale. The fuzzy logic inference was used as it depends on the margin transition of an attribute and emerges less arbitrarily. It is also more useful than an ordinal rating. The Euclidean distances were calculated for each feature, and the fuzzy logic inference was implemented to normalize all the environmental features to a common scale between 0 and 1, with 0 denoting least suitable and 1 denoting most suitable.

A series of values of distance and terrain flatness was adopted from an Alberta beaver study, which modelled the beaver occupancy related to the influence of stream hydrology, forest composition, and industrial activity (Stevens, Paszkowski, & Foote, 2007). Specifically, a distance function was created on the stream layer, extending to 200 meters beyond the edges of the selected stream water. The distance function layer was reclassified based on literature values for the distances that beavers travel from a waterbody for foraging. Areas of water cover and land within 50 meters were given the highest scores, as those are areas of highest beaver activity (Jenkins, 1980). More distant areas received lower scores, as activity decreases dramatically but can extend to approximately 200 meters. The streams were rescaled as shown in Equation 5.1. Beavers prefer a

flat area to form a wetland for shelter, so a change of slope of less than 5 degrees was considered acceptable, whereas slopes greater than 5 degrees were not considered as suitable beaver habitat. The layer was rescaled based on Equation 5.2.

$$Stream_f = \begin{cases} \frac{200 - D_{Stream}}{200 + 50(Order - 1)}, & if \ D_{Stream} \leq 200 \ meters \\ 0, & if \ D_{Stream} > 200 \ meters \end{cases}$$

(Eq. 5.1)

$$Slope_f = \begin{cases} \frac{5 - Slope}{5}, & if \ Slope \leq 5 \ degrees \\ 0, & if \ Slope > 5 \ degrees \end{cases}$$

(Eq. 5.2)

The criteria based on the distance to the food was determined from the non-coniferous vegetation layer, as shown in Equation 5.3. It is worth mentioning that in an ideal case, the ranking should be based on forest dominant woody species. However, the cover types of the preferred forage tree species (e.g., alder, poplar, etc.) were not available, so the extracted non-coniferous vegetation cover with a buffer distance extending to 50 meters was assumed to represent suitable beaver habitat in terms of potential food availability.

$$Deciduous\ \ Trees_f = \begin{cases} \frac{50 - D_{Dtrees}}{50}, & if\ \ D_{Dtrees} \leq 50\ \ meters \\ 0, & if\ \ D_{Dtrees}\ \ > 50\ \ meters \end{cases}$$

(Eq. 5.3)

For shelter consideration, the distance to the wetland and human interferences were calculated and rescaled. A 40-meter distance to the wetland was assumed to affect habitat suitability, and Euclidean distance to all wetland classes was calculated and rescaled based on Equation 5.4. Distances less than 200 meters to human infrastructures were deemed unsuitable given the lack of preferred habitat or physical disturbance, as shown in Equation 5.5.

$$Wetland_f = \begin{cases} \frac{40 - D_{Wetland}}{40}, & if\ \ D_{Wetland} \leq 40\ \ meters \\ 0, & if\ \ D_{Wetland}\ \ > 40\ \ meters \end{cases}$$

(Eq. 5.4)

$$Human\ \ Interference_f = \begin{cases} \frac{D_{HI} - 200}{D_{HI}}, & if\ \ D_{HI} \geq 200\ \ meters \\ 0, & if\ \ D_{HI}\ \ < 200\ \ meters \end{cases}$$

(Eq. 5.5)

AHP was used to assign weightings to features between the derived fuzzy layers. As a general AHP, three steps were utilized to generate the weights. First, a consistency matrix was calculated based on the pairwise importance among all of the environmental/habitat features. The pairwise importance was evaluated

and assigned based on previous knowledge of the habitat needs and behaviour of beavers. In this study, a range of 1–5 was used to indicate importance (or weight), where a value of 1 denoted equal importance and 5 denoted extreme importance. For better representation, the matrix arranged the most important feature (i.e., highest rank) on the first row, followed by the less important features with the lowest important feature at the bottom of the matrix. In the matrix, the feature would have equal importance with itself (i.e., rank equals 1), and the reverse order of pairwise comparison was assigned to the inverse ranking. Second, the pairwise comparison scores were normalized by the respective column sum. The final weightings were determined by averaging the respective row of the normalized matrix.

The consistency of the assigned pairwise importance was checked by calculating a consistency index (CI, shown in Equation 5.6), where λ is the largest eigenvalue computed from the consistency matrix and n is the number of features. The large value of CI denotes higher inconsistency, while a value of 0 denotes complete consistency. In general, a CI value within 10% of perfect consistency was considered satisfactory (Wu & Xu, 2012).

$$CI = \frac{\lambda - n}{n - 1} \qquad \text{(Eq. 5.6)}$$

5.3.3 Beaver pond identification (Step 3)

I used a size filter to help extract the beaver ponds from remote sensed imagery. Based on the literature, beaver pond size can range from 702 m^2 to 16,357 m^2 (Beedle, 1991; Karran, Westbrook, Wheaton, Johnston, & Bedard-Haughn, 2017). After all of the candidate ponds were extracted, a distance filter was also set to screen out the ponds that were far from the "high beaver activity" area. The candidate ponds that fell within the range were extracted and labeled as 'potential' beaver ponds.

5.3.4 Validation of Potential Beaver Ponds

To validate the 'potential' beaver ponds identified by our methods, both qualitative and quantitative analyses were conducted. The independent manually digitized beaver ponds were identified as wetlands based on the presence of impoundments created by beaver dams evident in the imagery. In addition, data identifying the presence of beavers from a helicopter survey were used as a visual reference for results validation.

Further validation of our modeled beaver ponds results was also completed from beaver presence data from Plot 11. Two seasonal S1 MSI was acquired on May

1, 2020, and August. 12, 2020, together with two RS2 data from August 08, 2014, and August 12, 2014, were used for this assessment.

5.4. Results

5.4.1 Open surface water extraction from RS2 data

The results from the open surface waterbody extraction from seasonal RS2 data are shown in the blue-lined polygons in Figure 5.3. The majority of the surface waterbodies were successfully identified and extracted, with an overall accuracy of 97.2%. However, a few linear water streams and small ponds are missing in the classification results as omission errors, and a few commission errors are evident near the bottom of the site, mainly due to inundated water or flooded vegetation falsely identified as open surface water (Figure 5.3).

Figure 5.3. Open water bodies extracted from the seasonal RS2 data are shown in blue-lined polygons and overlaid on the S1 MSI summer scene, with the red band display in red, the green band display in green, and the blue band display in blue.

5.4.2 Beaver activity map

The result of the derived stream network (Figure 5.4a) had an order ranking value ranging from 1 (upper stream) to 7 (mainstream), corresponding to changes in elevation. A dense drainage network was produced here to describe the beavers' need for low-speed streams to build their dams. The DEM-derived slope is shown in Figure 5.4(b), where the blue colour indicates a flat area (i.e., changing of slope by less than 5 degrees). Notably, part of the flat area shows a

correlation with water bodies and low-speed upper streams, which makes the slope feature relevant to the location of beaver ponds.

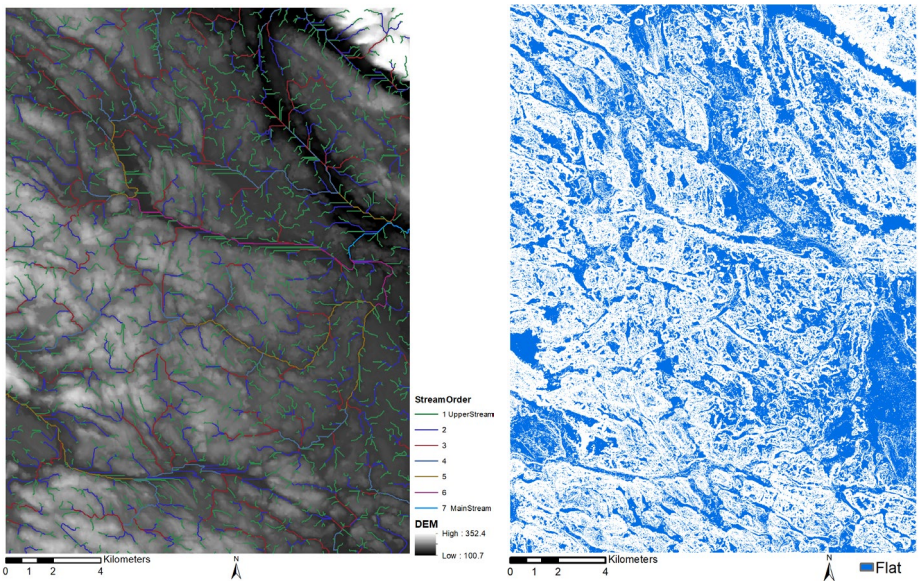

(a) (b)

Figure 5.4. Result of DEM-derived features. (a) Stream ordering map overlaid on grayscale DEM, where the green lines indicate slow-speed upper streams and the light blue lines indicate high-speed mainstreams. (b) The DEM-derived slope in blue indicates a preferred flat area for beavers.

A non-coniferous vegetation area representing beaver food habitat was mapped as the difference in NDVI between the periods of leaf-off (spring season) and leaf-on (summer season) (Figure 5.5). Commission errors were noted, including the wetlands that were falsely identified as vegetation because they exhibited

similar seasonal changes as the non-coniferous vegetation. However, as wetlands are also the preferred location for beavers to build their shelters, these areas were retained for further processing.


Kilometers
0 1 2 4
N

(a)


Kilometers
0 1 2 4
N

(b)

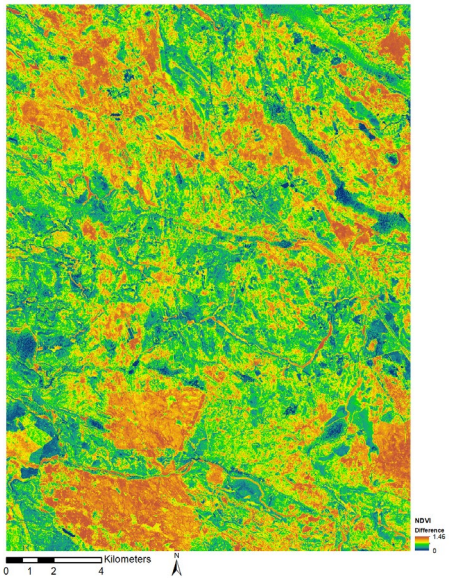
NDVI
Difference
1.46
0
Kilometers
0 1 2 4
N

(c)

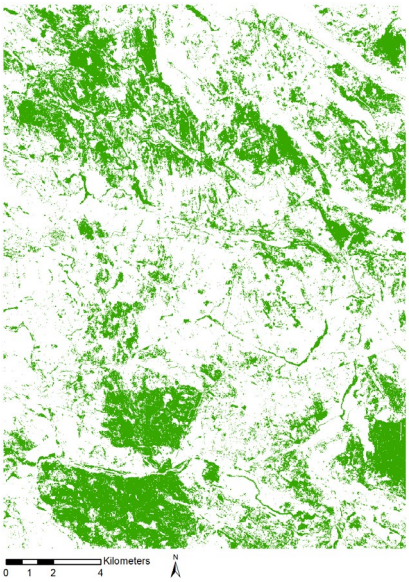
Kilometers
0 1 2 4
N

(d)

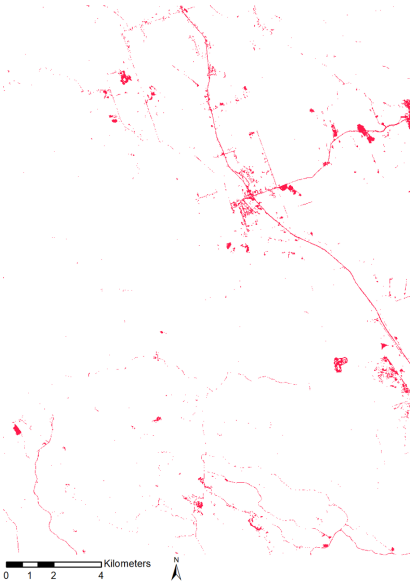

(e)

Figure 5.5. Non-coniferous vegetation layer produced using the Google Earth Engine. (a) A spring scene of S2 MSI taken on May 13, 2020, with the red band display in red, the green band display in green, and the blue band display in blue. (b) A summer scene of S2 MSI taken on Aug. 14, 2020, with the red band display in red, the green band display in green, and the blue band display in blue. (c) The difference of NDVI calculated from the spring and summer images, with the colors varying from red to blue, indicating NDVI difference values ranging from 1.46 to 0. (d) Non-coniferous vegetation area (green area) resulting from the thresholding of NDVI difference. (e) Human interference area (red area) resulting from the thresholding of NDVI difference.

The wetland features derived from RS 2 and S1 (Figure 5.6a) generally manifested good agreement with an available wetland inventory provided by the Ontario Ministry of Northern Development, Mines, Natural Resources and Forestry (Figure 5.6b). Specifically, 84.2% of the wetlands that I identified were also delinated in the provincial data. On the other hand, commission error was 67.1%, as more features were extracted as wetlands from our methodology, especially around the edges of lakes and rivers. This can be explained by the fact that aquatic plants growing near the edge of the open water can create double-bouncing scattering as well. Note that provincial data are ground truthed in the field so they do not eradicate the need for mapping regional scales or greater. Furthermore, provincial data are based on historical records, so they do not reflect the changes in wetlands through time.

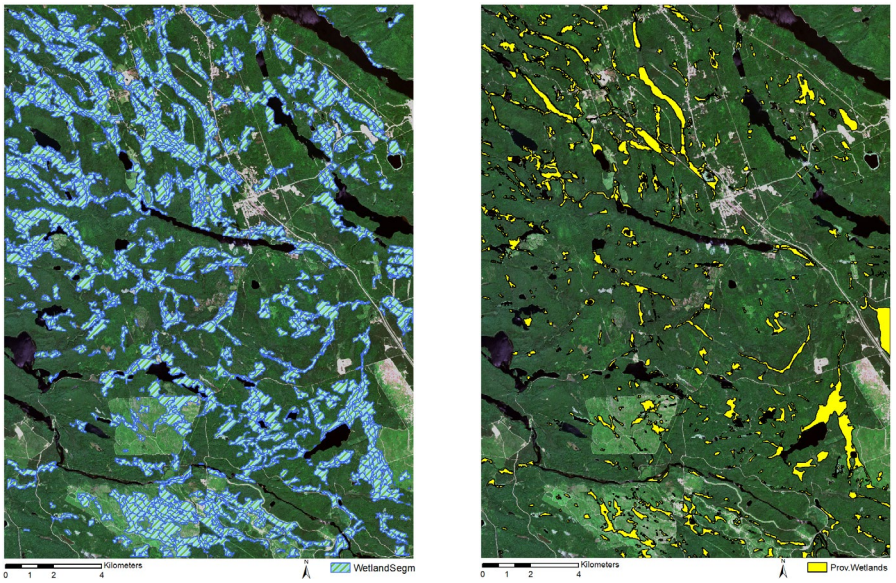

(a) (b)

Figure 5.6. Wetland map. (a) Wetland segments generated from combined S1 MSI and RS2 data are shown in blue hatches and overlaid on the S1 MSI summer scene, with the red band display in red, the green band display in green, and the blue band display in blue. (b) Provincial wetland classes are shown in yellow polygons, overlaid on the S1 summer scene, with the red band display in red, the green band display in green, and the blue band display in blue.

Table 5.2. The AHP calculation process

	Consistency matrix					***Normalized matrix***					*Weights(%)*
	Streams	non-coniferous	Wetland	Slope	H. I.	Streams	non-coniferous	Wetland	Slope	H. I.	
Streams	1	3	3	4	5	0.47	0.45	0.58	0.35	0.31	43.37
non-coniferous	0.33	1	0.5	3	4	0.16	0.15	0.09	0.26	0.25	18.38
Wetland	0.33	2	1	3	3	0.16	0.30	0.19	0.26	0.19	22.06
Slope	0.25	0.33	0.33	1	3	0.12	0.05	0.07	0.09	0.19	10.17
H. I.	0.2	0.33	0.33	0.33	1	0.09	0.05	0.07	0.03	0.06	6.02

Table 2 shows the AHP process with pairwise importance comparisons among the features, normalization of the consistency matric, and the calculated weightings. The calculated weights are listed in the last column of Table 1. The distance to the stream was ranked as the most important feature, followed by non-coniferous vegetation, wetland, slope, and human infrastructure. The CI for the rankings was calculated as 0.0862, which indicates that the pairwise comparisons performed in Table 1 were sufficient for consistency purposes.

The results of the beaver suitability map was overlaid with the reference beaver dam locations from provincial data (Figure 5.7). In the entire test area, 12.6% of the ponds were classified into the most active area. To validate the predictive AHP habitat model beaver activity map, it was compared with the location of the provincial beaver dams, marked as black lines in Figure 5.7. The result shows a good prediction of beaver habitats, as almost all of the dams appeared in the high-ranked area (red to orange colours). Specifically, 78.9% of the beaver dams were in the most active area (i.e., Rank = 9), and all of them fell in areas with ranks greater than or equal to 6. Notably, as the stream network had been given the highest weight in the suitability map generation and the distance to the upper stream was 200 meters, the high-ranked area is linear rather than block-shaped.

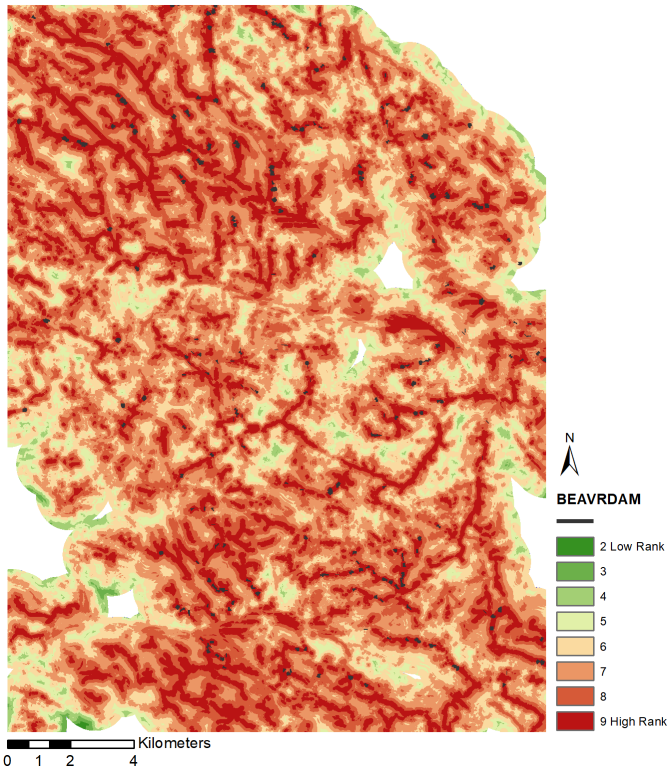

Figure 5.7. Beaver activity map of Plot 7, with the colors red to green indicating high-activity rank to low-activity rank. The provincial beaver dams are represented by black lines.

An additional test of the beaver activity map from Plot 11 was generated using the same criteria, and the result was overlaid with reference beaver dam locations, as shown in Figure 5.8. The colors closer to red indicate a higher rank of beaver activity, and the colors closer to green indicate a lower rank of beaver activity. The result shows a good prediction of beaver habitats, as almost all of the dams

appeared in the high-ranked area (red to orange). Specifically, 86.5% of the beaver dams were in the most active area (i.e., Rank = 9), and all of them fell in areas with ranks greater than or equal to 7.

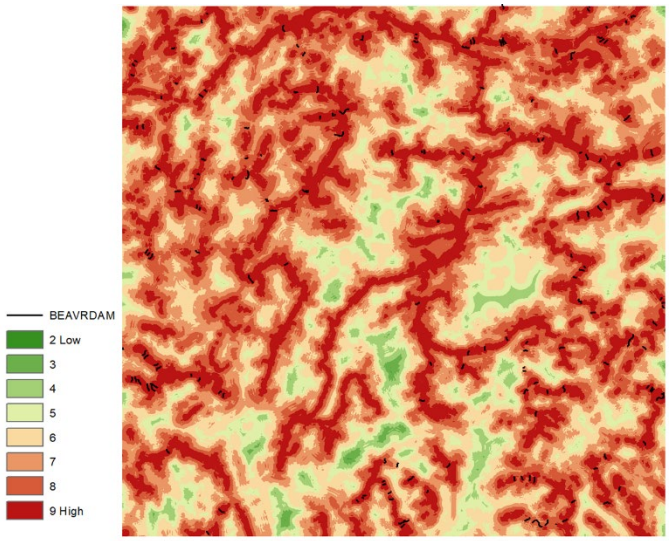

Figure 5.8. Predictive habitat model showing a beaver activity map using an Analytical Hierarchy Process of Study Plot 11, with the colours red to green indicating high-activity rank to low-activity rank. The location of known beaver dams from provincial data are shown by black lines.

5.4.3 Beaver pond identification and validation

With the beaver activity map, open surface waters within the defined size range were extracted and classified as beaver ponds. The result of the identified beaver ponds is shown in Figure 5.9, with 174 objects extracted as 'potential' beaver ponds from the RS2-derived surface water map.

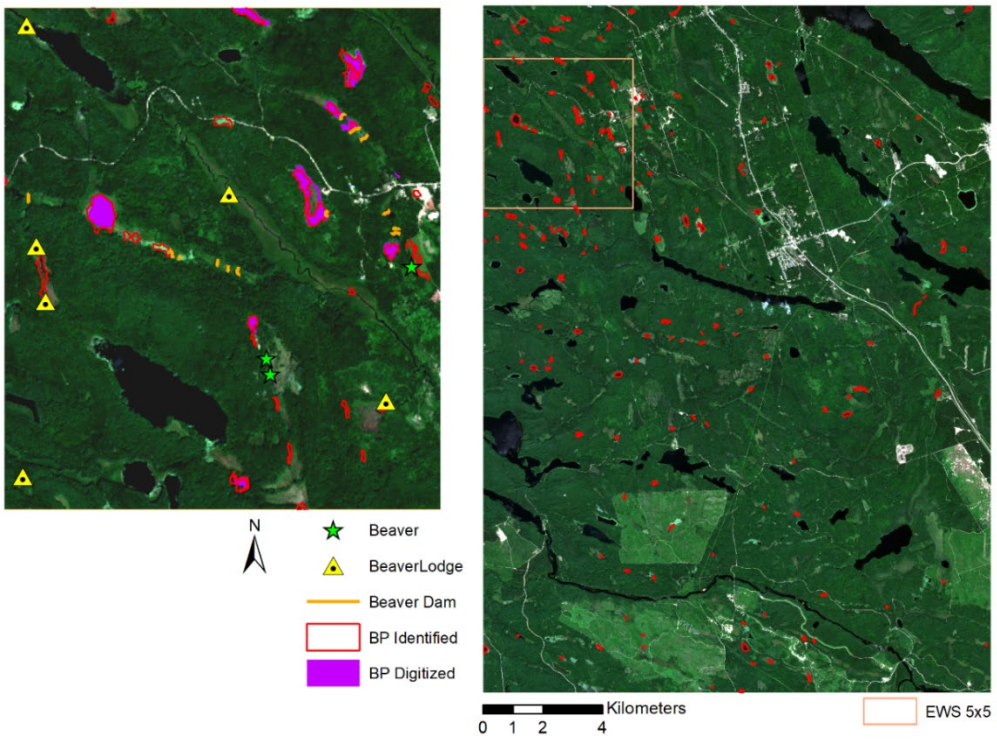

Figure 5.9. The result of the beaver pond prediction in Plot 7 is represented by red polygons. The manually digitized beaver ponds are in magenta polygons, together with the helicopter-observed beaver presence in green stars, the beaver lodge in a yellow triangle, and the provincial beaver dam marked in orange lines. The result is overlaid on a true-color S1 summer scene.

Compared with the reference data, the majority of beaver ponds were successfully identified and extracted, with an overall accuracy of 79.0%. One small pond is missing in the results as an omission error, with a false-positive rate of 9.0%. The false-negative rate is 25.6%, as some commission errors are evident near the bottom and on both sides of the study plot. Notably, the beaver pond identified on the left edge is a true beaver pond, according to the helicopter-observed beaver lodge locations, as they appear on both sides of the pond. Other falsely identified ponds appear to be open waterbodies inside the wetland inaccurately identified as beaver ponds.

The result of the identified beaver ponds in Plot 11 is shown in Figure 5.10, with 121 objects extracted as beaver ponds from the RS 2-derived surface water map. In addition, the corresponding manually digitized beaver pond polygons and the presence of either beavers or lodges are shown in Figure 5.10. Compared with the reference data, the majority of beaver ponds were successfully identified and extracted, with an overall accuracy of 65.9%. The false-negative rate is 21.6%, as commission errors are evident near the bottom and on both sides of the study plot, which appear to be open waterbodies inside the wetland falsely identified as beaver ponds. Although the majority of the predicted beaver ponds appear at the same location as the actual digitized beaver ponds, the false positive rate is

44.5%, as the beaver ponds identified are mostly smaller than the manually digitized beaver ponds. Furthermore, three of the small ponds are missing in the results as omission errors. The reason for the size difference between the predicted and actual ponds is that the size of the beaver ponds was generated from the RS2 data as open waterbodies, considering that the horizontal extent of the same beaver ponds varies seasonally depending on water levels. The acquisition date of the RS2 data is different from the referenced data used in the manual digitizing. The amount of precipitation and extent of beaver activity can further alter the size of a pond overtime.

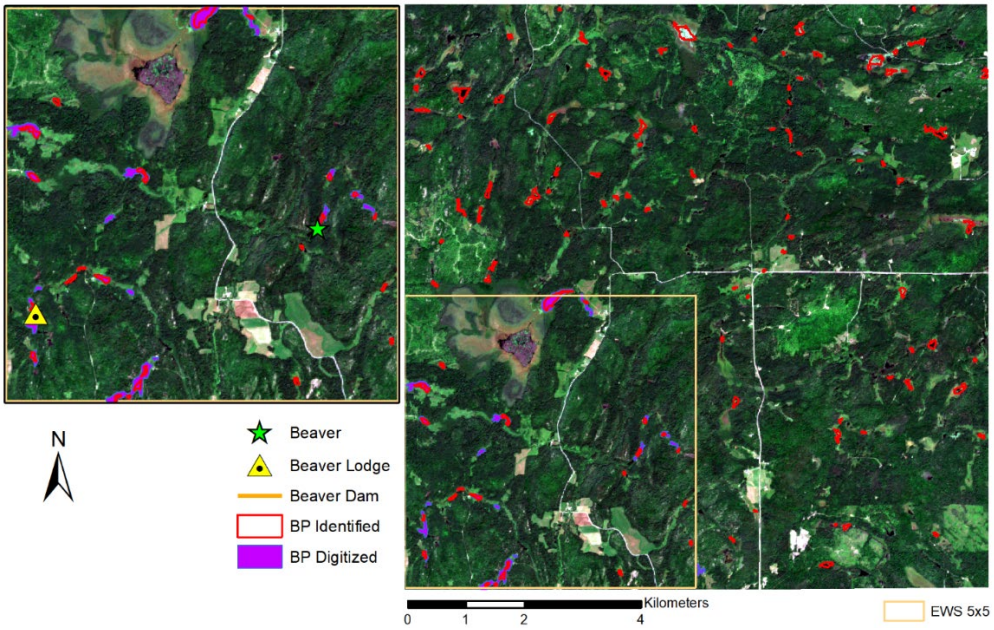

Figure 5.10. The result of the identified beaver ponds in Plot 11 is represented by redlined polygons, with the manually digitized beaver ponds in magenta polygons, the field-identified beaver presence in green stars, the beaver lodge in a yellow triangle, and the provincial beaver dams in orange lines. The result is overlaid on a true-color S1 summer scene, with the red band display in red, the green band display in green, and the blue band display in blue.

5.5. Discussion

This study demonstrates that the integration of multi-sourced remotely sensed information and use of a fuzzy AHP can be highly effective in mapping the spatial distribution and extent of beaver ponds using environmental and habitat features. Our results show a proof of concept in the utility of available

remote sensing products for mapping spatial and temporal variabilities in wetland habitats, particularly in remote areas of Canada. Compared to similar work proposed by Dittbrenner et al. (2018), which incorporates a set of variables in a beaver intrinsic potential (BIP) model to predict where beavers are likely to be present, the important habitat needs of vegetation for food/shelter and human interference were not included in their model. Our model, however, incorporated those variables, which are essential for the life history of beavers, thereby improving the accuracy of our wetland habitat mapping and, ultimately, better informing wetland habitat conservation and management decisions. Furthermore, the consideration of wildlife history needs in the derivation of intermediate functional layers not only improved the classification of the primary features of interest in our study, but also potentially, has management and conservation implications beyond beavers and wetlands. For example, our results can be used to generate standardized procedures and indices for a myriad of species where remote sensing imagery can be used to delineate important habitat features for those species (e.g., meadow marsh or deciduous forest species). Intermediate remote sensing products are not only beneficial for wildlife habitat mapping but can also have great potential for broader usage for other habitat management activities, such as forest management plans or controlling lake/river water levels.

Geo-referenced data on current and historical wildlife abundance is fundamental in modeling species habitat relationships especially when linking remote sensing data to species presence. As shown in our study, when fine scale wildlife data are available, the accuracy of the predictive habitat model is greatly improved. This can be further improved with the widely used Maxent model (Phillips, Anderson, Dudík, Schapire, & Blair, 2017; Phillips, Dudík, & Schapire, 2004), which systematically maps the wildlife habitat with adaptive learning based on more and improved precision of wildlife species presence and distribution. However, in the case of insufficient information (i.e., data availability or geo-referencing error) on the presence/absence of wildlife, the predictive habitat model performs poorly. Our model incorporated knowledge of the life history and behaviour of beavers to identify, derive and weigh the corresponding environmental/habitat variables to better inform our predictive habitat model. As a result, this produced an efficient tool to create an accurate beaver pond map (over 80% accuracy) to inform future habitat conservation and management actions. Notably, the environmental/habitat variables that we used in our model not only describe the life history needs of the beaver but they will also serve as part of the conditions in the process of multivariate Maxent modeling later when the species distribution information is available.

It is also noteworthy that the integrated use of multi-temporal and multi-source data can pose challenges when data acquisition times vary among sources. The DEM used in our study was generated from the stereo imagery collected between April to May 2013, the RS2 time series data were obtained in 2016, while the S1 MSI time series were taken in 2020. Among all of the environmental/habitat features, the wetland features derived from the combined RS2 and S1 MSI can be affected the most based on when the data are collected/acquired. For example, the shape, extent and size of both wetlands and open waterbodies can change based on annual snow pack and precipitation and lake ice. However, using an AHP model, this may be accounted for through the assignment of different weights for various features based on their importance to the study species; in our study, the AHP assigned a weight of 22.0% for the wetland features for beavers. Although data collection time among different data sources can be a drawback in segmenting the wetland class, the error propagating into mapping the beaver activity map in our study was still minimal. In addition, the spatial resolution of the data plays an important factor in developing the predictive habitat model. Our beaver activity map demonstrates that the density of the streams correlates closely with the number of beaver dams. It should be noted that the DEM used in our study had a high resolution of 2 meters, so the derived

stream network had seven orders. On the other hand, with a 30-meter-resolution DEM, the stream network can only be derived up to four orders. In that case, the upper streams that the beaver preferred were missed and, thus, the resulting beaver activity map was less accurate.

5.6 Summary

In this study, a framework was established for waterfowl habitat mapping with a fuzzy AHP model and the use of remote sensing products. Multi-source and multi-temporal remotely sensed data were used to derive environmental/habitat variables based on the knowledge of the behavior of beavers (food sources, shelters, etc.), and the locations of "potential" beaver ponds were identified. Specifically, DEM, seasonal S1 MSI, and RS 2 data were employed to extract a set of environmental/habitat features; AHP was used to model the features important to informing beaver activity; and beaver ponds were identified from the previously generated high-activity area. In the proposed beaver habitat model, hydrology and additional vegetation (habitat) related features were all incorporated. In addition, rather than assigning the feature weights based on an empirical estimation, AHP was used to mathematically

calculate the weights of each feature. Thereafter, a comprehensive activity map was predicted based on the features. The results of this study demonstrated that it was possible to create a wetland habitat monitoring tool to accurately map beaver activity on the landscape and then extract the location of "potential" beaver ponds. Based on validation against the known locations of beaver dams from the ground truth provincial data, the results were over 83.0% accurate in predicting the location of beaver dams located within highly active areas. Notably, over 72.5% of the beaver ponds were successfully identified compared with manually digitized ponds. Commission errors occurred due to the inaccurate mapping of deciduous forest areas, such as meadows and wetlands, which exhibited the same seasonal changes as deciduous trees. Most omission errors were due to the acquisition time difference between the dataset and the seasonal effects on the size and extent of the open water bodies.

Chapter 6
Conclusion and Future Work

To fully utilize the available remotely sensed data for wildlife habitat management, advanced methodologies were developed to derive information related to the properties of environmental features, and tools were created to improve the understanding of the role of a habitat in shaping animal distributions, behavior, and population dynamics.

The novelty and major contributions of this research can be summarized as follows.

(1) An advanced machine learning approach was developed to characterize the forest succession stages utilizing an imagery spatial pattern analysis and random forest (Chapter 2).

(2) A deep-learning and machine-learning integrated method was developed for the automatic identification and mapping of forest roads (Chapter 3).

(3) The robust stepwise automatic thresholding method was developed to accurately map the dynamics of surface waters within seconds (Chapter 4).

(4) A wetland habitat monitoring framework was established to accurately map beaver-altered wetlands in the landscape using remote sensing products derived based on the knowledge of beaver activities (Chapter 5).

(5) My overall findings contribute to the knowledge base regarding improving the value and utility of remote sensing products to support habitat monitoring initiatives, such as quantifying wetland habitat changes over time, assessing wildlife responses to habitat changes, and integrating this habitat data into existing monitoring-management frameworks.

The detailed findings for the abovementioned individual investigations are described as follows.

(1) This study provided a comprehensive investigation of variables derived from a texture analysis of GLCM, semi-variogram, and spectral variables of shadow fraction and shadow distribution. The machine learning RF classification has been utilized and the result demonstrated that the metrics derived from spatial pattern analysis can differentiate the stages of forest stand development with a classification accuracy of 89%. The new metric derive from the presence of shadow improves the forest stages classification accuracy, and rank the most important metrics. In addition, the cross-validation of the image texture

classification using LiDAR derived indices of PLH demonstrated that the multispectral imagery can be used as a cost effective alternative of LiDAR to derive forest successional stages. It worth mentioning that my study supports the findings of the research conducted by Kayitakire et al. (2006) with forest structural parameters including basal area, top height, circumference, stand density, and age were modeled using image texture features derived from1m resolution IKONOS-2 imagery. Also, important GLCM features found are similar to what has demonstrated in Ozdemir and Karnieli's study (Ozdemir & Karnieli, 2011).

(2) The study on forest road extraction focused on a novel method that utilizes road feature filtering and VGG 16 together. Multivariate Gaussian and its LoG were utilized to extract road feature candidates from the imagery, VGG 16 was then employed to provide refined results. The vegetation-covered secondary roads can be successfully identified and extraction from the proposed method, which has not been achieved in previous investigations. Based on the validation against manually digitized roads, the results showed that the proposed method was able to extract forest roads with an average of 74% of completeness. Compared with the forest road extraction results of Azizi et al. (2014), the correctness of the extracted roads was improved from 63% to 73%.

(3) An operational SAT technique has been developed to automatically generate surface water maps from C-band SAR data (Radarsat-2 and Sentinel-1). The preprocessing of SAR data was implemented under the PCI Geomatica and the SNAP toolbox, and the SAT is written in Python. The whole process has the default values encoded in the algorithm for automatic extraction. The proposed method is adaptive to all incident angle, and found to be efficient in extracting surface water bodies from different scenes, with an overall accuracy over 98%. Also, the time-series surface water extraction results revealed the seasonal dynamics of inundation and showed a correlation between the response in the surface water extent to the changes in precipitation. This implied that the usage of SAR data might allow for detailed and timely surface water mapping for wetland habitat monitoring, which has previously been missing from inventory data and land classification maps. The algorithm developed during this study can be implemented in an operational system to generate a provincial or a national scale and can benefit long-term water monitoring frameworks for wetlands and their management. Its ability to track the changes in the surface water will facilitate habitat assessments for biodiversity dependent on wetlands, such as the effect of temporal variations in wetland habitat availability on waterfowl and the standardized monitoring of changes in a wetland habitat.

(4) A framework has been established for beaver habitat mapping that utilized a fuzzy AHP model and the use of remote sensing products derived from prior knowledge of life history of beavers. The developed beaver habitat prediction model incorporated hydrology features, and vegetation (habitat) related features. Moreover, AHP was used to mathematically calculate the weights of each feature. Based on validation against the known locations of beaver dams from ground truth provincial data, the results were over 83.0% accurate in predicting the location of beaver dams located within highly active areas. Notably, over 72.5% of the beaver ponds were successfully identified compared with manually digitized ponds. This study demonstrates that remote sensing is an effective approach for identifying beaver-modified wetland features and can be applied to map these and other wetland habitat features of interest across large spatial extents. Furthermore, the systematic acquisition strategy of the remote sensors employed is well suited for monitoring changes in wetland conditions that affect the availability of habitats important to waterfowl and other wildlife.

Although the proposed methods were demonstrated to have promising accuracy in characterizing different environmental features from multi-temporal and multi-sourcing remote sensing data, they can be further developed based on the following future considerations.

(1) An index for characterizing dynamic forest development will be investigated. The proposed method used discrete stages to characterize forest development, where the continuous descriptor was more favourable. In addition, within-stand variability that may exist within a stand development class will have individual stands that deviate from the identified stages.

(2) The inclusion of an adaptive filter will be tested to progressively extract roads with more complex conditions. Fine-tuning of the CNN network, such as changing the learning rate and weights of the layers, will also be performed. Moreover, U-net classification could be investigated if a number of masked samples of forest roads becomes available.

(3) Future studies on surface water mapping will explore non-local speckle filters to minimize the influence of the roughening of the water due to wind. More tests will also be conducted for rough terrain, as the proposed method has been applied to flat terrain.

(4) Future research on wildlife habitat modeling will further validate habitat models with ground-truth, specific wildlife activity (the presence of beaver lodges/shelters, beaver dams, waterfowl nests, etc.). Additional tests will be

performed for waterfowl habitat modeling.

(5) Additional remote sensing tools/products will be utilized to describe vegetation health, measures of habitat fragmentation, and net primary productivity. The proposed tools will also be tested to determine their ability to be scaled up to produce global maps.

(6) Due to continuously developing technology and the increasing accessibility of hyperspectral, hyper-spatial, and hyper-temporal data, the possibilities for wildlife habitat management will be enhanced. Future studies can be conducted using the open access data from newly released data from commercial satellites, airborne hyperspectral data, airborne LiDAR data, and unmanned aerial vehicles for a precise assessment of wildlife habitats. The framework for wildlife habitat management can also be further improved with machine learning and deep-learning concepts of wildlife ecology to build habitat models at different scales.

References

Allen, A. W. (1982). *Habitat suitability index models: beaver.* Western Energy and Land Use Team, Office of Biological Services, Fish and Wildlife Service, US Department of the Interior.

Amani, M., Salehi, B., Mahdavi, S., Granger, J. E., Brisco, B., & Hanson, A. (2017). Wetland classification using multi-source and multi-temporal optical remote sensing data in Newfoundland and Labrador, Canada. *Canadian Journal of Remote Sensing*, *43*, 360–373.

Anderson, J., & Bonner, J. (2014). Modeling habitat suitability for beaver (Castor canadensis) using geographic information systems. *International Conference on Energy and Environmental Science*, *61*, 12–23.

Azizi, Z., Najafi, A., & Sadeghian, S. (2014). Forest Road Detection Using LiDAR Data. *Journal of Forestry Research*, *25*(4), 975–980. https://doi.org/10.1007/s11676-014-0544-0

Banks, S., Millard, K., Pasher, J., Richardson, M., Wang, H., & Duffe, J. (2015). Assessing the potential to operationalize shoreline sensitivity mapping: Classifying multiple Wide Fine Quadrature Polarized RADARSAT-2 and Landsat 5 scenes with a single Random Forest model. *Remote Sensing*, *7*(10), 13528–13563.

Beedle, D. L. (1991). *Physical dimensions and hydrologic effects of beaver ponds on Kuiu Island in southeast Alaska*. Physical dimensions and hydrologic effects of beaver ponds on Kuiu Island in southeast Alaska.

Bergen, K. M., Goetz, S. J., Dubayah, R. O., Henebry, G. M., Hunsaker, C. T., Mhoff, M. L., … Radeloff, V. C. (2009). Remote sensing of vegetation 3D structure for biodiversity and habitat: Review and implications for lidar and radar spaceborne missions. *Journal of Geophysical Research: Biogeosciences*, *114*(G2).

Bolanos, S, Stiff, D., Brisco, B., & Pietroniro, A. (2016). Operational surface water detection and monitoring using Radarsat 2. *Remote Sensing 285*, *8*(4).

Bolanos, Sandra, Stiff, D., Brisco, B., & Pietroniro, A. (2016). Operational surface water detection and monitoring using Radarsat 2. *Remote Sensing*, *8*(4). https://doi.org/10.3390/rs8040285

Bourgeau-Chavez, L., Endres, S., Battaglia, M., Miller, M. E., Banda, E., Laubach, Z., … Marcaccio, J. (2015). Development of a bi-national Great Lakes coastal wetland and land use map using three-season PALSAR and Landsat imagery. *Remote Sensing*, *7*, 8655–8682.

Bouziani, M., Goita, K., & He, D. C. (2010). Rule-based classification of a very

high resolution image in an urban environment using multispectral segmentation guided by cartographic data. *IEEE Transactions on Geoscience and Remote Sensing*, *48*(8), 3198–3211. https://doi.org/10.1109/TGRS.2010.2044508

Breiman, L. (2001). Random forests. *Machine Learning*, *45*, 5–32.

Brisco, B., Schmitt, A., Murnaghan, K., Kaya, S., & Roth, A. (2013). SAR polarimetric change detection for flooded vegetation. *International Journal of Digital Earth*. https://doi.org/10.1080/17538947.2011.608813

Brisco, Brian. (2015). Mapping and monitoring surface water and wetlands with synthetic aperture radar. In *Remote Sensing of Wetlands: Applications and Advances*. https://doi.org/10.1201/b18210

Butenuth, M., & Heipke, C. (2012). Network snakes: Graph-based object delineation with active contour models. *Machine Vision and Applications*, *23*(1), 91–109. https://doi.org/10.1007/s00138-010-0294-8

Cain, A. T., Tuovila, V. R., Hewitt, D. G., & Tewes, M. E. (2003). Effects of a highway and mitigation projects on bobcats in Southern Texas. *Biological Conservation*, *114*(2), 189–197.

Cohen, W. B., Spies, T. A., & Bradshaw, G. A. (1990). Semivariograms of digital imagery for analysis of conifer canopy structure. *Remote Sensing of*

Environment, *34*, 167–178.

Corcoran, J. M., Knight, J. F., & Gallant, A. L. (2013). Influence of multi-source and multi-temporal remotely sensed and ancillary data on the accuracy of random forest classification of wetlands in northern Minnesota. *Remote Sensing*, *5*(7), 3212–3238. https://doi.org/10.3390/rs5073212

Cosmopoulos, P., & King, D. J. (2004). Temporal analysis of forest structural condition at an acid mine site using multispectral digital camera imagery. *International Journal of Remote Sensing*, *25*, 2259–2275.

Cunningham, J. M., Calhoun, A. J., & Glanz, W. E. (2007). Pond-breeding amphibian species richness and habitat selection in a beaver-modified landscape. *The Journal of Wildlife Management*, *71*(8), 2517–2526.

Curran, P. J. (1988). The semivariogram in remote sensing: an introduction. *Remote Sensing of Environment*, *24*(3), 493–507.

Cutler, D. R., Edwards Jr., T. C., Beard, K. H., Cutler, A., Hess, K. T., Gibson, J., & Lawler, J. J. (2007). Random Forests for classification in ecology. *Ecology*, *88*, 2783–2792.

Dale, M. R., Dixon, P., Fortin, M. J., Legendre, P., Myers, D. E., & Rosenberg, M. S. (2002). Conceptual mathematical relationships among methods for

spatial analysis. *Ecography*, *25*, 558–577.

DeGraaf, R. M., Yamasaki, M., Leak, W. B., & Lester, A. M. (2006). Technical guide to forest wildlife habitat management in New England. In *UPNE*.

Deledalle, C. A., Denis, L., Tupin, F., Reigber, A., & Jager, M. (2015). NL-SAR: A unified nonlocal framework for resolution-preserving (Pol)(In)SAR denoising. *IEEE Transactions on Geoscience and Remote Sensing*. https://doi.org/10.1109/TGRS.2014.2352555

Diefenbach, D. R., & Owen Jr, R. B. (1989). A Model of Habitat Use by Breeding American Black Ducks. *The Journal of Wildlife Management*, *53*(2), 383–389. Retrieved from https://www.jstor.org/stable/3801141

Dittbrenner, B. J., Pollock, M. M., Schilling, J. W., Olden, J. D., Lawler, J. J., & Torgersen, C. E. (2018). Modeling intrinsic potential for beaver (Castor canadensis) habitat to inform restoration and climate change adaptation. *PloS One*, *13*(2), e0192538.

Du, Z., Li, W., Zhou, D., Tian, L., Ling, F., Wang, H., … Sun, B. (2014). Analysis of Landsat-8 OLI imagery for land surface water mapping. *Remote Sensing Letters*, *5*(7), 672–681.

Dyer, S. J., O'Neill, J. P., Wasel, S. M., & Boutin. S. (2001). Avoidance of industrial development by woodland caribou. *Journal of Wildlife*

Management. 65, 531–542.

Falkowski, M. J., Evans, J. S., Martinuzzi, S., Gessler, P. E., & Hudak, A. T. (2009). Characterizing forest succession with lidar data: An evaluation for the Inland Northwest, USA. *Remote Sensing of Environment*, *113*, 946–956.

Freeman, A., & Durden, S. L. (1998). A three-component scattering model for polarimetric SAR data. *IEEE Transactions on Geoscience and Remote Sensing*, *36*(3), 963–973. https://doi.org/10.1109/36.673687

Fuller, T. K. (1989). Population dynamics of wolves in north-central Minnesota. *Wildlife Monographs*, 3–41.

Gao, L., Song, W., Dai, J., & Chen, Y. (2019). Road extraction from high-resolution remote sensing imagery using refined deep residual convolutional neural network. *Remote Sensing*, *11*(5), 1–16. https://doi.org/10.3390/rs11050552

Geldsetzer, T., & Yackel, J. J. (2009). Sea ice type and open water discrimination using dual co-polarized C-band SAR. *Canadian Journal of Remote Sensing Jan 1*, *35*(1), 73–84.

Gill, J. A., Norris, K., & Sutherland, W. J. (2001). Why behavioural responses may not reflect the population consequences of human disturbance.

Biological Conservation, *97*(2), 265–268. https://doi.org/10.1016/S0006-3207(00)00002-1

Gislason, P. O., Benediktsson, J. A., & Sveinsson, J. R. (2006). Random forests for land cover classification. *Pattern Recognition Letters*, *27*, 294–300.

Glenn, E. M., & Ripple, W. J. (2004). On using digital maps to assess wildlife habitat. *Wildlife Society Bulletin*, *32*(3), 852–860. https://doi.org/10.2193/0091-7648(2004)032[0852:oudmta]2.0.co;2

Grebner, D. L., Bettinger, P., Siry, J., & Boston, K. (2021). *Introduction to Forestry and Natural Resources.* Academic press.

Greenberg, J. A., Dobrowski, S. Z., & Ustin, S. L. (2005). Shadow allometry: Estimating tree structural parameters using hyperspatial image analysis. *Remote Sensing of Environment*, *97*, 15–25.

Guillemain, M., Pöysä, H., Fox, A.D., Arzel, C., Dessborn, L., Ekroos, J., Gunnarsson. G., Holm, T.E., Christensen, T.K., Lehikoinen, A., Mitchell, C., Rintala, J., & Moller, A.P. (2013). Effects of climate change on European ducks: what do we know and what do we need to know? *Wildl Biol*. 19, 404–419. doi:10.2981/12-11

Ham, J., Chen, Y., Crawford, M. M., & Ghosh, J. (2005). Investigation of the random forest framework for classification of hyperspectral data. *IEEE*

Transactions on Geoscience and Remote Sensing, *43*, 492–501.

Hanqiu Xu. (2006). Modification of normalised difference water index NDWI to enhance open water features in remotely sensed imagery. *International Journal of Remote Sensing*, *27*(14), 9.

Haralick, R. M., Shanmugam, K., & Dinstein, I. H. (1973). Textural features for image classification. *IEEE Transactions on Systems, Man, and Cybernetics*, 610–621.

Helle, P., & Monkkonen, M. (1990). *Forest Successions and Bird Communities: Theoretical Aspects and Practical Implications*. Amsterdam, The Netherlands: SPB Academic Publishing.

Herrera Huertas, A., Lencinas, M. V., Toro Manríquez, M., Miller, J. A., & Martínez Pastur, G. (2020). Mapping the status of the North American beaver invasion in the Tierra del Fuego archipelago. *PloS One*, *15*(4), e0232057.

Hess, L. L., Melack, J. M., Novo, E. M., Barbosa, C. C., & Gastil, M. (2003). Dual-season mapping of wetland inundation and vegetation for the central Amazon basin. *Remote Sensing of Environment*, *87*(4), 404–428.

Hill, G. J. E. (1987). Habitat mapping by Landsat for aerial census of kangaroos. *Remote Sensing of Environment*, *21*, 53–60.

Hong, S., Jang, H., Kim, N., & Sohn, H. G. (2015). Water area extraction using RADARSAT SAR imagery combined with landsat imagery and terrain information. *Sensors*, *15*(3), 6652–6667.

Hong, S., Jang, H., Kim, N., & Sohn, H.-G. (2015). Water area extraction using RADARSAT SAR imagery combined with Landsat imagery and terrain information. *Sensors (Basel, Switzerland)*, *15*(3), 6652–6667. https://doi.org/10.3390/s150306652

Hong, Z., Ming, D., Zhou, K., Guo, Y., & Lu, T. (2018). Road extraction from a high spatial resolution remote sensing image based on richer convolutional features. *IEEE Access*, *6*, 46988–47000. https://doi.org/10.1109/ACCESS.2018.2867210

Hrůza, P., Mikita, T., Tyagur, N., Krejza, Z., Cibulka, M., Procházková, A., & Patočka, Z. (2018). Detecting forest road wearing course damage using different methods of remote sensing. *Remote Sensing*, *10*(4), 1–17. https://doi.org/10.3390/rs10040492

Hu, B., Li, J., Jing, L., & Judah, A. (2014). Improving the efficiency and accuracy of individual tree crown delineation from high-density LiDAR data. *International Journal of Applied Earth Observation and Geoinformation*, *26*, 145–155.

Hu, J., Razdan, A., Femiani, J. C., Cui, M., & Wonka, P. (2007). Road network extraction and intersection detection from aerial images by tracking road footprints. *IEEE Transactions on Geoscience and Remote Sensing*, *45*(12), 4144–4157. https://doi.org/10.1109/TGRS.2007.906107

Huang, W., DeVries, B., Huang, C., Lang, M., Jones, J., Creed, I., & Carroll, M. (2018). Automated extraction of surface water extent from Sentinel-1 data. *Remote Sensing May797*, *10*(5).

Imam, E., & Tesfamichael, G. Y. (2013). Use of remote sensing, GIS and analytical hierarchy process (AHP) in wildlife habitat suitability analysis. *Journal of Materials and Environmental Science*, *4*(3), 460–467.

Inkley, D. B., Anderson, M. G., Blaustein, A. R., Burkett, V., Felzer, B., Griffith, B., … Root, T. L. (2004). Global climate change and wildlife in North America. *Technical Review*, *04*(2), 1–26.

Isnaini, N., Marhaento, H., & Subrata, S. A. (2021). Combining Analytical Hierarchy Process (AHP) and Geographical Information System (GIS) for mapping habitat threat of mentilin (Cephalopachus bancanus). *IOP Conference Series: Earth and Environmental Science.*, *623*(1), 012044.

James, A. R., & Stuart-Smith, A. K. (2000). Distribution of caribou andwolves in relation to linear corridors. *Journal of Wildlife Management*.

64, 154–159.

Jenkins, S. H. (1980). A size-distance relation in food selection by beavers. *Ecology*, *61*(4), 740–746.

Jing, L., Hu, B., Noland, T., & Li, J. (n.d.). An individual tree crown delineation method based on multi-scale segmentation of imagery. *ISPRS Journal of Photogrammetry and Remote Sensing*, *70*, 88–98.

Johansen, K., Coops, N. C., Gergel, S. E., & Stange, Y. (2007). Application of high spatial resolution satellite imagery for riparian and forest ecosystem classification. *Remote Sensing of Environment*, *110*, 29–44.

Johnson, C. J., Alexander, N. D., Wheate, R. D., & Parker, K. L. (2003). Characterizing woodland caribou habitat in sub-boreal and boreal forests. *Forest Ecology and Management*, *180*, 241–248.

Karran, D. J., Westbrook, C. J., Wheaton, J. M., Johnston, C. A., & Bedard-Haughn, A. (2017). Rapid surface-water volume estimations in beaver ponds, Hydrol. *Earth Syst. Sci*, *21*, 1039–1050. Retrieved from https://doi.org/10.5194/hess-21-1039-2017

Kayitakire, F., Hamel, C., & Defourny, P. (2006). Retrieving forest structure variables based on image texture analysis and IKONOS-2 imagery. *Remote Sensing of Environment*, *102*, 390–401.

Klein, I., Dietz, A. J., Gessner, U., Galayeva, A., Myrzakhmetov, A., & Kuenzer, C. (2014). Evaluation of seasonal water body extents in Central Asia over thepast 27 years derived from medium-resolution remote sensing data. *International Journal of Applied Earth Observation and Geoinformation*. https://doi.org/10.1016/j.jag.2013.08.004

Lane, C. R., & D'Amico, E. (2010). Calculating the ecosystem service of water storage in isolated wetlands using LiDAR in north central Florida, USA. *Wetlands*. https://doi.org/10.1007/s13157-010-0085-z

Lawrence, R. L., Wood, S. D., & Sheley, R. L. (2006). Mapping invasive plants using hyperspectral imagery and Breiman Cutler classifications (Random Forest). *Remote Sensing of Environment*, *100*, 356–362.

Lebbin, D., Parr, M., Fenwick, G. (2010). The American bird conservancy guide to bird conservation. The University of Chicago Press, Chicago

Levesque, J., & King, D. J. (1999). Airborne digital camera semivariance for evaluation of forest structural damage at an acid mine. *Remote Sensing of the Environment*, *68*(December 1997), 112–124.

Li, J., & Wang, S. (2015). An automatic method for mapping inland surface waterbodies with Radarsat-2 imagery. *International Journal of Remote Sensing*, *36*(5), 1367–1384.

https://doi.org/10.1080/01431161.2015.1009653

Liang, J., & Liu, D. (2020). A local thresholding approach to flood water delineation using Sentinel-1 SAR imagery. *ISPRS Journal of Photogrammetry and Remote Sensing*, *159*(October 2019), 53–62. https://doi.org/10.1016/j.isprsjprs.2019.10.017

Lim, K., Treitz, P., Wulder, M., St-Onge, B., & Flood, M. (2003). LiDAR remote sensing of forest structure. *Progress in Physical Geography*, *27*(1), 88–106.

Lin, S. C. (2016). Landscape and traffic factors affecting animal road mortality. *Journal of Environmental Engineering and Landscape Management*, *24*(1), 10–20.

Lindenmayer, D. B. (2009). Forest wildlife management and conservation. *Annals of the New York Academy of Sciences*, *1162*(1), 284–310.

Lu, X., Zhong, Y., Zheng, Z., Liu, Y., Zhao, J., Ma, A., & Yang, J. (2019). Multi-Scale and Multi-Task Deep Learning Framework for Automatic Road Extraction. *IEEE Transactions on Geoscience and Remote Sensing*, *57*(11), 9362–9377. https://doi.org/10.1109/TGRS.2019.2926397

Manjusree, P., Prasanna Kumar, L., Bhatt, C. M., Rao, G. S., & Bhanumurthy, V. (2012a). Optimization of threshold ranges for rapid flood inundation

mapping by evaluating backscatter profiles of high incidence angle SAR images. *International Journal of Disaster Risk Science*. https://doi.org/10.1007/s13753-012-0011-5

Manjusree, P., Prasanna Kumar, L., Bhatt, C. M., Rao, G. S., & Bhanumurthy, V. (2012b). Optimization of threshold ranges for rapid flood inundation mapping by evaluating backscatter profiles of high incidence angle SAR images. *International Journal of Disaster Risk Science*, *3*(2), 113–122. https://doi.org/10.1007/s13753-012-0011-5

Marshall, I. B., Smith, C. A. S., & Selby, C. J. (1996). A National Framework for Monitoring and Reporting on Environmental Sustainability in Canada. In *Global to Local: Ecological Land Classification* (pp. 25–38). https://doi.org/10.1007/978-94-009-1653-1_4

Martinis, S., Twele, A., & Voigt, S. (2009). Towards operational near real-time flood detection using a split-based automatic thresholding procedure on high resolution TerraSAR-X data. *Natural Hazards and Earth System Science*. https://doi.org/10.5194/nhess-9-303-2009

Matgen, P., Hostache, R., Schumann, G., Pfister, L., Hoffmann, L., & Savenije, H. H. G. (2011). Towards an automated SAR-based flood monitoring system: Lessons learned from two case studies. *Physics and Chemistry of*

the Earth. https://doi.org/10.1016/j.pce.2010.12.009

Máttyus, G., Wang, S., Fidler, S., & Urtasun, R. (2015). Enhancing road maps by parsing aerial images around the world. *Proceedings of the IEEE International Conference on Computer Vision*, 1689–1697. Vis.

Maxie, A. J., Hussey, K. F., Lowe, S. J., Middel, K. R., Pond, B. A., Obbard, M. E., & Patterson., B. R. (2010). A comparison of forest resource inventory, provincial land cover maps and field surveys for wildlife habitat analysis in the Great Lakes–St. Lawrence forest. *The Forestry Chronicle*, *86*(1), 77–86.

McDermid, G. J., Hall, R. J., Sanchez-Azofeifa, G. A., Franklin, S. E., Stenhouse, G. B., Kobliuk, T., & LeDrew, E. F. (2009). Remote sensing and forest inventory for wildlife habitat assessment. *Forest Ecology and Management*, *257*(11), 2262–2269. https://doi.org/10.1016/j.foreco.2009.03.005

McFeeters, S. K. (1996). The use of the Normalized Difference Water Index (NDWI) in the delineation of open water features. *International Journal of Remote Sensing*, *17*(7), 1425–1432.

Medhi, A., & Saha, A. K. (2014). Land cover change and rhino habitat mapping of Kaziranga National Park, Assam. In *Climate change and biodiversity*.

Springer, Tokyo.

Medioni, G., Tang, C.-K., & Lee, M.-S. (2000). Tensor Voting : Theory and Applications. *Congrès Francophone Sur La Reconnaissance Des Formes et l'Intelligence Artificielle (RFIA)*, *2000*.

Meentemeyer, R. K. and, & Butler, D. R. (1995). Temporal and spatial changes in beaver pond locations, eastern Glacier National Park, Montana, USA. *The Geographical Bulletin*, *37*(2), 97.

Mena, J. B., & Malpica, J. A. (2005). An automatic method for road extraction in rural and semi-urban areas starting from high resolution satellite imagery. *Pattern Recognition Letters*, *26*(9), 1201–1220,.

Merendino, M. T., & Ankney, C. D. (1994). Habitat use by mallards and American black ducks breeding in central Ontario. *The Condor*, *96*(2), 411–421.

Morandeira, N. S., Grings, F., Facchinetti, C., & Kandus, P. (2016). Mapping plant functional types in floodplain wetlands: An analysis of C-band polarimetric SAR data from RADARSAT-2. *Remote Sensing*. https://doi.org/10.3390/rs8030174

Movaghati, S., Moghaddamjoo, A., & Tavakoli, A. (2010). Filtering and Extended Kalman Filtering. *IEEE Transactions on Geoscience and*

Remote Sensing, *48*(7), 2807–2817.

Murfitt, J., Brown, L. C., & Howell, S. E. L. (2018). Evaluating RADARSAT-2 for the monitoring of lake ice phenology events in mid-latitudes. *Remote Sensing*. https://doi.org/10.3390/rs10101641

Osborne, P. E., Alonso, J. C., & Bryant, R. G. (2001). Modelling landscape-scale habitat use using GIS and remote sensing: a case study with great bustards. *Journal of Applied Ecology*, *38*(2), 458–471.

Otsu, N. (1979). THRESHOLD SELECTION METHOD FROM GRAY-LEVEL HISTOGRAMS. *IEEE Trans Syst Man Cybern*, *SMC-9*(1), 62–66. https://doi.org/10.1109/TSMC.1979.4310076

Ozdemir, I. (2008). Estimating stem volume by tree crown area and tree shadow area extracted from pan-sharpened Quickbird imagery in open Crimean juniper forests. *International Journal of Remote Sensing*, *29*, 5643–5655.

Ozdemir, I., & Donoghue, D. N. (2013). Modelling tree size diversity from airborne laser scanning using canopy height models with image texture measures. *Forest Ecology and Management*, *295*, 28–37.

Ozdemir, I., & Karnieli, A. (2011). Predicting forest structural parameters using the image texture derived from WorldView-2 multispectral imagery in a

dryland forest, Israel. *International Journal of Applied Earth Observation and Geoinformation*, *13*, 701–710.

Pesaresi, M. (2000). Texture analysis for urban pattern recognition using fine-resolution panchromatic satellite imagery. *Geographical and Environmental Modelling*, *4*(1), 43–63.

Phillips, S. J., Anderson, R. P., Dudík, M., Schapire, R. E., & Blair, M. E. (2017). Opening the black box : an open-source release of Maxent. *Ecography*, *40*(March), 887–893. https://doi.org/10.1111/ecog.03049

Phillips, S. J., Dudík, M., & Schapire, R. E. (2004). A maximum entropy approach to species distribution modeling. *Proceedings of the Twenty-First International Conference on Machine Learning*, 83.

Pollock, M. M., Pess, G. R., Beechie, T. J., & Montgomery., D. R. (2004). The importance of beaver ponds to coho salmon production in the Stillaguamish River basin, Washington, USA. *North American Journal of Fisheries Management*, *24*(3), 749–760.

Qin, X., Yang, J., Li, P., & Sun, W. (2019). Research on Water Body Extraction from Gaofen-3 Imagery Based on Polarimetric Decomposition and Machine Learning. *International Geoscience and Remote Sensing Symposium (IGARSS)*, 6903–6906.

https://doi.org/10.1109/IGARSS.2019.8898204

Quegan, S., Toan, T. Le, Yu, J. J., Ribbes, F., & Floury, N. (2000). Multitemporal ERS SAR analysis applied to forest mapping. *IEEE Transactions on Geoscience and Remote Sensing*. https://doi.org/10.1109/36.842003

Ravanbakhsh, M., Heipke, C., & Pakzad, K. (2008). Road Junction Extraction From High-Resolution Aerial Imagery. *The Photogrammetric Record*, *23*(124), 405–423.

Rawat, J. S., & Kumar, M. (2015). Monitoring land use/cover change using remote sensing and GIS techniques: A case study of Hawalbagh block, district Almora, Uttarakhand, India. *The Egyptian Journal of Remote Sensing and Space Science*, *18*(1), 77–84.

Reed, R. A., Johnson-Barnard, J., & Baker, W. L. (1996). Contribution of roads to forest fragmentation in the Rocky Mountains. *Conservation Biology*, *10*(4), 1098–1106.

Rempel, R. S., Abraham, K. F., Gadawski, T. R., & Gabor, S. (1997). A Simple Wetland Habitat Classification for Boreal Forest Waterfowl Published by : Wiley on behalf of the Wildlife Society Stable URL : http://www.jstor.org/stable/3802181 Accessed : 27-06-2016 05 : 14 UTC

Your use of the JSTOR archive indicates your acce. *The Journal of Wildlife Management*, *61*(3), 746–757. Retrieved from http://www.jstor.org/stable/3802181

Rettie, J.W., & Messier, F.(2000) Hierarchical habitat selection by woodland caribou: Its relationship to limiting factors. *Ecography*, 23, 466–478.

Robertson, A., McDonald, R. A., Delahay, R. J., Kelly, S. D., & Bearhop, S. (2015). Resource availability affects individual niche variation and its consequences in group-living European badgers Meles meles. *Oecologia*, *178*(1), 31–43.

Rosenfeld, J. S., & Hatfield, T. (2006). Information needs for assessing critical habitat of freshwater fish. *Canadian Journal of Fisheries and Aquatic Sciences*, *63*(3), 683–698.

Saaty, T. L. (2004). Decision making—the analytic hierarchy and network processes (AHP/ANP). *Journal of Systems Science and Systems Engineering*, *13*(1), 1–35.

Saito, S., Yamashita, T., & Aoki, Y. (2016). Multiple object extraction from aerial imagery with convolutional neural networks. *IS and T International Symposium on Electronic Imaging Science and Technology*, *60*(1), 1–9. https://doi.org/10.2352/ISSN.2470-1173.2016.10.ROBVIS-392

Santoro, M., Wegmüller, U., Lamarche, C., Bontemps, S., Defourny, P., & Arino, O. (2015). Strengths and weaknesses of multi-year Envisat ASAR backscatter measurements to map permanent open water bodies at global scale. *Remote Sensing of Environment*, *171*, 185–201. https://doi.org/10.1016/j.rse.2015.10.031

Schaefer, J. A., & Mahoney, S. P. (2007). Effects of progressive clearcut logging on Newfoundland caribou. The Journal of Wildlife Management, 71(6), 1753-1757.

Storeheier, P.V., Mathiesen, S.D., Tyler, N.J.C., & Olsen, M.A. (2002). Nutritive value of terricolous lichens for reindeer in winter. *Lichenologist*, 34, 247–257.

Saunders, R., Bozek, M. A., Edwards, C. J., Jennings, M. J., & Newman, S. P. (2002). Habitat features affecting smallmouth bass Micropterus dolomieu nesting success in four northern Wisconsin lakes. *American Fisheries Society Symposium 31*, 123–134.

Sawaya, K. E., Olmanson, L. G., Heinert, N. J., Brezonik, P. L., & Bauer, M. E. (2003). Extending satellite remote sensing to local scales: land and water resource monitoring using high-resolution imagery. *Remote Sensing of Environment 88 144156*, 1–2.

Sherba, J., Blesius, L., & Davis, J. (2014). Object-based classification of abandoned logging roads under heavy canopy using LiDAR. *Remote Sensing*, *6*(5), 4043–4060. https://doi.org/10.3390/rs6054043

Shi, W., Miao, Z., & Debayle, J. (2013). An integrated method for urban main-road centerline extraction from optical remotely sensed imagery. *Geoscience and Remote Sensing, IEEE Transactions On*, *52*(6), 3359–3372.

Silveira, M., Heleno, S., & IEEE, ,. (2009). Separation between water and land in SAR images using region-based level sets. *And Remote Sensing Letters Pp*, *6*(3), 471–475.

Simonyan, K., & Zisserman, A. (2014). Very deep convolutional networks for large-scale image recognition. *ArXiv Preprint ArXiv:1409.1556*. Retrieved from https://arxiv.org/abs/1409.1556

Smith, L. C., Sheng, Y., MacDonald, G. M., & Hinzman, L. D. (2005). Atmospheric Science: Disappearing Arctic lakes. *Science*. https://doi.org/10.1126/science.1108142

Soille, P. (2013). Morphological image analysis: principles and applications. *Springer Science Business Media Mar 14*.

Soille, Pierre, & Pesaresi, M. (2002). Advances in mathematical morphology

applied to geoscience and remote sensing. *IEEE Transactions on Geoscience and Remote Sensing*, *40*(9), 2042–2055. https://doi.org/10.1109/TGRS.2002.804618

Song, C., & Woodcock, C. E. (2002). The spatial manifestation of forest succession in optical imagery: The potential of multi-resolution imagery. *Remote Sensing of Environment*, *82*, 271–284.

Song, M., & Civco, D. (2004). Road extraction using SVM and image segmentation. *Photogrammetric Engineering and Remote Sensing*, *70*(12), 1365–1371. https://doi.org/10.14358/PERS.70.12.1365

Stevens, C. E., Paszkowski, C. A., & Foote, A. L. (2007). Beaver (Castor canadensis) as a surrogate species for conserving anuran amphibians on boreal streams in Alberta, Canada. *Biological Conservation*, *134*(1), 1–13.

Suzuki, N., & McComb, W. C. (1998). *Habitat classification models for beaver (Castor canadensis) in the streams of the central Oregon Coast Range.*

Swanson, M. E., Franklin, J. F., Beschta, R. L., Crisafulli, C. M., DellaSala, D. A., Hutto, R. L., … Swanson, F. J. (2011). The forgotten stage of forest succession: early-successional ecosystems on forest sites. *Frontiers in Ecology and the Environment*, *9*(2), 117–125.

Szantoi, Z., Smith, S. E., Strona, G., Koh, L. P., & Wich, S. A. (2017).

Mapping orangutan habitat and agricultural areas using Landsat OLI imagery augmented with unmanned aircraft system aerial photography. *International Journal of Remote Sensing*, *38*(8–10), 2231–2245.

Tang, T. Q., Li, J. G., Huang, H. J., & Yang, X. B. (2014). A car-following model with real-time road conditions and numerical tests. *Measurement: Journal of the International Measurement Confederation*, *48*(1), 63–76. https://doi.org/10.1016/j.measurement.2013.10.035

Tarboton, D. G., Bras, R. L., & Rodriguez-Iturbe, I. (1991). On the extraction of channel networks from digital elevation data. *Hydrological Processes*, *5*(1), 81–100.

Touzi, R., Deschamps, A., & Rother, G. (2007). Wetland characterization using polarimetric RADARSAT-2 capability. *Canadian Journal of Remote Sensing*, *33*, S56–S67. https://doi.org/10.5589/m07-047

Trombulak, S. C., & Frissell, C. A. (2000). Review of ecological effects of roads on terrestrial and aquatic communities. *Conservation Biology, 14*(1), 18–30.

Valero, S., Chanussot, J., Benediktsson, J. A., Talbot, H., & Waske, B. (2010). Advanced directional mathematical morphology for the detection of the road network in very high resolution remote sensing images. *Pattern*

Recognition Letters. https://doi.org/10.1016/j.patrec.2009.12.018

Van Ewijk, K. Y., Tritz, P. M., & Scott, N. A. (2011). Characterizing forest succession in Central Ontario using LiDAR-derived indices. *Photogrammetric Engineering & Remote Sensing*, *77*, 261–270.

Vors, L. S., Schaefer, J. A., Pond, B. A., Rodgers, A. R., & Patterson, B. R. (2007). Woodland caribou extirpation and anthropogenic landscape disturbance in Ontario. The Journal of wildlife management, 71(4), 1249-1256.

Wei, Y., Wang, Z., & Xu, M. (2017). Road Structure Refined CNN for Road Extraction in Aerial Image. *IEEE Geoscience and Remote Sensing Letters*, *14*(5), 709–713. https://doi.org/10.1109/LGRS.2017.2672734

Westerhoff, R. S., Kleuskens, M. P. H., Winsemius, H. C., Huizinga, H. J., Brakenridge, G. R., & Bishop, C. (2013). Automated global water mapping based on wide-swath orbital synthetic-aperture radar. *Hydrology Earth System Sciences*, *17*(1).

White, L., Brisco, B., Dabboor, M., Schmitt, A., & Pratt, A. (2015). A collection of SAR methodologies for monitoring wetlands. In *Remote Sensing* (Vol. 7). https://doi.org/10.3390/rs70607615

White, R. A., Dietterick, B. C., Mastin, T., & Strohman, R. (2010). forest roads

mapped using LiDAR in steep forested terrain. *Remote Sensing*, *2*(4), 1120–1141. https://doi.org/10.3390/rs2041120

Wiedemann, C., Heipke, C., Mayer, H., & Jamet, O. (1998). Empirical Evaluation Of Automatically Extracted Road Axes. *Empirical Evaluation Techniques in Computer Vision*, *12*, 172–187. Retrieved from http://citeseerx.ist.psu.edu/viewdoc/summary?doi=10.1.1.57.5701

Witmer, G. W. (2005). Wildlife population monitoring: some practical considerations. *Wildlife Research*, *32*(3), 259–263.

Woo, M. K., & Waddington, J. M. (1990). Effects of beaver dams on subarctic wetland hydrology. *Arctic*, 223–230.

Woodcock, C. E., Strahler, A. H., & Jupp, D. L. B. (1988). The use of variograms in remote sensing: II. Real digital images. *Remote Sensing of Environment*, *25*(3), 349–379.

Wu, Z., & Xu, J. (2012). A consistency and consensus based decision support model for group decision making with multiplicative preference relations. *Decision Support Systems*, *52*(3), 757–767.

Wulder, M. A., Hall, R. J., Coops, N. C., & Franklin, S. E. (2004). High spatial resolution remotely sensed data for ecosystem characterization. *BioScience*, *54*, 511–521.

Yang, H., Yang, X., Heskel, M., Sun, S., & Tang, J. (2017). Seasonal variations of leaf and canopy properties tracked by ground-based NDVI imagery in a temperate forest. *Scientific Reports*, *7*(1), 1–10. Retrieved from https://doi.org/10.1038/s41598-017-01260-y

Yilmaz, K. K., Adler, R. F., Tian, Y., Hong, Y., & Pierce, H. F. (2010). Evaluation of a satellite-based global flood monitoring system. *International Journal of Remote Sensing*. https://doi.org/10.1080/01431161.2010.483489

Zhang, C., Murai, S., & Baltsavias, E. P. (1999). Road network detection by mathematical morphology. *ISPRS Workshop" 3D Geospatial Data Production: Meeting Application Requirements.*, 12–19. https://doi.org/10.3929/ethz-a-010782581

Zhang, H. K., & Roy, D. P. (2017). Using the 500 m MODIS land cover product to derive a consistent continental scale 30 m Landsat land cover classification. *Remote Sensing of Environment*. https://doi.org/10.1016/j.rse.2017.05.024

Zhang, P., Chen, L., Li, Z., Xing, J., Xing, X., & Yuan, Z. (2019). Automatic extraction of water and shadow from SAR images based on a multi-resolution dense encoder and decoder network. *Sensors (Switzerland)*,

19(16). https://doi.org/10.3390/s19163576

Zhang, W., Hu, B., & Brown, G. S. (2020). Automatic Surface Water Mapping Using Polarimetric SAR Data for Long-Term Change Detection. *Water*, *12*(3), 872.

Zhang, Z., Liu, Q., & Wang, Y. (2018). Road Extraction by Deep Residual U-Net. *IEEE Geoscience and Remote Sensing Letters*, *15*(5), 749–753. https://doi.org/10.1109/LGRS.2018.2802944

Zhong, Z., Li, J., Cui, W., & Jiang, H. (2016). Fully convolutional networks for building and road extraction: Preliminary results. *International Geoscience and Remote Sensing Symposium (IGARSS)*, *2016-Novem*, 1591–1594. https://doi.org/10.1109/IGARSS.2016.7729406

Zhou, C. (2000). Flood monitoring using multi-temporal AVHRR and RADARSAT imagery. *Photogrammetric Engineering and Remote Sensing 66*, *5*, 633–638.

Zhou, X., Liu, X., & Zhang, Z. (2019). Automatic extraction of lakes on the qinghai-tibet plateau from sentinel-1 SAR images. *2019 SAR in Big Data Era, BIGSARDATA 2019 - Proceedings*, 1–4. https://doi.org/10.1109/BIGSARDATA.2019.8858446

Zhu, C., Shi, W., Pesaresi, M., Liu, L., Chen**, X., & King, B. (2005). The

recognition of road network from high-resolution satellite remotely sensed data using image morphological characteristics. *International Journal of Remote Sensing*, *26*(24), 5493–5508. https://doi.org/10.1080/01431160500300354

Appendix

Table 1. Summary of Radarsat-2 data acquired over the study sites from May 2008 to August 2016.

Acquisition	Image Mode	Incident Angle(°)		Resolution (m) (range × azimut	Polarization	Direction
		Near	Far			
2008-05-	FQ4	22.1	24.1	5.2 × 7.6	Quad Pol	Descending
2008-07-	FQ18	37.4	38.9	5.2 × 7.6	Quad Pol	Ascending
2008-08-	FQ18	37.4	38.9	5.2 × 7.6	Quad Pol	Ascending
2008-08-	FQ9	28	29.8	5.2 × 7.6	Quad Pol	Descending
2009-08-	FQ9	28	29.8	5.2 × 7.6	Quad Pol	Descending
2010-07-	FQ18	37.4	38.9	5.2 × 7.6	Quad Pol	Ascending
2010-07-	FQ9	28	29.8	5.2 × 7.6	Quad Pol	Descending
2010-08-	FQ4	22.1	24.1	5.2 × 7.6	Quad Pol	Ascending
2010-08-	FQ18	37.4	38.9	5.2 × 7.6	Quad Pol	Ascending
2010-08-	FQ9	28	29.8	5.2 × 7.6	Quad Pol	Descending
2010-08-	FQ4	22.1	24.1	5.2 × 7.6	Quad Pol	Ascending
2011-07-	FQ18	37.4	38.9	5.2 × 7.6	Quad Pol	Ascending
2011-07-	FQ14	33.4	35.1	5.2 × 7.6	Quad Pol	Ascending
2011-08-	FQ18	37.4	38.9	5.2 × 7.6	Quad Pol	Ascending
2011-08-	FQ14	33.4	35.1	5.2 × 7.6	Quad Pol	Ascending
2011-08-	FQ18	37.4	38.9	5.2 × 7.6	Quad Pol	Ascending
2012-05-	FQ14	33.4	35.1	5.2 × 7.6	Quad Pol	Ascending
2012-05-	FQ18	37.4	38.9	5.2 × 7.6	Quad Pol	Ascending
2012-05-	FQ14	33.4	35.1	5.2 × 7.6	Quad Pol	Ascending
2014-05-	FQ23	41.9	43.3	5.2 × 7.6	Quad Pol	Descending
2014-05-	FQ9	28	29.8	5.2 × 7.6	Quad Pol	Descending
2014-06-	FQ18	37.4	38.9	5.2 × 7.6	Quad Pol	Ascending
2014-06-	FQ9	28	29.8	5.2 × 7.6	Quad Pol	Descending
2014-08-	FQ18	37.4	38.9	5.2 × 7.6	Quad Pol	Ascending
2014-08-	FQ9	28	29.8	5.2 × 7.6	Quad Pol	Descending
2015-05-	FQ9	28	29.8	5.2 × 7.6	Quad Pol	Descending
2015-05-	FQ14	33.4	35.1	5.2 × 7.6	Quad Pol	Ascending
2015-05-	FQ28	46	47.2	5.2 × 7.6	Quad Pol	Ascending
2015-05-	FQ9	28	29.8	5.2 × 7.6	Quad Pol	Ascending
2015-05-	FQ23	41.9	43.3	5.2 × 7.6	Quad Pol	Ascending
2015-05-	FQ4	22.1	24.1	5.2 × 7.6	Quad Pol	Ascending
2015-05-	FQ18	37.4	38.9	5.2 × 7.6	Quad Pol	Ascending
2015-06-	FQ4	22.1	24.1	5.2 × 7.6	Quad Pol	Ascending
2015-06-	FQ9	28	29.8	5.2 × 7.6	Quad Pol	Descending
2015-07-	FQ4	22.1	24.1	5.2 × 7.6	Quad Pol	Ascending
2015-07-	FQ18	37.4	38.9	5.2 × 7.6	Quad Pol	Ascending
2015-08-	FQ4	22.1	24.1	5.2 × 7.6	Quad Pol	Ascending
2015-08-	FQ18	37.4	38.9	5.2 × 7.6	Quad Pol	Ascending
2015-08-	FQ4	22.1	24.1	5.2 × 7.6	Quad Pol	Ascending
2016-05-	FQ28	46	47.2	5.2 × 7.6	Quad Pol	Descending
2016-05-	FQ28	46	47.2	5.2 × 7.6	Quad Pol	Ascending

2016-05-	FQ23	41.9	43.3	5.2 × 7.6	Quad Pol	Ascending
2016-05-	FQ4	22.1	24.1	5.2 × 7.6	Quad Pol	Descending
2016-05-	FQ9	28	29.8	5.2 × 7.6	Quad Pol	Descending
2016-06-	FQ18	37.4	38.9	5.2 × 7.6	Quad Pol	Ascending
2016-06-	FQ9	28	29.8	5.2 × 7.6	Quad Pol	Descending
2016-07-	FQ18	37.4	38.9	5.2 × 7.6	Quad Pol	Ascending
2016-07-	FQ9	28	29.8	5.2 × 7.6	Quad Pol	Descending
2016-08-	FQ9	28	29.8	5.2 × 7.6	Quad Pol	Descending
2016-08-	FQ18	37.4	38.9	5.2 × 7.6	Quad Pol	Ascending
2016-08-	FQ9	28	29.8	5.2 × 7.6	Quad Pol	Descending